UiO **: University of Oslo**

Lluís Artús Suàrez

Computational Study on the Deaminative Hydrogenation of Amides Catalyzed by Base Metal Complexes.

Thesis submitted for the degree of Philosophiae Doctor

Department of Chemistry
Faculty of Mathematics and Natural Sciences

Hylleraas Centre for Quantum Molecular Sciences

Contents

Preface

The thesis is submitted in partial fulfilment of the requirements for the degree of Philosophiae Doctor at the University of Oslo. The research here presented is the result of my studies, from August 2015 until March 2021, under the supervision of Ainara Nova, David Balcells and Mats Tilset, in the Centre for Theoretical and Computational Chemistry of the Kjemisk institutt, Universitet I Oslo.

I want to thank my supervisors for their guidance and perseverance. I am sure the education I received from them will influence my working life from now onwards, independently of the field of work. I know I have not been an easy nor regular student, and therefore, my supervision required a lot of patience. Thank you.

I also want to emphasize the importance of my friends Marius and The Pinnipeds, as well as my PhD and Master colleagues. Your moral support and scientific advice have been essential and helped me go back to the chair to keep writing.

Finally, I want to thank my family, friends from Palafrugell and Wietske, that offered unconditional sentimental support and love in the darkest times. This period of my life has been a rollercoaster, and you managed to put me back in the rails after I derailed.

<div align="center">Standing on the shoulders of giants</div>

Oslo August 2020   Lluís Artús Suàrez

II. **Abstract**

The thesis describes my investigations on the reaction mechanisms of the **Fe^H-PN^{H}P-** or **Mo^H-PN^{H}P-**catalyzed deaminative hydrogenation of amides (see Figure I). Here I propose reaction mechanisms that can explain the experimental behaviour of these reactions. The proposed reaction mechanisms have also been used for the optimization and design of more efficient systems, and the qualitative prediction of reaction-rate changes caused by several additives (proton-shuttle molecules and alkaline countercations). The reaction was studied using Density Functional Theory (DFT) calculations, and the results were later inputted in microkinetic models to be compared against experimental measures.
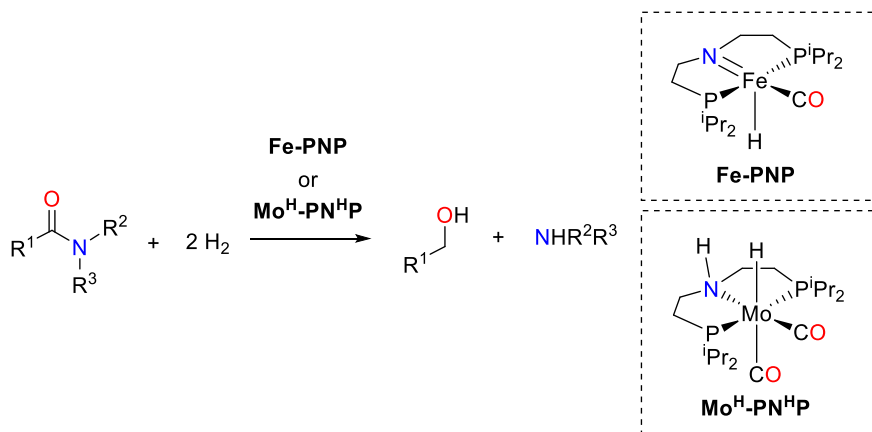
Figure I Deaminative hydrogenation of amides catalyzed by **Fe-PNP** or **Mo^H-PN^{H}P**

III. **List of Papers and Manuscripts**

The thesis is comprised of results included in the following papers.

Paper 1:   *The key role of the Hemiaminal Intermediate in the Iron-Catalyzed Deaminative Hydrogenation of Amides*

Artús Suàrez, L.; Culakova, Z.; Balcells, D.; Bernskoetter, W. H.; Eisenstein O.; Goldberg, K. I.; Hazari, N.; Tilset, M.; Nova, A.

ACS Catalysis, **2018**, *8*, 8751-8762

Paper II: *Rational Selection of co-Catalysts for the Deaminative Hydrogenation of Amides*

Artús Suàrez, L.; Jayarathne, U.; Balcells, D.; Bernskoetter, W. H.; Hazari, N.; Jaraiz M.; Nova A.

Chemical Science, **2020**, *11*, 2225-2230

Paper III: *Highly Selective Hydrogenation of Amides Catalyzed by a Molybdenum Pincer Complex: Scope and Mechanism*

Leischner, T.; **Artús Suàrez, L.**; Spannenberg, A.; Junge, K.; Nova A.; Beller M.

Chemical Science, **2019**, *10*, 10566-10576

IV. <u>**Symbols and Abbreviations**</u>

Symbols

n = number of electrons

$\vec{r}_i$ = spatial coordinates of electron i

s_i = spin of electron i

$\hat{H}$ = Hamiltonian of a system

$\hat{h}_i$ = monoelectronic Hamiltonian of electron i

Ψ = system wave function

ψ_i = monoelectronic wave function of electron i

E = Expectation value of the energy of a system

K = Expectation value of the electronic kinetic energy of a system

J = Expectation value of the Coulomb potential energy of a system

E_{ne} = Expectation value of the nuclei-electron potential energy of a system

T = Temperature

R = Ideal gas constant

h = Planck constant

k_B = Boltzmann constant

TS = Transition state

G = Free energy

v_{ne} = Nuclei-electron potential field felt by a single electron.

Abbreviations

B.O. = Born-Oppenheimer approximation

COPASI = COmplex PAthway SImulator

D = DMF = Dimethylformamide

DFT = Density Functional Theory

F = Formanilide

HF = acronym for Hartree-Fock

IEF-PCM = Integral Equation Formalism of PCM (*vide-infra*)

KS = Acronym for Kohn-Sham

LSODA = Livermore Solver for Ordinary Differential Equations "Automatic"

M = Morpholidine

MF = Methylformanilide

MA = Methylacetanilide

ODE = Ordinary Differential Equation

PCM = Polarized Continuum Model

SASA = Solvent Accessible Surface Area

SCF = Self-Consistent Field

SCRF = Self-Consistent Reaction Field

SMD = Solvent Model based on Density

TBD = Triazabicyclodecene

THF = Tetrahydrofuran

1 Introduction

1.1 Hydrogenation Reactions

The addition of hydrogen atoms to unsaturated C=X or C≡X bonds (X = C, N, O) is a widespread and routine reaction in the synthesis of both commodity and fine chemicals. The importance of hydrogenation reactions is highlighted by its broad use as an efficient method for inducing chirality: readily available prochiral olefins, ketones, imines and amides, can be transformed into high-value high-demand products, using an inexpensive reagent (hydrogen).[1,2] Furthermore, in 2001, the Royal Swedish Academy of Sciences, recognized the importance of this reaction by awarding the Nobel Prize in Chemistry to W.S. Knowles and R. Noyori for their contributions to enantioselective hydrogenation. As the thesis focusses on the hydrogenation of amides, I will introduce some general topics of hydrogenation reactions: the nature and origin of the hydrogen atoms (1), the reaction mechanisms for hydrogen activation (2) and the reaction mechanisms for hydrogen transfers (3).

1.1.1 Hydride vs molecular hydrogen

The source of hydrogen atoms will determine the reaction hazard, cost, and reaction conditions. Hydrogen sources can be classified into two main groups: hydride or molecular hydrogen sources.[3–6]

INTRODUCTION

Hydrogenation reactions with hydride sources are those that use already activated hydrogen. However, they require of an external source of protons for completing hydrogenation. Some examples of hydride sources are $LiAlH_4$, $LiBH_4$ and $NaBH_4$. Their advantage over molecular hydrogen is that they are solid and they can hydrogenate at low temperatures. However, they are less selective, and $LiAlH_4$ and $LiBH_4$ are very aggressive reducing agents that can cause severe damage if mishandled. Alternatively, some organic molecules (e.g. iPrOH)[7] can be catalytically reduced in order to use them as hydrogen sources.

Molecular hydrogen can be used directly as hydrogen source. Therefore, it is often a cheaper substrate if compared to hydride sources. Molecular hydrogen is also a greener alternative to hydride sources due to its atom efficiency. However, molecular hydrogen requires heterogeneous or homogeneous catalysts for its activation, the cost and toxicity of which may surpass those of hydride sources.

Examples of heterogeneous catalysts for hydrogenation reactions are those made of solid or supported palladium and platinum (e.g. Adam's catalyst) or nickel and aluminium (e.g. Raney nickel). These catalysts split molecular hydrogen on their surface into two hydrides via oxidative addition. They offer high catalyst reuse and easy product separation. However, their lack of selectivity and the necessary harsh reaction conditions are not suitable for many applications, including the synthesis of fine chemicals.

Homogeneous catalysts, instead, usually operate under milder conditions, are highly tunable, may be selective in respect to their reactants and/or induce chirality in their products. Their main disadvantages are their often-high production price and the need of catalyst separation from products. Some classic examples of catalyst for molecular hydrogen activation are the widely known [Rh(PPh$_3$)$_3$Cl] Wilkinson's catalyst (developed by Geoffrey Wilkinson, 1973 Nobel Prize of Chemistry) or the stereoselective [Rh(COD)(BINAP)*] and [Rh(COD)(DIPAMP)*] catalysts (developed by R. Noyori and W. S. Knowles, 2001 Nobel Prize of Chemistry). Popular newer catalysts for hydrogen activation are [Ru(Triphos)(TMM)], frustrated Lewis pairs[8–10] and the bi-functional Shvo-, Milstein- and Noyori-type catalysts (see Chapter 1.1.2).[11]

1.1.2 Homolytic vs heterolytic cleavage of H$_2$

Reaction mechanisms for catalytic molecular hydrogen activation are generally classified in two groups: those involving a homolytic cleavage of H$_2$ and those with a heterolytic cleavage.

The homolytic cleavage of H$_2$ consists of a hydrogen oxidative addition to one (e.g. Wilkinson's catalyst) or two metallic centres (e.g. Iguchi's catalyst), thus oxidizing the metal centres and producing two hydrides. (see Figure 1.1).[3,5] Both homogeneous and heterogeneous catalysts can utilize this mechanism.
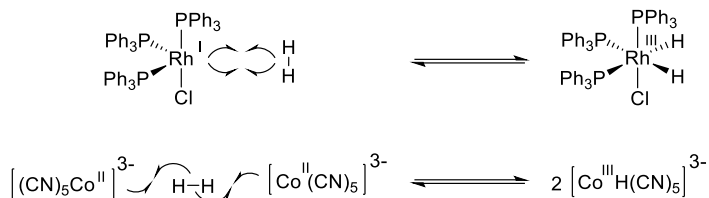
Figure 1.1 Homolytic cleavage of H_2 by Wilkinson's catalyst (above) and by Iguchi's catalyst (below).

In the heterolytic cleavage of H_2, a metal centre forms a hydride while a nucleophile generates a $H^{\delta+}$ (Figure 1.2).[3,5] Some catalysts contain nucleophilic ligands that facilitate the reaction due to their proximity to the metal centre.[12] Heterolytic cleavage of H_2 does not change the oxidation state of the metal.
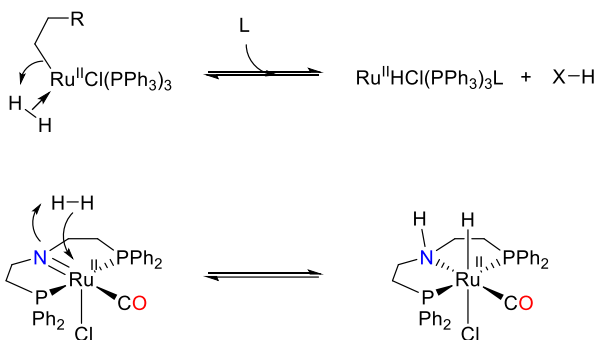
Figure 1.2 Examples of heterolytic cleavage with a [RuCl(PPh$_3$)$_3$R] catalyst (above) or a Noyori-type Ru catalyst (below).

The hydrogenations studied in the thesis utilize molecular hydrogen activated by bi-functional tridentate Noyori-type catalysts, with iron or molybdenum centres (see Figure 1.3). Bi-functional catalysts are catalysts with two active centres that can perform elementary steps of different nature, i.e. nucleophilic attacks and electrophilic additions. The active sites of bi-functional catalysts for hydrogenation reactions are

placed in a disposition favouring the reversible heterolytic cleavage of hydrogen, yielding a hydride for nucleophilic attack and a proton for electrophilic addition (see Figure 1.3). This charge separation resembles the concept of frustrated Lewis pairs.[8–10] The most popular bi-functional catalysts for multiple-bond hydrogenation can be categorized in three families that involve different nucleophilic centres: nitrogen for Noyori-type bifunctional catalysts, carbon for Milstein-type bifunctional catalysts and oxygen for Shvo-type bifunctional catalysts (see Figure 1.3). Rigid ligands are often used to set an appropriate arrangement of the catalyst active site. In the case of Noyori- and Milstein-type catalysts, these ligands are multidentate chelating ligands. The large variety of non-innocent multidentate chelating ligands gives modularity to these catalysts.[13–15]
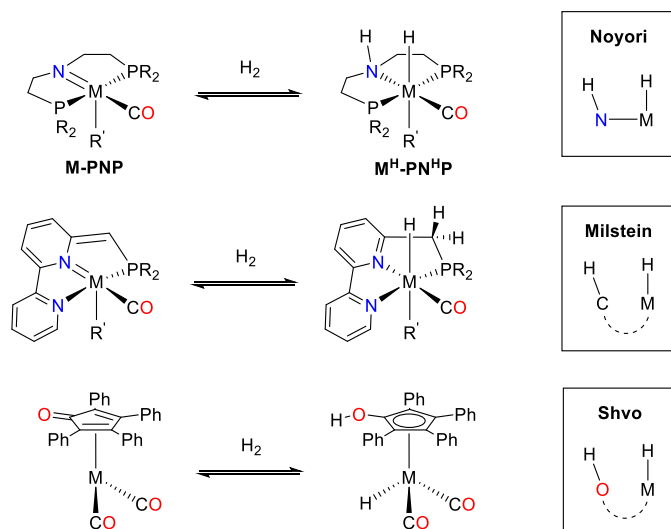
Figure 1.3 Heterolytic hydrogen cleavage assisted by Noyori-, Milstein- and Shvo-type bifunctional catalysts. Most popular metallic centres (M) are Ru, Rh or Mn. Dashed lines indicate an indirect bond between the transition metal centre and the nucleophilic centre.

1.1.3 **Hydrogen transfer mechanisms. Inner- vs outer -sphere mechanisms.**

Two main reaction mechanisms exist for homogeneous hydrogenation reactions, and they are differentiated by the presence or absence of a substrate-metal bond: inner-sphere and outer-sphere hydrogenation mechanisms, respectively (see Figure 1.4 and Figure 1.5).[3,5]

In the inner-sphere hydrogenations mechanisms, the reaction begins with a ligand decoordination to facilitate the coordination of the double-bond (see Figure 1.4). The following step is a hydride insertion to the double-bond and the formation of a substrate-metal bond. Finally, the hydrogenated molecule is eliminated either by a reductive elimination or a σ-bond metathesis (depending on the metal facility to change its oxidation state).[16] The rate of inner-sphere mechanisms strongly depends on the lability of the decoordinated ligand.
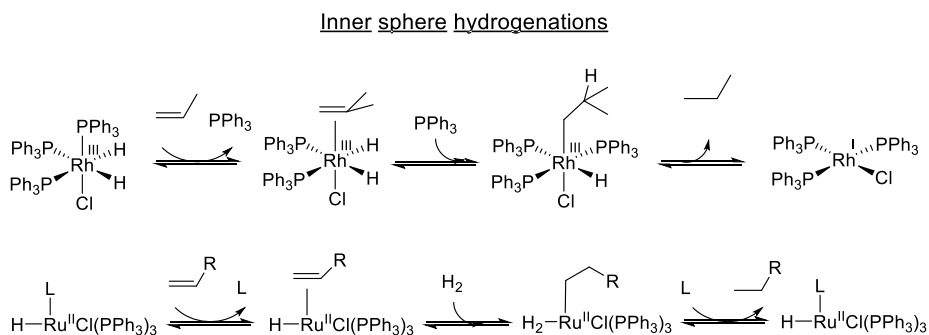
Figure 1.4 Examples of inner sphere reaction mechanisms for homogeneous catalytic double-bond hydrogenations.

In the other hand, outer-sphere hydrogenation mechanisms do not require the coordination of the substrate, neither a ligand dissociation. This mechanism consists of a hydride nucleophilic attack and a $H^{\delta+}$ electrophilic addition. There are two classes of outer-sphere mechanisms, differentiated by the order of the steps (see Figure 1.5), and none of them involve a change in the metal oxidation state. Hydrogenation of highly nucleophilic substrates (such as quinolines or acridines) will prefer outer-sphere mechanisms where there is first a $H^{\delta+}$ electrophilic addition, followed by a hydride nucleophilic attack.[3] In the other hand, Shvo-, Noyori- and Milstein-type catalysts are known to favour first a hydride nucleophilic attack, followed by a $H^{\delta+}$ electrophilic addition.[13,14]
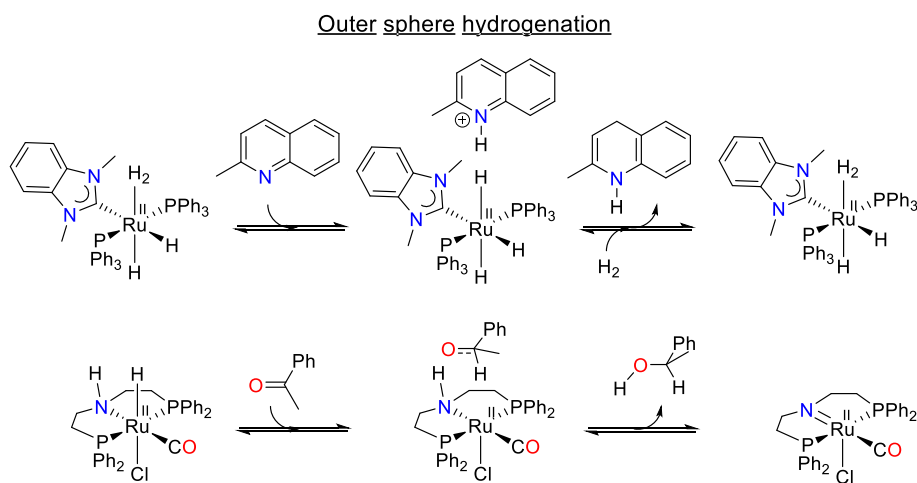
Figure 1.5 Examples of outer sphere reaction mechanisms for homogeneous catalytic double-bond hydrogenations.

1.2 Amides as a substrate.

Amides and carboxamides are the names given to molecules containing the functional group $R^1C(=O)NR^2R^3$. Due to their natural abundance and synthetic accessibility, amides play prominent roles in several contexts, such as biochemistry, synthesis of industrial and fine chemicals,[17–22] in processes of CO_2 conversion to methanol[23–26] as well as amine precursors. Amides belong to the family of carboxylic acid derivatives: electron-rich carbonyl groups of the form $RC(=O)Y$, which are susceptible to be hydrolyzed to carboxylic acids (Figure 1.6). Amides are the most stable within that family, which is a desired feature for example in their biological role in protein's peptide bonds. However, amides relative high stability is a drawback when they are used as a substrate since their reactivity is more challenging and slower than that of carboxylic acid derivatives.

Most reactive   **Least reactive**
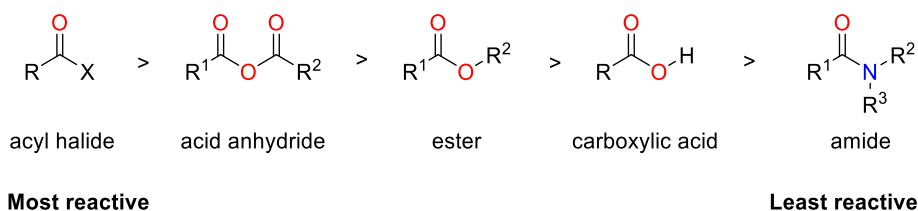
Figure 1.6 Relative reactivity and electron affinity of carboxylic acid derivatives.

Traditionally, methods for amide reduction relied on the consumption of stoichiometric amounts of strong reducing agents, such as $LiAlH_4$ or $LiBH_4$ and/or heterogeneous catalysts that demand very high pressures (>100 atm).[27–30] To date, only a small number of homogenous catalysts can directly hydrogenate amides to amines.[23,31–36] The thesis presents

our efforts to understand and improve the deaminative hydrogenation of amides by **M^H-PN^{H}P** catalysts. Therefore, it is important to contextualize the origin of amides low activity, as well as the reactions in which they can get involved.

1.2.1 **Amides reactivity**

Although amides are the least reactive of the carboxylic acid derivatives, they still do react under appropriate conditions. Amides can undergo nucleophilic addition (Figure 1.7) via a nucleophilic attack to the carbonyl carbon, and formation of an alkoxide molecule, which will later undergo either an oxygen protonation or an amine elimination.
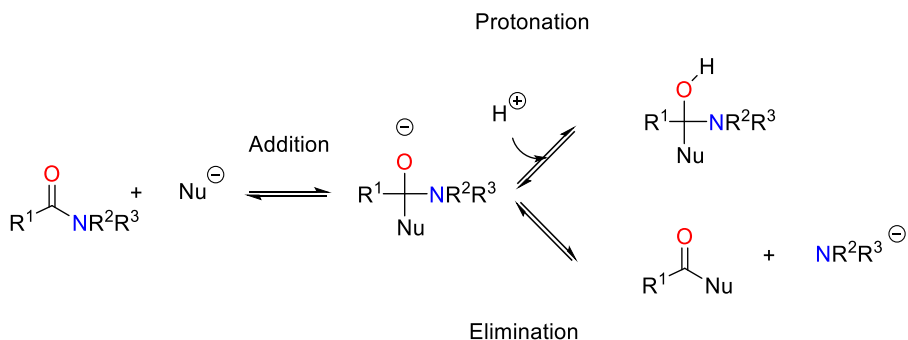
Figure 1.7 General amide reactivity.

Most of amides main reactions (see Figure 1.8) result from the combination of these fundamental steps with different nucleophiles and reaction conditions. We can differentiate two amide reaction families: those which involve C-N cleavage (with amine elimination), and those which involve C=O cleavage (with water elimination). C-N cleavage reactions can proceed with five different nucleophiles (alcohols, water,
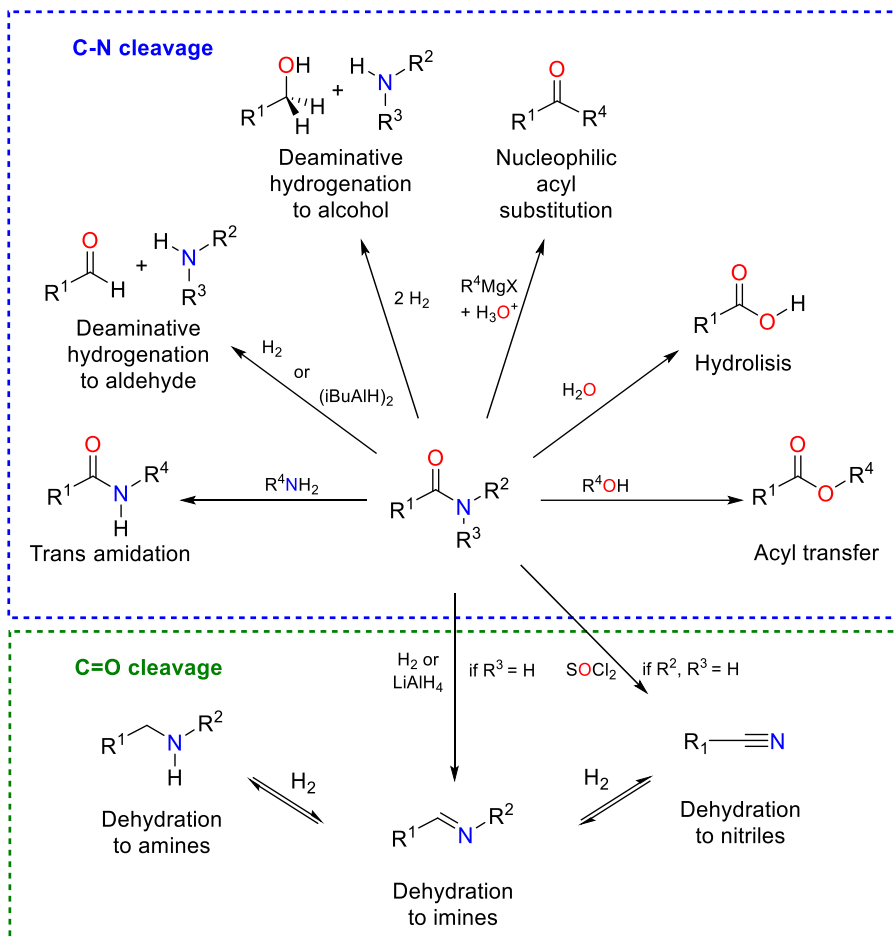
Figure 1.8 Schematic summary of amide reaction types. In blue: reactions involving C-N cleavage. In green: reactions involving C=O cleavage.

amines, Grignard reagents and hydrogen), leading to six different reactions types: acyl transfer, hydrolysis, trans amidation, nucleophilic acyl substitution, deaminative hydrogenation to aldehyde[37] (similar to the Vilsmeier-Haack reaction) and deaminative hydrogenation to alcohol. [37,38] In the case of C=O cleavage, the reaction can lead to three different products (amine, imine and nitrile) depending on the amide, the

catalyst or the reaction conditions. In some cases, mixed products can be formed.

Though all those reaction types are worth a chapter by themselves, they fall out of the scope of the thesis. Extensive reviews on amides C-N and C=O cleavage were written by J. Blanchet,[39] A. Y. Khalimon et al. .[40] and A. Smith and R. Whyman.[27]

1.2.2 **Electronic properties**

Amides stability is often associated with their multiple resonance forms (see Figure 1.9). In terms of Lewis theory, amides possess six conjugated electrons over the O-C-N moiety, resulting in the formation of three possible resonant forms. Such electron delocalization gives planarity and rigidity to the O-C-N moiety while contributing to amide's stability.
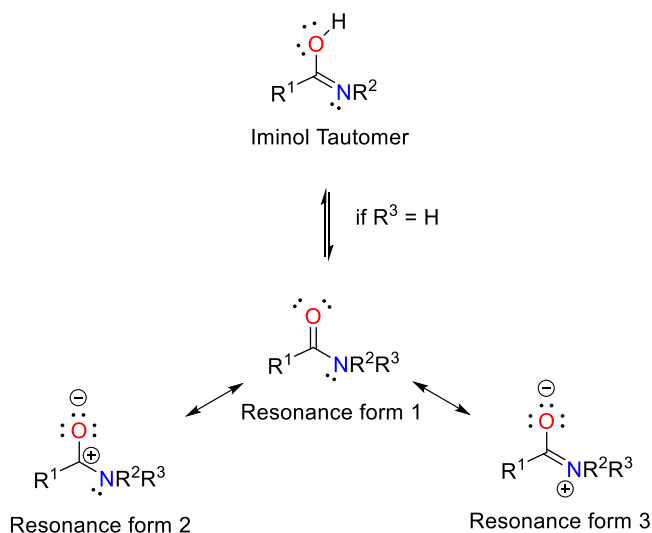
Figure 1.9 Amides resonance and tautomeric forms. Iminol tautomerization is only accessible from primary and secondary amides ($R^3 = H$).

11

Resonance forms 2 and 3 play an important role in the reactivity of amides. Nucleophilic additions to amides formally proceed through the resonance form 2 (see Figure 1.9). However, resonance form 3 (see Figure 1.9) strengthens the C-N bond reducing the C electrophilicity, and thus, depending on their weight in the electronic structure, can hamper nucleophilic additions. Amides with electron-withdrawing groups will have a stronger contribution of resonance form 2. Therefore, they will undergo nucleophilic additions faster than amides with electron donor groups, which have a stronger contribution of resonance form 3. The same rule applies to amides C-N cleavage reactions.

Alternatively, secondary and tertiary amides can transfer a proton from their N to their O to form an iminol tautomer (see Figure 1.9). The iminol tautomer hampers nucleophilic additions and C-N cleavages similarly to resonance form 3: it strengthens the C-N bond and reduces the C electrophilicity. The negative contribution of iminol tautomers can be reduced with the use of non-polar solvents, which disfavor their formation.

1.3 Deaminative hydrogenation of amides with bifunctional catalysts

The increasing pollution, and the necessity of renewable energies during the 21st century, has enforced a boost to green chemistry. Daily, new synthetic methods are being developed for the synthesis of industrial and fine chemicals with atom efficient reactions, renewable chemical

reagents, and mild reaction conditions. Deaminative hydrogenation of amides, the reaction studied in this work, is an example of such evolution. First attempts of deaminative hydrogenation of amides to alcohols without aggressive reagents were documented in 2003 within a patent.[41,42] That work was the first to use molecular hydrogen as hydrogen source instead of hydride sources like $LiAlH_4$ or hydroboranes. The hydrogenation reaction was achieved by using the ruthenium triphos catalyst [Ru(triphos)CO(H)$_2$] (see Figure 1.10). However, ruthenium is a precious metal, high temperatures and pressures were required and only modest Turn Over Number (TON) and Turn Over Frequency (TOF) were achieved (600 and 43 h^{-1} respectively).
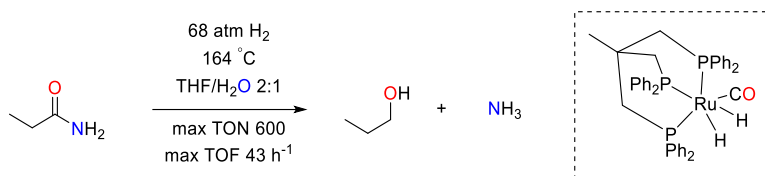
Figure 1.10 First homogeneous catalyzed deaminative hydrogenation of amides to alcohols with molecular hydrogen

Seven years later, in 2010, the Milstein group used for the first time a bifunctional catalyst for this reaction and it drastically reduced the required temperatures and pressures from 68 atm and 164 ºC to 10 atm and 110 ºC (entry **1** in Figure 1.11).[33] From then onward, bifunctional catalysts gained popularity and rapidly dominated the homogeneous catalysis of deaminative hydrogenation of amides to alcohols: bidentate Noyori- and Milstein-type catalysts were introduced in this reactions in 2011 and 2013 (entries **2** and **3** in Figure 1.11),[34,43–46] tridentate Noyori-type catalysts were reported in 2015 (entry **4** in Figure 1.11) [25,35,47] and base metal tridentate Milstein- and Noyori-type catalysts in 2016 (entries **5** and **6** in Figure 1.11).[36,48,49] This was the state of the art when this project started in the second half of 2016.

More recently, during the course of this research, deaminative hydrogenation of amides by Noyori-type catalysts has been expanded from ruthenium[50] and iron[31,51–53] to molybdenum[54] and manganese[23,55] with modest TONs and TOFs (entries **1** and **2** in Figure 1.12). Ruthenium and iron catalysis went through reaction optimization, emerging as the most active catalysts for this reaction, with maximum TONs up to 19600 and 5180, and TOFs up to 980 and 1108 h^{-1}, respectively (entries **3** and **4** in Figure 1.12).
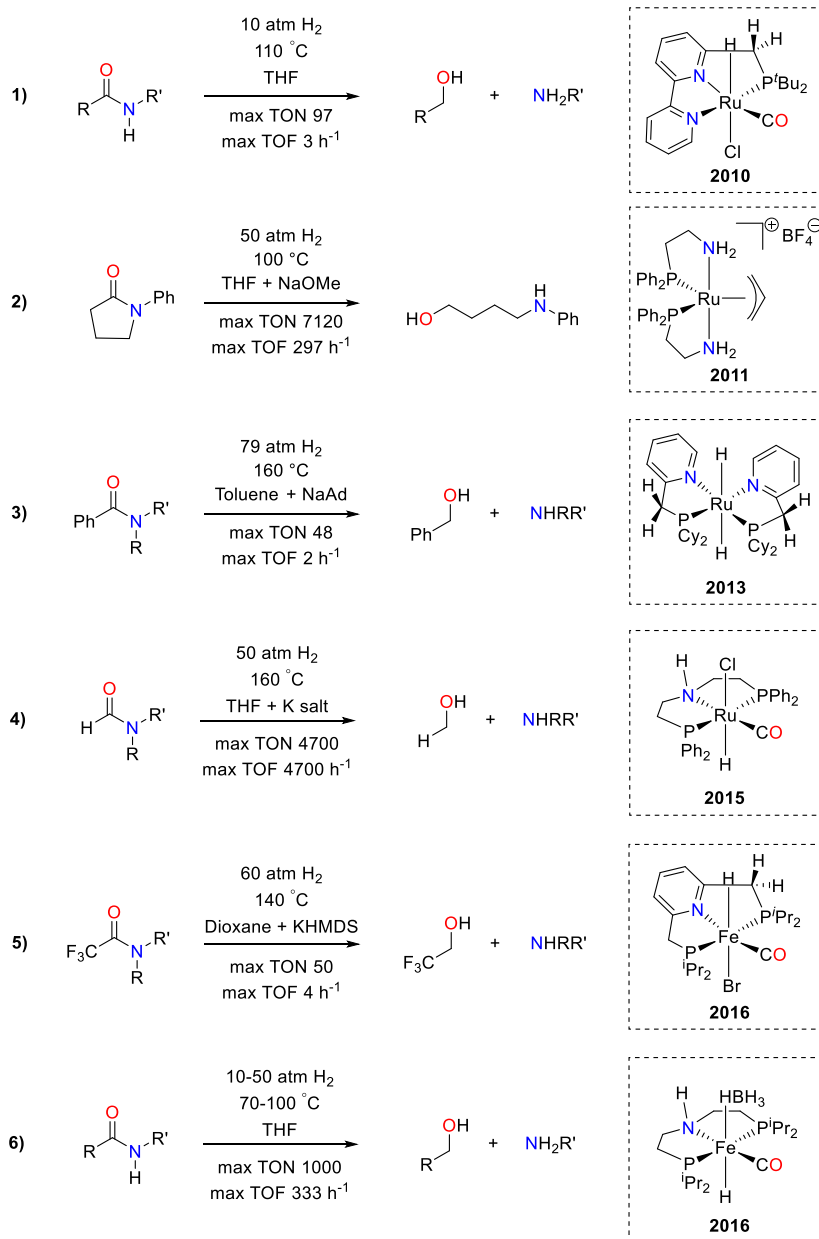
Figure 1.11 Historical evolution of bifunctional catalyst utilization in the deaminative hydrogenation of amides to alcohol until 2016.
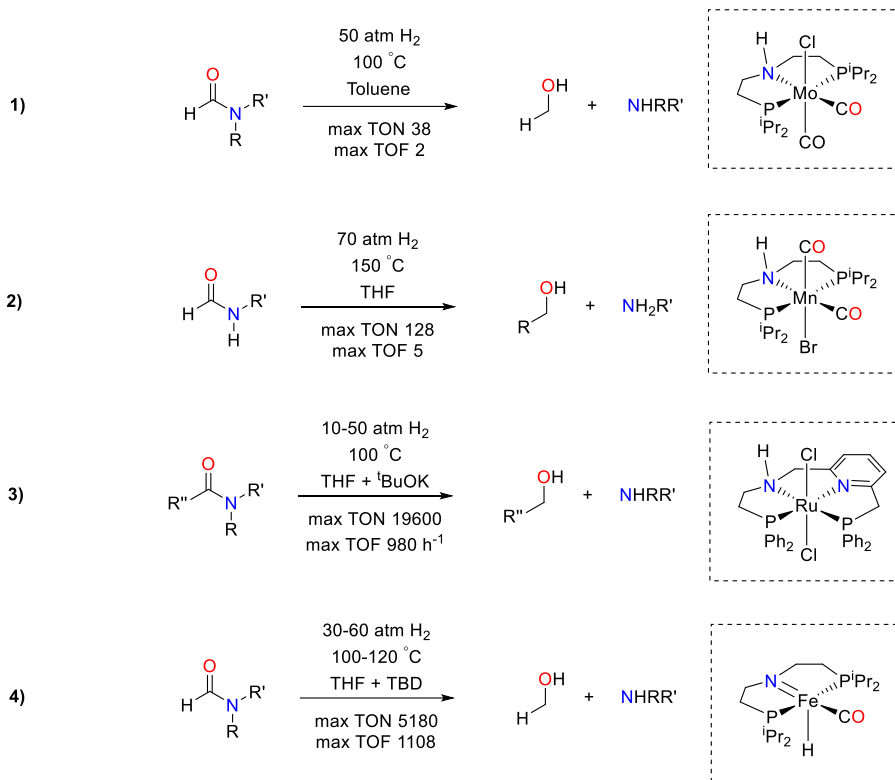
Figure 1.12 State of the art of amide deaminative hydrogenation catalyzed by Noyori-type catalysts in 2020.

1.3.1 Fe-PNP Catalyzed Deaminative Hydrogenation of Amides

In 2020, the Noyori-type bifunctional catalyst **Fe-PNP** (see Table 1.1) was the non-noble metal homogeneous catalysts with the best performance at the time for the deaminative hydrogenation of amides. The first iron Noyori-type catalyst was first synthesized in 2013 by M. Beller and co-workers, who used it as a catalyst for methanol dehydrogenation.[56] This catalyst strongly gained popularity in the next

two years for its ability to hydrogenate the double bonds of a wide variety of substrates, including esters, carbon dioxide, alkenes, heterocycles and nitriles.[57–62] In 2016, iron Noyori-type catalysts was used for the first time for deaminative hydrogenation of amides, by Langer and coworkers[48] and by Sanford and co-workers.[49] The catalyst exhibited selectivity towards the reduction of aryl formamides and benzamides with promising activities: TONs and TOFs up to 177 and 59 h^{-1} respectively, under mild conditions of 110 ºC and 20 bar; and TONs and TOFs up to 1080 and 100 h^{-1} in the presence of K_3PO_4, temperature of 110 ºC and H_2 pressure of 60 bar.

A key milestone for the project came in 2017 in a new study published by Hazari, Bernskoetter and co-workers.[31] This paper presented three main results: (I), they presented a catalyst optimization: utilization of the dehydrogenated catalyst **Fe-PNP** reached TONs and TOFs up to 4430 and 1108 h^{-1} (see Table 1.1); (II), they reported that the conversion of alkyl formamides and benzamides is enhanced by the presence of secondary aryl amides or LiOTf (see Table 1.2); and (III), they reported the formation of adducts between **Fe-PNP** and secondary amides in the absence of hydrogen (see Figure 1.13), similar to those observed between **Fe-PNP** and methanol or formic acid.[63] Interestingly, secondary amides and/or LiOTf had no catalytic effect on secondary amides.
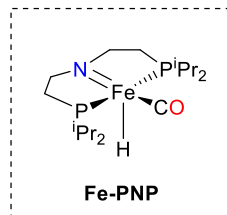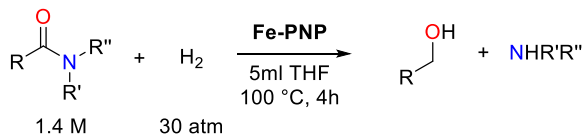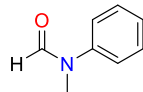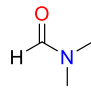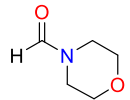
Amide/substrate	[Fe-PNP]	Conv. (%)	TON // TOF (h^{-1})
	1 mM 0.25 mM	>99 79	>1400 // >350 4430 // 1108
	1 mM 0.25 mM	>99 58	> 1400 // > 350 3240 // 810
	1 mM 0.25 mM	97 36	1360 // 340 2000 // 500
	1 mM	9	130 // 33
	1 mM	4	60 // 15
	1 mM	0	-- // --

Table 1.1 Summary of the results reported by Hazari, Bernskoetter *et al.* on the **Fe-PNP**-catalyzed deaminative hydrogenation of different secondary and tertiary amides.[31]
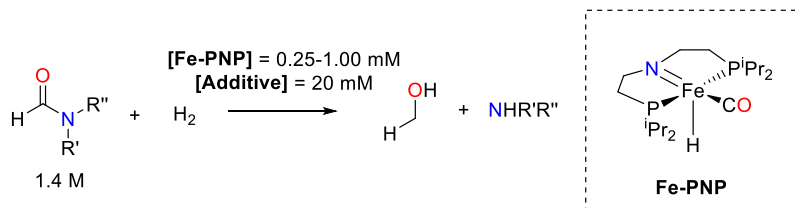
Amide/substrate	Additive	Conv. (%)	TON // TOF (h^{-1})
a	4'-Trifluoromethylformanilide	> 99	> 1390 // 348
	Formanilide	93	1305 // 326
	4'-Methoxyformanilide	78	1098 // 275
	Aniline	24	335 // 84
	Benzanilide	12	168 // 42
	---------------	4	60 // 15
b	Formanilide + LiOTf	24	340 // 21
	Formanilide	14	190 // 12
	----------------	4	50 // 3
c	Formanilide + LiOTf	54	3010 // 188

Table 1.2 a) 30 atm H_2, 100 ºC, 1 mM of **Fe-PNP**, 4h. b) 60 atm H_2, 120 ºC, 1 mM of **Fe-PNP**, 16h. c) 60 atm H_2, 120 ºC, 0.25 mM of **Fe-PNP**, 16h.
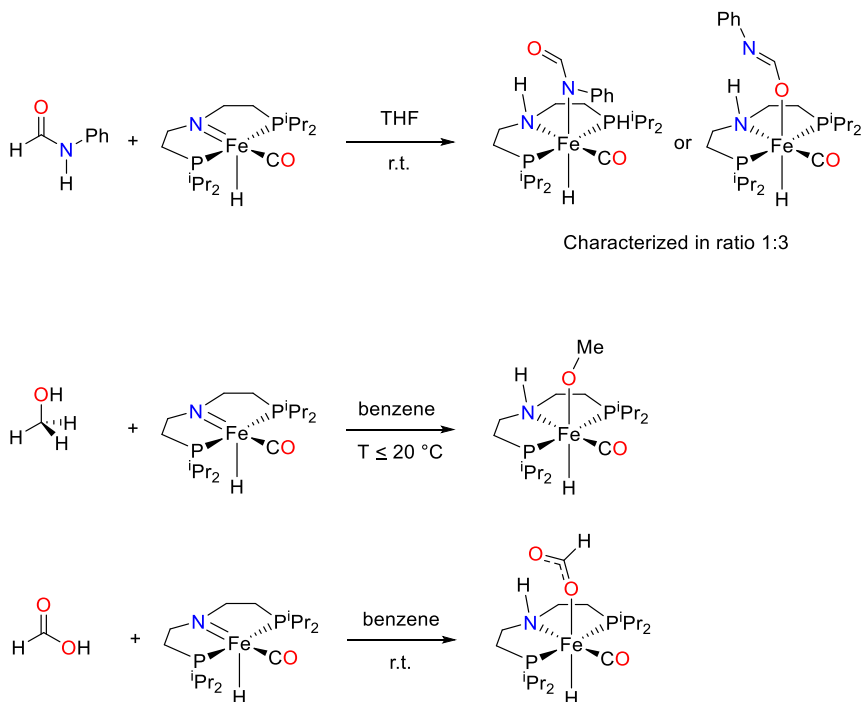
Figure 1.13 Experimentally observed adducts of **Fe-PNP** when treated with stoichiometric amounts of formanilide, methanol and formic acid (in the absence of hydrogen).[31,63,64]

1.3.2 Mo^Cl^-PN^H^P Catalyzed Deaminative Hydrogenation of Amides

Mo^Cl^-PN^H^P (see Table 1.3) was first synthesized in 2018 by M. Beller and co-workers, as an alternative of **Fe-PNP**.[54,65] **Mo^Cl^-PN^H^P** could hydrogenate ketones, olefines, amides, though it had modest TONs and TOFs when compared to **Fe-PNP**. Still, it exhibited an opposite selectivity within amides: **Mo^Cl^-PN^H^P** performance was good in the deaminative hydrogenation of tertiary aryl amides, but it was barely active for acetamides or secondary aryl amides, and inert for aliphatic

formamides. Similarly to **Fe-PNP**, **Mo^{Cl}-PN^{H}P** favoured the deaminative hydrogenation of formamides, or amides with electron-withdrawing groups, over other amide types with electron-donor groups.

The activation of **Mo^{Cl}-PN^{H}P** pre-catalyst formally requires the elimination of HCl to allow the addition of H_2. This reaction was performed using NaBHEt$_3$, yielding Mo(0) d^6 **Mo-PNP** and hydrogen elimination (Figure 1.14). The formation of **Mo-PNP** was supported by HR-ESI-MS (High-Resolution Electron Spray Ionization Mass Spectroscopy), and by an inactive Electron Paramagnetic Resonance (EPR).

Mo^{Cl}-PN^{H}P was reported to form adducts in the presence of formanilide and NaHBEt$_3$ (Figure 1.14), in a similar fashion to **Fe-PNP**. The resulting compound was characterized by single-crystal X-ray diffraction, as a Mo(0) dimeric complex. The formed adduct catalyzed the deaminative hydrogenation of amides in the absence of NaBHEt$_3$, reinforcing the hypothesis that Mo(0) d^6 **Mo-PNP** is the active catalyst.

Mo^{Cl}-PN^{H}P + NaBHEt$_3$

12.5 mM

2 ml toluene
100 ºC 24 h

0.25 M

H$_2$

50 atm
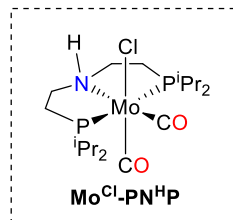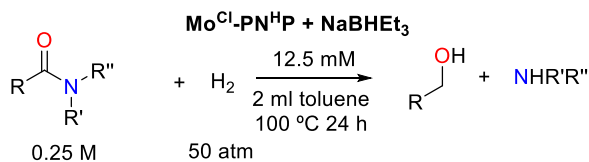
Amide/substrate	Conv. (%)	TON // TOF (h^{-1})
	>99	20 // 1
	>99 94[a]	20 // 1 38[a] // 2[a]
	83	17 // 1
	20	4 // 0
	13	3 // 0
	<1[b]	0[b] // 0[b]

Table 1.3 Brief summary of the experimental results reported by M. Beller and co-workers on the **Mo^{Cl}-PN^{H}P** catalyzed deaminative hydrogenation of amides.[54] a) **[Mo^{Cl}-PN^{H}P + NaBHEt$_3$]** = 6.25 mM. b) T = 130 °C.
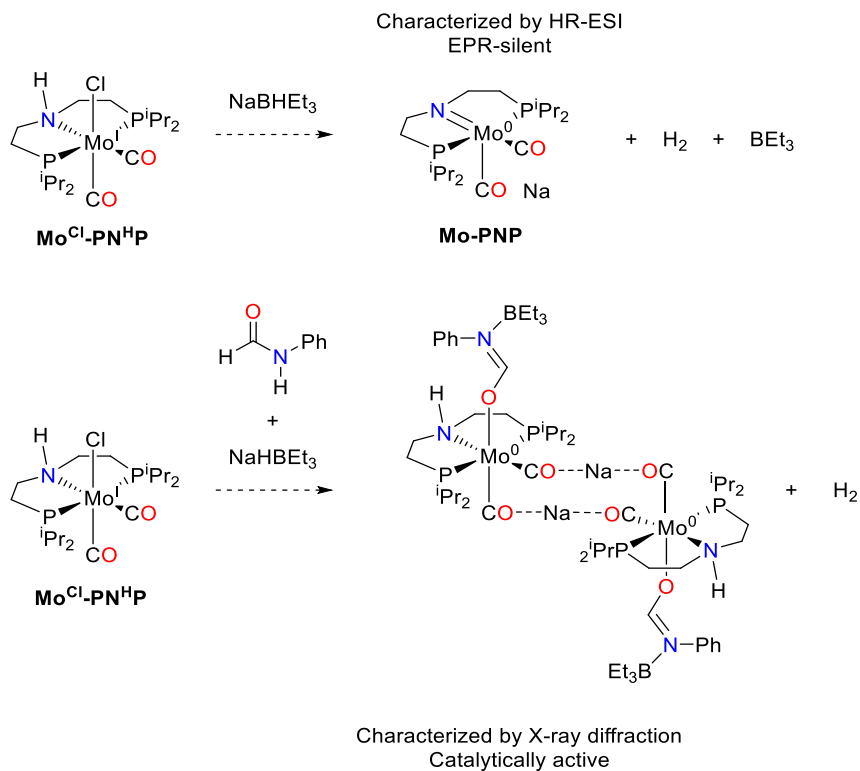
Figure 1.14 Mo^{Cl}-PN^{H}P activation by NaBHEt$_3$ (above) and by NaBHEt$_3$ plus formanilide (below).[54] The dashed arrow indicates the lack of experimental information to have reaction mass balance.

2 Methods

The workflow used in this study (see Figure 2.1) consisted on (I) benchmarking different methods to experimental and theoretical references (described in Appendix) to select a density functional that accurately described our system, (II) computing reaction mechanism guesses, by Density Functional Theory (DFT) calculations, (III) using the computed energies to generate a microkinetic model of the reaction mechanism, (IV) comparing the results of the microkinetic model against experimental measures. New reaction mechanisms were calculated in case of discrepancies between calculations and experiments.
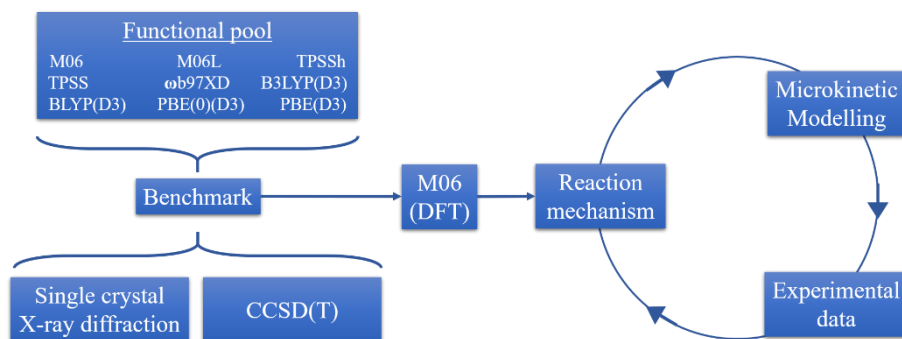
Figure 2.1 Work-flow chart used in this research.

2.1 Density Functional Theory (DFT)

DFT is the method used in this research for the calculation of ground-energies and geometries. DFT, was selected among other computational methods because its accuracy *vs* computational-cost ratio allowed for the

calculation of free energies with sufficient accuracy and within a reasonable time span.

DFT was first proposed in 1927 by Thomas and Fermi, and its bases were founded in 1964 by Hohenberg and Kohn, who enunciated and proved their two theorems:[66,67] (I) an electron density function $\rho(\vec{r})$ (see Eq 2-1 and Eq 2-2) can adopt the role of a "function that defines the state of a system" and hence define all the properties of the ground state; and (II) the functional $F_{HK}[\rho]$ delivers the ground state energy of the system if and only if the input $\rho(\vec{r})$ and potential field $v(\vec{r})$ match those of the real ground state (see Eq 2-3).

Eq 2-1

$$\rho(\vec{r}) = n \int \cdots \int |\Psi(\vec{r}_1, s_1, \vec{r}_2, s_2, \dots \vec{r}_n, s_n)|^2 \, ds_1 d\vec{r}_2 ds_2 \dots d\vec{r}_n ds_n$$

$$\int \rho(\vec{r}) d\vec{r} = n \qquad\qquad \textbf{Eq 2-2}$$

$$E[\rho] = \int \rho(\vec{r}) v(\vec{r}) d\vec{r} + F_{HK}[\rho] \qquad\qquad \textbf{Eq 2-3}$$

Although the Hohenberg-Kohn theorems are rigorously correct, they do not yield an analytical expression for $F_{HK}[\rho]$, which remains unknown. Therefore, further approximations were needed to make DFT applicable to computational chemistry.

2.1.1 **Kohn-Sham Equations**

In 1965, Kohn and Sham reformulated Hohenberg and Kohn's theory into a computationally implementable DFT approximation. Kohn and Sham proved that the solution of an ideal system with non-interacting electrons and with a density function ρ_{KS}, can reproduce the energy of a real system if ρ_{KS} is equal to that of the real system.[68]

The advantages of using an ideal system are that it can be defined with a kinetic energy operator $\hat{T}_{el}$, and an external potential V^{KS} that artificially simulates the real electron-electron repulsion (see Eq 2-4). This ideal system can be expressed in terms of the one-electron operator $\hat{h}^{KS}(\vec{r})$, similar to the Fock operator.

$$\hat{H}^{KS} = \hat{K}_{el} + V^{KS} = \sum_{i=1}^{n} \left(-\frac{\nabla_i}{2} + v^{KS}(\vec{r}_i) \right) = \sum_{i=1}^{n} \hat{h}^{KS}(\vec{r}_i) \qquad \textbf{Eq 2-4}$$

v^{KS} in Eq 1-4 is the potential field that a single electron feels from the ideal nuclei-electron interaction, $v_{ne}(\vec{r})$, the ideal electron-electron interaction, $\int \frac{\rho_{KS}(r\prime)}{|r-r\prime|} dr'$, and the non-ideal electron-electron repulsion, $\frac{\delta E_{xc}[\rho_{KS}]}{\delta \rho_{KS}}$ (see Eq 2-5). Kohn and Sham named E_{xc} the exchange-correlation energy.

$$v^{KS}(\vec{r}) = v_{ne}(\vec{r}) + \int \frac{\rho_{KS}(r')}{|r - r'|} dr' + \frac{\delta E_{xc}[\rho_{KS}]}{\delta \rho_{KS}} \qquad \textbf{Eq 2-5}$$

An exact mathematical expression of $E_{xc}[\rho_{KS}]$ is unknown and all further DFT methods focus on finding an approximation of E_{xc}. Once a E_{xc} approximation has been selected, an initial guess wavefunction Ψ^{HF} can be used as an input in Eq 2-1 to obtain a ρ_{KS} guess, which can be input in Eq 2-5 to calculate a v^{KS} guess, which at the same time can built a $\hat{h}^{KS}$ guess. Then $\hat{h}^{KS}(\vec{r})\psi^{KS}(\vec{r}) = \varepsilon^{KS}\psi^{KS}(\vec{r})$ can be solved iteratively to find all ψ^{KS} until a self-consistent $\rho_{KS}(\vec{r})$ is found. It is at this point when $\rho_{KS}(\vec{r})$ can be used to calculate the energy of the system (see Eq 2-6) whose components are: kinetic energy $T^{KS}[\rho_{KS}]$, Coulomb energy $J^{KS}[\rho_{KS}]$, nuclei-electron potential energy $E_{ne}[\rho_{KS}]$ and exchange-correlation energy $E_{xc}[\rho_{KS}]$.

$$\rho_{KS}{}^0 \;\longrightarrow\; v^{KS\,0} \;\longrightarrow\; \left(\hat{h}^{KS}\right)^0 \longrightarrow\; \{\psi_1^{KS\,0}, \psi_2^{KS\,0}, \dots \psi_n^{KS\,0}\}$$

$$\hookrightarrow \rho_{KS}{}^1 \;\longrightarrow\; v^{KS\,1} \;\longrightarrow\; \left(\hat{h}^{KS}\right)^1 \longrightarrow\; \{\psi_1^{KS\,1}, \psi_2^{KS\,1}, \dots \psi_n^{KS\,1}\}$$

$$\hookrightarrow \cdots = \cdots \longrightarrow \cdots \longrightarrow \cdots$$

$$\hookrightarrow \rho_{KS} = \rho_{real}$$

$$E[\rho_{KS}] = K^{KS}[\rho_{KS}] + J^{KS}[\rho_{KS}] + E_{ne}[\rho_{KS}] + E_{xc}[\rho_{KS}] \qquad \textbf{Eq 2-6}$$

The fundamental difficulty in DFT is that we do not know the exact expression of the exchange-correlation energy $E_{xc}[\rho_{KS}]$. Many approximations of $E_{xc}[\rho_{KS}]$ have been proposed since Kohn and Sham published their computable implementation of DFT. However, there is not a $E_{xc}[\rho]$ approximation that generally outperforms all the others.

Therefore, a benchmark of methods against an experimental or computational reference is recommended.

In the thesis, the hybrid *meta*-GGA M06[69] functional was selected on the basis of geometry and energy benchmarks (see Appendix), using X-ray crystal structures and CCSD(T) (also known as the golden standard method to obtain accurate bond energies),[70] with basis set cc-pVTZ.[71]

2.1.2 **M06**

M06, the functional used in the thesis for the calculation of molecular ground energies, is a hybrid meta-exchange-correlation functional created in 2008 by Truhlar and co-workers. It belongs to the family of the so-called Minnesota functionals.[69] M06 is a highly parametrized functional, specifically optimized to reproduce the thermochemistry of main group elements and organometallic compounds. M06 was also optimized to reproduce non-covalent interactions of main croup elements. A total of 36 parameters were fitted against databases with empirical measures and highly accurate calculations of both transition metals and non-metal elements. These databases contained over 403 energetic data points of thermochemistry, kinetics, non-covalent and metallic bonding and excitation energies. M06 accurately describe dispersion forces thanks to the inclusion of second derivatives of the density function.

M06 energies can be decomposed in three components: 27% of Hartree-Fock exchange energy, 73% of pure M06 exchange energy, and 100 % of M06 correlation functional (see Eq 2-7).

$$E_{xc}^{M06}[\rho, x_\sigma, \tau_\sigma] = 0.27 E_x^{HF} + 0.73 E_x^{M06} + E_C^{M06} \qquad \textbf{Eq 2-7}$$

The inclusion of Hartree-Fock exchange makes M06 a hybrid functional. Also, M06 is classified as a meta-GGA functional because it depends on the variables electron density (ρ_σ), reduced spin density gradient (x_σ), and spin kinetic energy density (τ_σ).

2.2 Solvent Modelling

The free energy of a system, and hence its reactivity, can be severely altered by the presence or absence of a surrounding condensed phase. Inclusion of solvent modelling is critical in systems with relevant interaction between solvent and solute, like those found in ionic solvents or solutes, solvents with the possibility to coordinate or hydrogen bond with the solute, reactions involving proton transfers, etc. The effect of a solvent in the free energy of a system receives the name of solvation free energy, ΔG_S°, and it is divided into three terms (see Eq 2-8):[72] (1) ΔG_{ENP} which contains the effect of electrostatic interactions between charges on the solute and charges on the solvent molecules (acronym of Electrons and Nuclei Polarization from gas- to liquid-phase); (2) ΔG_{CDS}, which contains the effect of non-electrostatic interactions (acronym of solvent Cavitation energy, Dispersion energy and local Solvent reorganization energy); and (3) ΔG_{conc}°, which contains the change in

free energies due to differences in standard state concentration between gas and liquid-phase (1.89 kcal mol^{-1} if 1 atm and 1 mol L^{-1} are used in the gaseous and solvated-phase respectively).

$$\Delta G_S^\circ = \Delta G_{ENP} + \Delta G_{CDS} + \Delta G_{conc}^\circ \qquad \textbf{Eq 2-8}$$

The modelling of a condensed-phase system is not trivial. The most realistic way to construct a model is to surround the solute with a finite number of solvent molecules (explicit solvent modelling) (see left scheme in Figure 2.2). However, the high number of solvent molecules surrounding the solute (which increases as the square of the radius of the simulated cell) implies the computation of an impracticable number of particle interactions and energy minimums, only computable by simulation techniques such as molecular dynamics.

Implicit continuum solvation modelling emerged as an alternative to implicit solvent modelling. The assumptions underlying implicit continuum solvation models are that (I) solvent molecules do not react with the solute, and (II) the huge number of individual solvent molecules may be replaced by a continuous medium with properties consistent with those of the solvent itself (see right scheme in Figure 2.2).[73,74] Some implicit models are: PCM,[75] IEF-PCM,[76] SMD,[72] SMD12,[77] COSMO,[78] MCSCRF[79] or FEM.[80]

Alternatively to implicit or explicit solvent modelling, hybrid implicit-explicit solvation models can be used (see middle scheme in Figure 2.2). Hybrid solvation models typically consist of a continuous medium that surrounds a solute and few solvent molecules. Such approximation is

usually used when solvent reactivity is expected but full explicit solvent simulation is computationally too expensive. It is in these cases when hybrid solvation models shine thanks to their computational cost in between that of implicit and explicit models.

| Explicit solvation model | Hybrid solvation model | Implicit solvation model |
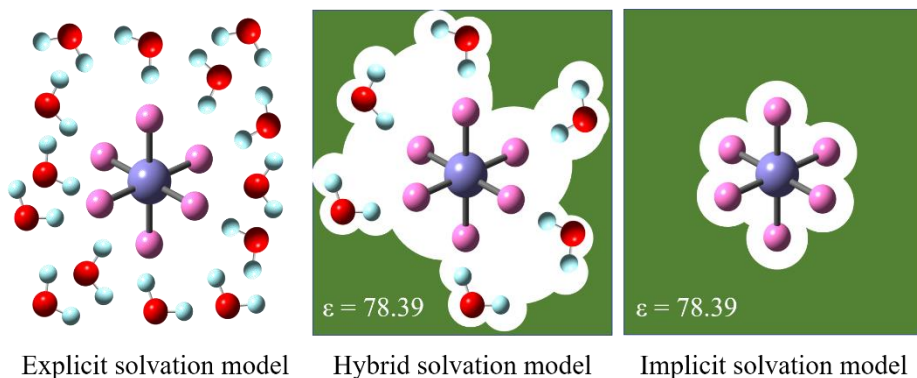
Figure 2.2 Toy systems of explicit, hybrid and implicit solvation models.

In the thesis, implicit models have been used because solvent reactivity was not expected (i.e. the simulated solvent, toluene and thf, are aprotic and non-coordinating molecules), and the big size of our system made the computational cost of explicit solvation modeling not practical for this study. Instead, the method Solvent Modeled Density (SMD) was used to introduce solvation free energy corrections to DFT calculated free energies. SMD is an implicit continuum solvent model developed in 2009 by A. Marenich, C. Cramer and D. Truhlar.[72] The SMD modelling of ΔG_{ENP} is a parametrized version of the Polarized Continuum Model approximation (PCM) (more specifically the IEF-PCM). In PCM, the Born-Oppenheimer approximation (B.O.) of clamped nuclei is assumed. B.O. implies that the dielectric field of the solvent does not polarize the solvated nuclei, therefore, the system

wavefunction is reduced to the electronic component and ΔG_{ENP} will be treated as ΔG_{EP} which is equal to Eq 2-9,

Eq 2-9

$$\Delta G_{EP} = \left\langle \Psi_{sol.} \middle| \widehat{H}_{gas} - \frac{e}{2}\phi \middle| \Psi_{sol.} \right\rangle + \frac{e}{2} \sum_{A}^{N} Z_A \phi_A - \left\langle \Psi_{gas} \middle| \widehat{H}_{gas} \middle| \Psi_{gas} \right\rangle$$

where ϕ (a.k.a. reaction field) is the electrostatic potential caused by the solute dipole moment and the solvent polarization. ϕ can be calculated with the Poisson equation (see Eq 2-10) which relates the solvent dielectric constant ϵ, and the charge density of the solute ρ_f. ϕ and ρ_f depend reciprocally on each other; hence they must be solved iteratively in a self-consistent process named Self-Consistent Reaction Field (SCRF).

$$\nabla \cdot (\epsilon \nabla \phi) = -4\pi \rho_f \qquad \textbf{Eq 2-10}$$

The SMD modelling of ΔG_{CDS} is a sum of terms that are proportional (with geometry-dependent proportionality constants σ, called atomic surface tensions) to the solvent-accessible surface areas of the individual atoms of the solute (A) (see Eq 2-11, where k and M refer to solute and solvent atoms respectively). Surface tension σ are parameterized constants of atoms k or M, characteristic of the SMD model, and they have no particular connection with conventional surface tension. In the SMD model, the Solvent-Accessible Surface Area is calculated as the area created by the addition spheres centred in the solute atoms, and with

a radius equal to the sum of the atom van der Waals radii plus the solvent radius.[6]

$$\Delta G_{CDS} = \sum_{k}^{N} \sigma_k A_k + \sigma^{[M]} \sum_{k}^{N} A_k \qquad \textbf{Eq 2-11}$$

2.3 Microkinetic modelling

The prediction of a reaction experimental macroscopic behaviour from its calculated reaction mechanism is often not straight forward. To achieve a deeper understanding of the studied reaction mechanisms, microkinetic models were constructed. Microkinetic modelling is a computational technique directed to solve the apparent rate of a reaction mechanism from the calculation of its elementary step rates. Using microkinetic models, one can obtain a set of concentrations and rates as a function of time (see Figure 2.3) from a complete set of elementary reactions and their rate constants (usually obtained with computational studies), and the initial reaction concentrations and conditions. These models facilitate the interpretation of complex reaction networks, like competing reactions or interconnected reactions cycles.
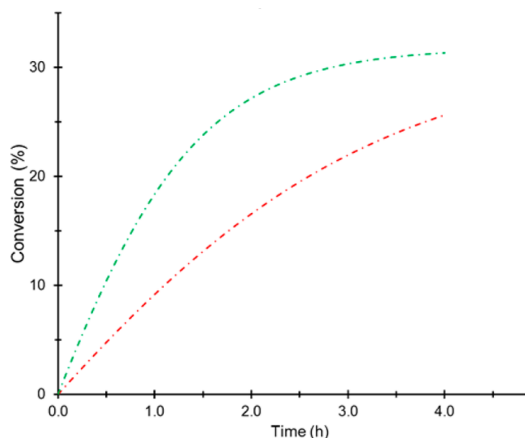
Figure 2.3 Example of a microkinetic model output of a toy reaction were the green and red lines are the conversion of two reactants (Conversion$_t$ = 100 * [Reactant]$_t$ / [Reactant]$_0$).

Microkinetic modelling is based on transition-state theory. Transition-state theory states that reaction mechanisms can be decomposed in elementary reactions: unidirectional reactions of one or more reactants or intermediates in *quasi-equilibrium* with a single activated transition state complex $X^{\ddagger}$ that irreversibly leads to one or more product or intermediates (see Figure 2.4).[74,81,82]
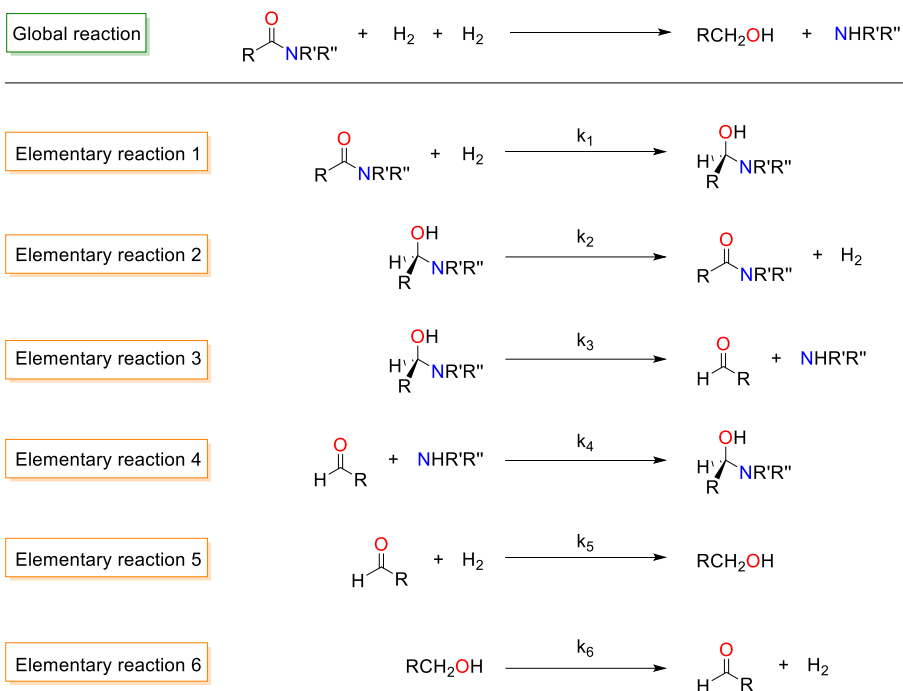
Figure 2.4 Toy example of a fictional reaction mechanism and its elementary reactions.

The velocity of an elementary reaction is proportional to the product of the concentration of its reactants, as described by Eq 2-12,

$$elementary\ reaction\ rate = k \prod_i [R_i]$$

<div align="right">**Eq 2-12**</div>

$$k = \frac{\kappa k_B T}{h} e^{-\frac{\Delta G^{\ddagger}}{RT}}$$

where k is a rate constant, k_B is the Boltzmann constant, T the reaction temperature, h the Planck constant, $\Delta G^{\ddagger}$ the free energy barrier of the elementary reaction, R is the ideal gas constant, and κ is transmission

coefficient (accounting for the phenomenons of tunnelling and "re-crossing").[81] Consequently, the macroscopic behaviour of any molecule R_i in a reaction mechanism is described by an ordinary differential equation (ODE) of the form of Eq 2-13,

$$\frac{\partial[R_i]}{\partial t} = [R_i] \sum_j k_j \prod_{a \neq i}[R_a] - [R_i] \sum_l k_l \prod_{b \neq i}[R_b] \qquad \textbf{Eq 2-13}$$

where j are the elementary reactions in which R_i is a reactant and R_a their reactants, and l are the elementary reactions in which R_i is a product and R_b their reactants.

The ODEs of a reaction mechanism are usually intercorrelated, and their analytical solution is unknown. Microkinetic modelling software offers several algorithms that numerically solve ODEs and allow us to simulate the time-evolution of the concentration of all species involved in the reaction mechanism. COPASI (COmplex PAthway SImulator)[83] is the software package used in the thesis for microkinetic modelling. COPASI solves ODE with the algorithm LSODA (Livermore Solver for Ordinary Differential Equations "Automatic").[84–87] LSODA automatically detects the stiffness of the evaluated ODE and determines which numerical method should be used to solve it: the Adam method for non-stiff ODEs and the Backward Differentiation Formula (BDF) for stiff ODEs.[84]

3 Objectives

The main goal of the thesis was the computational determination of the reaction mechanisms of the deaminative hydrogenation of amides by base metal Noyori-type catalysts. The secondary objective was the improvement of the reaction activity using the information given by the proposed mechanisms.

The reaction was studied with two catalysts, **Fe-PNP** and **Mo$^{\mathbf{H}}$-PN$^{\mathbf{H}}$P**. The different selectivity of these catalysts moulded the objective details of each reaction. While the **Fe-PNP**-catalyzed reaction mechanism should explain the different reactivity of secondary and tertiary amides, the **Mo$^{\mathbf{H}}$-PN$^{\mathbf{H}}$P**-catalyzed reaction mechanism should explain the different reactivity of formamides and acetamides. Despite their different selectivity, both catalysts were reported to form stable adducts with secondary amides such as formanilide. The thesis also aims to understand the formation of these adducts as well as their impact on the reaction outcome.

4 Results

This chapter summarizes the main findings obtained in the included papers. The central theme throughout this chapter is the computational mechanistic study on the deaminative hydrogenation of amides by either catalyst **Fe-PNP** or **Mo^{Cl}-PN^{H}P** (see Figure 4.1).
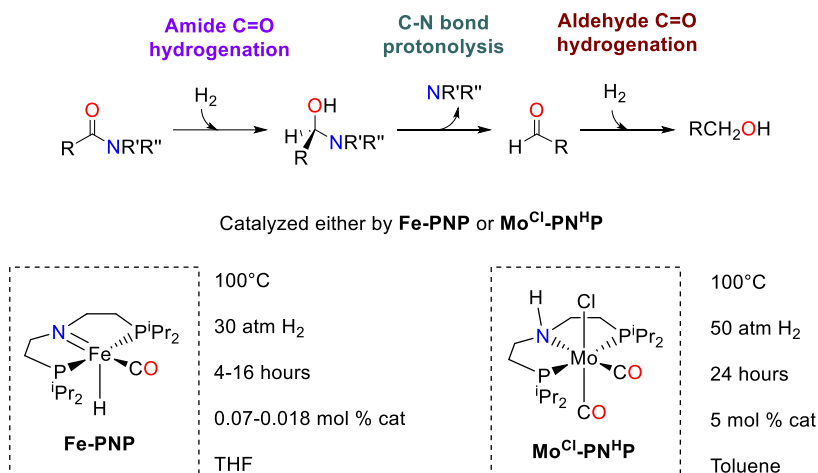
Figure 4.1 Above, commonly proposed elementary reaction steps on the deaminative hydrogenation of amides when in the presence of **Fe-PNP** or **Mo^{Cl}-PN^{H}P** catalysts. Below, studied catalysts and experimental conditions.

The overall reaction mechanism is based in three consecutive reaction steps (see Figure 4.1 and Figure 4.2):[64] amide C=O hydrogenation, C-N bond protonolysis and aldehyde C=O hydrogenation. This division is a proposal consistent with the ability of Noyori- and Milstein-type catalysts to hydrogenate carbonyl groups.[88,89] Although **M-PNP** catalysts are known to be involved in C=O hydrogenations, their role in C-N bond protonolysis remained unclear prior to the thesis. Hence, we considered adequate to investigate its role in C-N protonolysis too. We

have also studied the role of secondary amides, alcohols and other proton relay molecules. These species have been observed both to bind to the dehydrogenated catalysts and to co-catalyze the hydrogenation of some tertiary amides and esters.[31,63,64,88–91] Therefore, we included proton relay mechanisms for competitive catalyst inhibition, co-catalyzed C-N bond protonolysis and co-catalyzed **M-PNP** hydrogenations (see Figure 4.2).
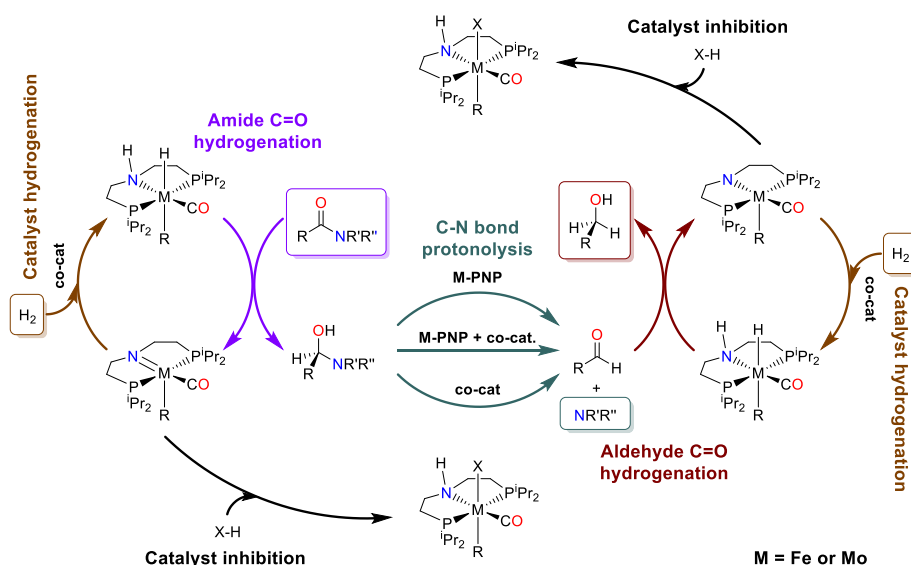
Figure 4.2 Studied interactions of **M-PNP** and co-catalysts in the elementary steps of deaminative hydrogenation of amides.

The amides used for this study are shown in Figure 4.3. The amides have been selected to cover a range of reactivity, substituents and steric hindrance. The selected amides for the **Fe-PNP**-catalyzed deaminative hydrogenation of amides are formanilide, morpholidine and dimethylformamide (DMF), and their experimental conversions are 58%, 36% and 0% respectively. The selected amides for the **Mo^{Cl}-**

PN^{H}P-catalyzed deaminative hydrogenation of amides are formanilide, N-methylformanilide and N-methylacetanilide, and their experimental conversions are 13%, >99% and 20% respectively. The lack of correlation between experimental conversions and the reaction thermodynamics indicates that deaminative amide hydrogenation behaviour is not thermodynamically but kinetically controlled. Substrate-dependent out-cycle reactions could also account for conversion differences between amides. **Fe-PNP** and **Mo^{Cl}-PN^{H}P** different selectivity (see the case of formanilide) suggests that their reaction mechanisms are different.

	Amide C=O hydrogenation	C-N bond protonolysis	Aldehyde C=O hydrogenation	

Fe-PNP — Calculated ΔG_r (kcal mol^{-1})

Substrate					Exp. Conv.
H–C(=O)NHPh	0.0	4.7	5.2	-10.1	58%
H–C(=O)N(morpholine)	0.0	8.8	12.4	-2.8	36%
H–C(=O)NMe$_2$	0.0	10.5	13.8	-1.5	No conversion

Mo^{H}Cl-PN^{H}P — Calculated ΔG_r (kcal mol^{-1})

Substrate					Exp. Conv.
H–C(=O)NHPh	0.0	4.0	5.1	-10.1	13%
H–C(=O)NMePh	0.0	7.6	6.8	-8.5	>99%
Me–C(=O)NMePh	0.0	10.5	0.6	-7.5	20%

Figure 4.3 Calculated free energies (kcal mol^{-1}) of organic key intermediates of selected amides, next to their experimental yields.[31,54] Experimental reaction conditions for the **Fe-PNP** catalyst are 1.4 M amide, 0.25 mM **Fe-PNP**, 30 atm H$_2$, 100 ºC and 4 hours in tetrahydrofuran (THF). Experimental reaction conditions for the **Mo^{Cl}-PN^{H}P** catalyst are 0.25 M amide, 12.5 mM **Mo^{Cl}-PN^{H}P**, 50 atm H$_2$, 100 ºC and 24 hours in toluene.

The hybrid *meta*-GGA M06 functional was selected on the basis of geometry and energy benchmarks,[69] using X-ray crystal structures and CCSD(T) [70] (with basis set cc-pVTZ)[71] energies as references. Double-z and triple-z basis sets were used for geometry optimization and energy refinement, respectively. Temperature and pressure and solvent modelling have been selected to match experimental conditions. A more detailed description of the method benchmark and the computational methods utilized is described in the Appendix chapter.

The results chapter is organized using a different structure than in the publications to eliminate redundancy and to maximize the comparisons between **Fe-PNP** and **Mo^{Cl}-PN^{H}P**. Many different reaction mechanisms have been explored, but only those with the lowest energy are described in the thesis (unless relevant exceptions). All presented energies are free energies (unless contrary stated). In the thesis, the superindexes F, D, M, MF and MA in the nomenclature of reaction intermediates have been used to denote the presence of formanilide, DMF, morpholidine, N-methylformanilide or N-methylacetanilide, respectively. The hydrogenated catalyst form **M^H-PN^{H}P** has been used as free energy reference (unless stated). Note that the labelling of species in the thesis does not follow the labelling used in the corresponding papers.

4.1 Reaction mechanisms of deaminative hydrogenation of amides

4.1.1 Hydrogen activation and catalyst inhibition

Molecular hydrogen is not sufficiently reactive to reduce amides or aldehyde C=O bonds. Therefore, hydrogen activation is needed before such reactions. When in presence of the Fe catalyst (^{iPr}PNP)Fe(H)(CO) (**Fe-1**), H_2 suffers a concerted heterolytic cleavage, yielding the trans-dihydride complex (^{iPr}PN^{H}P)Fe(H)$_2$(CO) (**Fe-2**) (see Figure 4.4). This hydrogenation is a -10.2 kcal mol^{-1} exergonic reaction with an internal energy barrier of 11.6 kcal mol^{-1} (**Fe-TS-1-2**). Alternatively, **Fe-1** hydrogenation can be assisted by a proton relay molecule such as methanol (studied by the groups of Wang and Guan)[88] or formanilide (studied in the thesis, see Figure 4.5). Wang and Guan reported an internal barrier of 17.3 kcal mol^{-1} for the methanol assisted **Fe-1** hydrogenation. In the thesis we researched the formanilide assisted mechanism, which proceeds through a H_2 binding to the metal centre while formanilide NH protonates the catalyst ligand, thus forming intermediate **Fe-3** at 6.8 kcal mol^{-1}. Then, H_2 is deprotonated by the formanilide N, yielding **Fe-2**. The formanilide-assisted activation of H_2 has an effective energy barrier of 4.0 kcal mol^{-1}, which is 3.1 and 7.6 kcal mol^{-1} less energetic than the methanol-assisted and the unassisted reactions.

However, hydrogen activation can be inhibited by weak acids such as formanilide or methanol (see Figure 4.4), which can react with **Fe-1**, forming the adducts **Fe-4^F** and **Fe-4^{MeOH}**, respectively. These adducts are not part of the catalytic cycle (off-cycle reactions). The stability of **Fe-4^F** (ΔG = -2.0 kcal mol^{-1}is consistent with its characterization by NMR and single-crystal X-ray diffraction analysis.[31] In the other hand, the less stable **Fe-4^{MeOH}** (ΔG = 3.3 kcal mol^{-1}) has only been characterized by NMR analysis at temperatures $\leq$ 20 ºC.[63,64] As a consequence of Fe catalyst inhibition by **Fe-4^F**, the catalyst activation mechanism has an effective energy barrier of 21.8 kcal mol^{-1}, or 16.2 kcal mol^{-1} in the presence of formanilide or 14.0 kcal mol^{-1} in the presence of methanol.
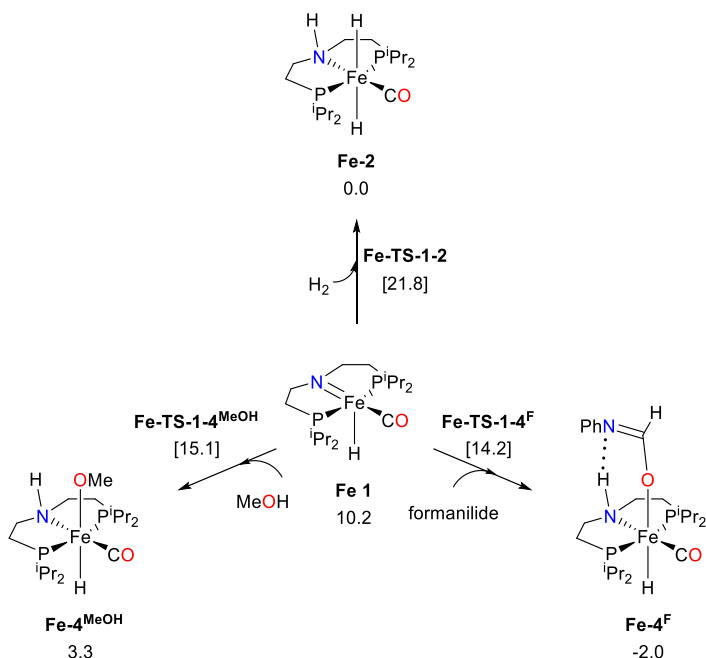
Figure 4.4 Free energies (kcal mol^{-1}) of unassisted **Fe-1** hydrogenation and **Fe-1** off-cycle species.
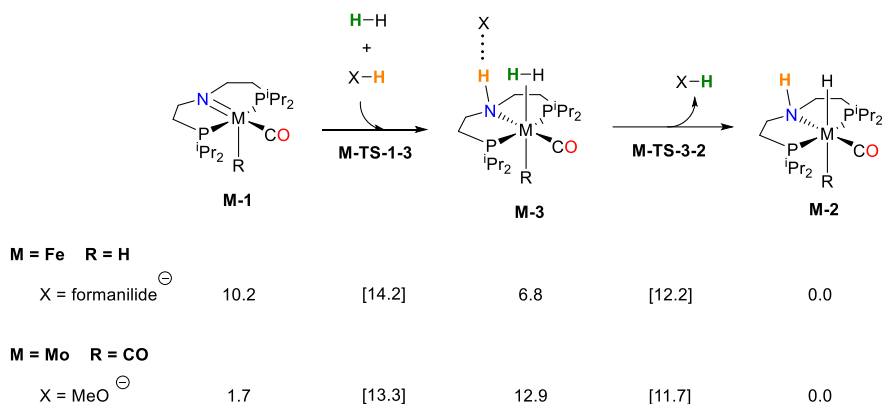
Figure 4.5 Free energies (kcal mol^{-1}) of catalyst hydrogenation assisted by formanilide and methanol.

On the case of Mo, the use of the catalyst precursor **Mo^{Cl}-PN^{H}P** requires stoichiometric amounts of NaBHEt$_3$ to generate the active [(^{iPr}PNP)Mo(CO)$_2$]Na (**Mo-1**) (see Figure 4.6), in which Mo(I) has been reduced to Mo(0).[54] The reduction of Mo(I) to Mo(0) is supported by the observation of hydrogen gas, and by HR-ESI mass spectrometry and EPR analysis of **Mo-1**.

Hydrogen activation with **Mo-1** follows the same mechanism than with **Fe-1** (see Figure 4.6), but on Mo case, the reaction is more thermoneutral (-1.7 *vs* -10.2 kcal mol^{-1}) and its internal barrier is higher (18.6 *vs* 11.6 kcal mol^{-1}). Furthermore, the Mo-methanol-assisted hydrogen activation has a higher internal barrier than that of the Fe-formanilide-assisted (11.6 kcal mol^{-1} *vs* 4.0 kcal mol^{-1}). In the other hand, the formations of adducts **Mo-4^F**, **Mo-4^{MeOH}** and **Mo-4^{EtOH}** (-20.8, -9.7 and -11.6 kcal mol^{-1}) are more exergonic than their Fe counterparts. The higher stability of **Mo-4** adducts might be attributed to a charge stabilization via the Na$^+$ counterion, the Lewis acid BEt$_3$ present in the solution (see Figure 4.5),

and the trans-CO ligand back-donation. As a consequence of Mo catalyst inhibition by **Mo-4^F**, **Mo-4^{MeOH}** and **Mo-4^{EtOH}**, hydrogen activation is not feasible without a proton relay molecule (effective barriers > 30 kcal mol^{-1}). Only the methanol assisted mechanism has a thermally accessible effective energy barrier (21.4 kcal mol^{-1}).
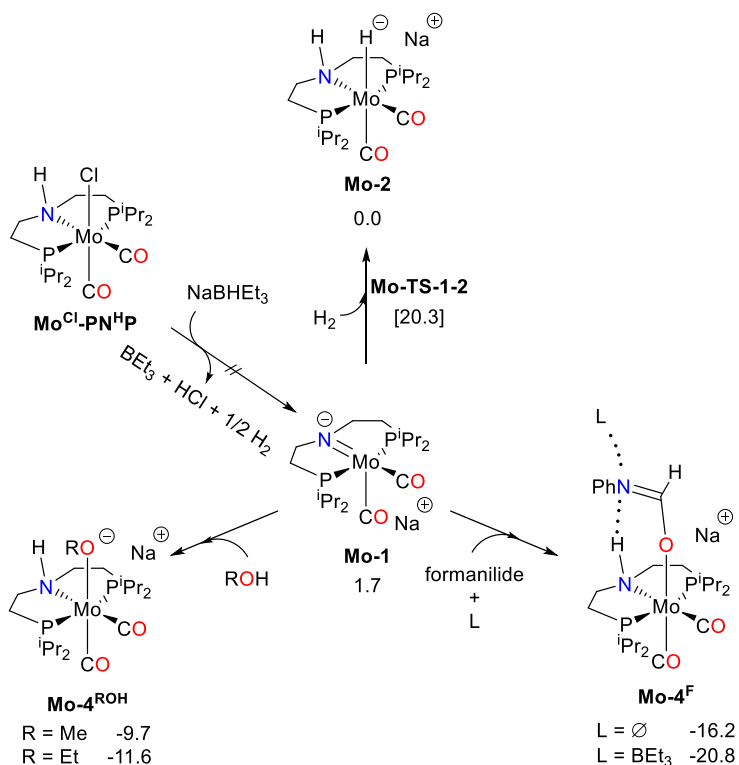
Figure 4.6 Free energies (kcal mol-1) of unassisted **Mo-1** hydrogenation and **Mo-1** off-cycle species.

4.1.2 **Amide and aldehyde C=O hydrogenation**

The hydrogenation of the amide C=O, as well as the hydrogenation of the aldehyde C=O, is performed by the hydrogenated catalyst species **Fe^H-PN^{H}P** or **Mo^H-PN^{H}P** (**Fe-2** or **Mo-2**) (see Figure 4.2). Our calculations indicate that both amide and aldehyde C=O hydrogenation by **Fe-2** or **Mo-2** share a common reaction mechanism (see Table 4.1): The mechanism is a stepwise process, consisting on an outer-sphere hydride transfer from the metal to the carbonyl C (**M-TS-2-5**), followed by a proton transfer from the ligand NH to the carbonyl O (**M-TS-5-1**). This proposal is consistent with other reported mechanistic studies on bifunctional pincer catalysts for (de)hydrogenation reactions.[11,14,92,93]

M	Reactant	M-2	M-TS-2-5	M-5	M-TS-5-1	M-1
	Formanilide	0.0	[15.8]	15.1	**[16.9]**	14.9
	Morpholidine	0.0	**[22.5]**	21.0	[19.7]	19.0
Fe	DMF	0.0	[23.1]	23.2	**[23.4]**	20.6
	Formaldehyde	0.0	**[4.6]**	-0.7	[-0.9]	-5.1
	Formanilide	0.0	**[10.6]**	5.4	[6.9]	5.7
	N-methylformanilide	0.0	**[13.1]**	6.6	[9.7]	9.3
Mo	N-methylacetanilide	0.0	**[20.9]**	12.6	[12.6]	12.2
	Formaldehyde	0.0	**[6.6]**	-9.1	[-9.8]	-13.6
	Acetaldehye	0.0	**[9.5]**	1.9	[0.5]	-6.4

Table 4.1 Free energies (kcal mol^{-1}) for amide and aldehyde C=O hydrogenation by **M^H-PN^{H}P** catalyst. The most energetic transition states are highlighted in green colour.

On the case of **Fe-2** assisted amide C=O hydrogenation, all the studied reductions are endergonic (from 15 to 20 kcal mol^{-1}), and all their

transition states are thermally accessible (below 24 kcal mol^{-1}). The energy difference between the hydride transfer (**Fe-TS-2-5**) and proton transfer barriers (**Fe-TS-5-1**) is small: (between -1 and 3 kcal mol^{-1}). Therefore, it is difficult to predict whether the hydride or the proton transfer will be the most energetic transition state of amide C=O hydrogenation by **Fe-2**. In the case of formaldehyde C=O hydrogenation, the reduction is exergonic (-5.1 kcal mol^{-1}) and the hydride transfer is significantly more energetic than the proton transfer (4.6 kcal mol^{-1} *vs* -0.9 kcal mol-1). The energies associated with formaldehyde reduction are significantly smaller than those of amides as a consequence of formaldehyde C=O lower electron density.

Regarding **Mo-2** assisted amide C=O hydrogenation, all the reductions are endergonic too, and their transition states are also thermally accessible. However, hydrogenation barriers with Mo are significantly lower than Fe barriers (around 10 kcal mol^{-1} higher). Moreover, contrary to Fe, Mo hydride transfers (**Mo-TS-2-5**) are consistently higher than Mo proton transfers (**Mo-TS-5-1**). Within the studied amides, acetanilide hydride transfer barrier is significantly higher than those of formamides (20.9 *vs* 10.6 and 13.1 kcal mol^{-1}), as a consequence of acetanilide C=O higher electron density. In Chapter 4.2 we will see that this energy difference is one of the reasons for **Mo^{Cl}-PN^{H}P** selectivity towards formamides. On the case of aldehydes, **Mo-2** assisted formaldehyde and acetaldehyde C=O hydrogenations follow the same trends as the **Fe-2** assisted: they are exergonic, their most energetic

transition state is the hydride transfer, and their transition states are lower than those of amide C=O hydrogenation.

4.1.3 **Hemiaminal C-N bond protonolysis**

The hemiaminal C-N bond protonolysis involves the following chemical transformations: hemiaminal OH deprotonation, hemiaminal N protonation and C-N cleavage (Figure 4.7). The simplest reaction mechanism, the intramolecular O-to-N proton transfer followed by C-N cleavage, has prohibitively high energy barriers for any of the tested amides (> 45 kcal mol^{-1}). Therefore, proton relay molecules are needed, as already proposed in the literature.[49,88] The candidates to assist the proton transfer are many: the catalyst, secondary amides (substrate), hydrogen (reactant) and alcohols (products). For these reasons, C-N bond protonolysis can proceed through different paths. However, only three paths have been identified to be the most relevant. They differ on which are the assisting molecules and on the order of the reaction steps (Figure 4.7).

Path 1 is catalyzed only by the catalyst (**M-1**). It consists of first the hemiaminal OH deprotonation by the ligand N (**M-TS-1-7**). Then the hemiaminal C-N cleavage (**M-TS-7-8**) forms an amido complex **M-8** and releases an aldehyde molecule, which can rapidly be reduced to alcohol. Finally, **M-8** amido group is protonated by the ligand NH (**M-TS-8-1**), yielding the corresponding amine.

Path 2 is catalyzed by both **M-1** and a proton relay molecule. It consists of first the hemiaminal OH deprotonation by the ligand N (**M-TS-1-9**) and the coordination of the proton relay to the metal centre. Then, the proton relay protonates the hemiaminal N (**M-TS-9-10**), thus liberating the corresponding zwitterion. Finally, the zwitterion will then undergo C-N cleavage (**M-TS-10-4**) and liberate the corresponding amine and aldehyde.

Path 3 is catalyzed by a proton relay molecule only, and the order of the steps depends on the acidity/basicity of the proton relay molecule. **Path 3** with formanilide as proton relay presents first the hemiaminal N protonation (**TS-6-11**), followed by the hemiaminal OH deprotonation (**TS-11-12**), forming a zwitterion that will then undergo C-N cleavage (**TS-12-13**). In the other hand, **Path 3** with methanol as proton relay, presents first a concerted hemiaminal protonation/deprotonation (**TS-6-12**) to a zwitterion, that will then undergo C-N cleavage (**TS-12-13**) to the corresponding aldehyde and amine.

Hemiaminal C-N protonolisis

M = Fe or Mo
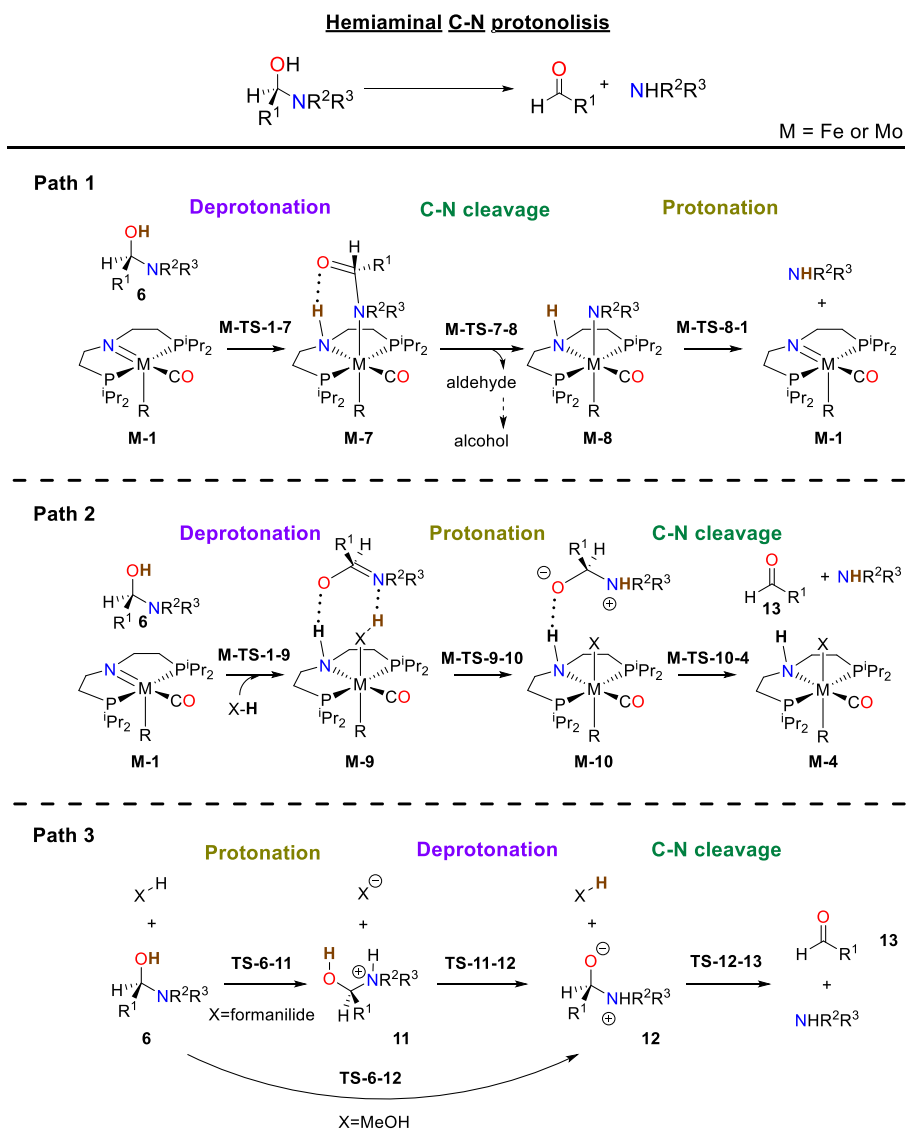
Figure 4.7 Calculated key steps of hemiaminal C-N bond protonolysis when in the presence of an **M-PNP** catalyst.

When in the presence of **Fe-1**, formanilide hemiaminal C-N bond protonolysis is assisted solely by **Fe-1** (**Path 1** in Figure 4.8). This path is almost thermoneutral, $\Delta G = 0.1$ kcal mol^{-1}, due to the exergonic (and

fast) reduction of formaldehyde to methanol. Its highest energy barrier **Fe-TS-7-8^F** ($\Delta G^{\ddagger}$ = 24.9 kcal mol^{-1}) is associated with the C-N bond cleavage step.
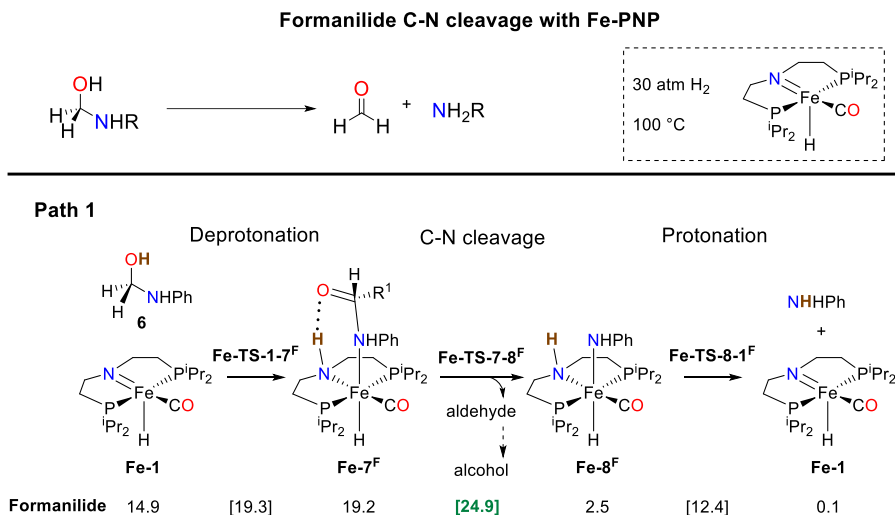
Figure 4.8 Calculated key steps of hemiaminal C-N bond protonolysis of formanilide when in **Fe-1** catalysis experimental conditions.[31,51] In green, most energetic species.

On the other case, morpholidine and DMF hemiaminal C-N protonolysis prefer **Path 2** and **Path 3** (see Figure 4.9) over **Path 1**, which is disfavoured by morpholidine and DMF more electron-donor substituents (ΔG > 40 kcal mol^{-1}). For both amides, the highest energy barrier is the proton transfer, but the methanol-assisted **Path 3** (ΔG = 28.1 and 29.6 kcal mol^{-1}) is slightly less energetic than **Path 2** (ΔG = 31.4 and 30.4 kcal mol^{-1}). However, **Path 3** precise of methanol, which can only be previously produced through **Path 2**. Therefore, one can expect that the reaction will evolve through **Path 2** during the first minutes, and will gradually switch to **Path 3** as methanol concentration increases. **Path 2** becomes unnecessary when formanilide is used as co-

catalyst: In this case, morpholidine and DMF hemiaminal C-N protonolysis proceeds only through the less energetic formanilide-assisted **Path 3** (highest energy barriers of 23.4 and 23.8 kcal mol^{-1}).
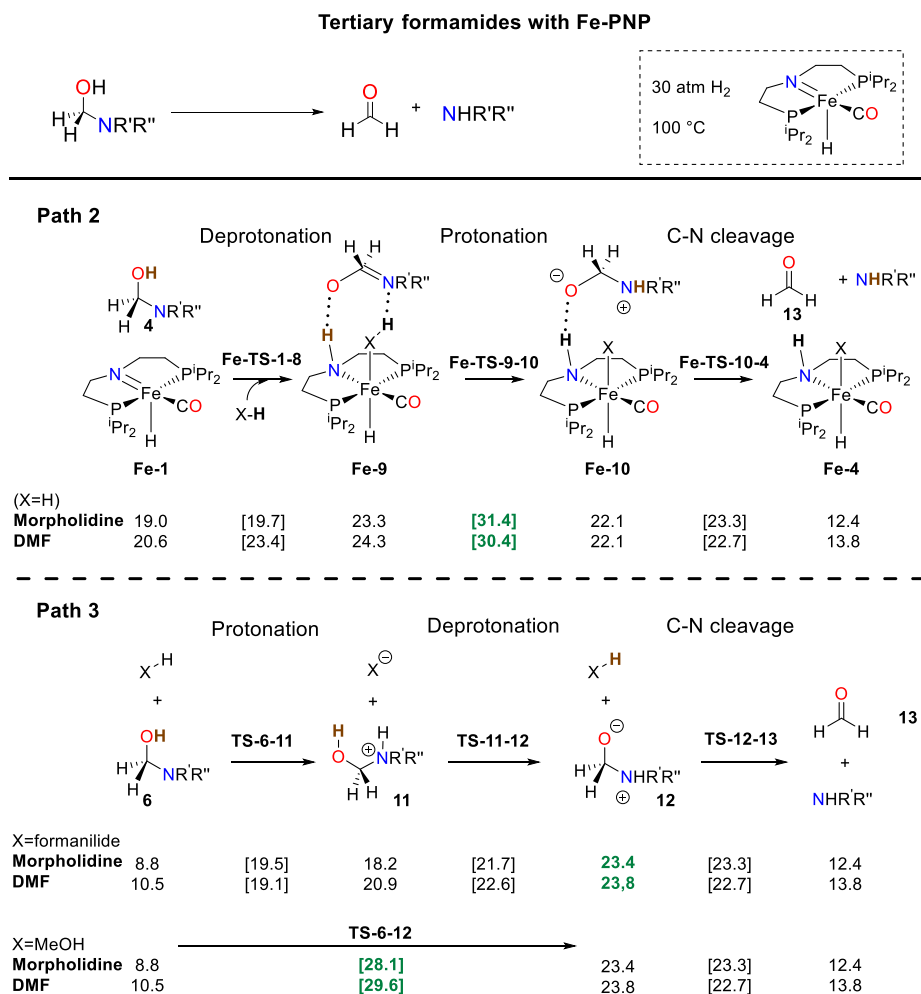
Figure 4.9 Calculated key steps of hemiaminal C-N bond protonolysis of DMF and morpholidine when in **Fe-1** catalysis experimental conditions.[31,51] In green, most energetic species.

Briefly, formanilide, morpholidine and DMF highest energy barriers for the hemiaminal C-N protonolysis are 24.9, 28.1 and 29.6 kcal mol^{-1} when unassisted, and 24.9, 23.4 and 23.8 kcal mol^{-1} when formanilide-assisted. In Chapter 4.2 we will see that these energy barriers are one of the rate-limiting factors in the **Fe-PNP**-catalyzed deaminative hydrogenation of amides.

The reaction pathways for the hemiaminal C-N protonolysis when in the presence of **Mo-1** are shown in Figure 4.10. Formanilide, N-methylformanilide and N-methylacetanilide go through both **Path 1** and the methanol-assisted **Path 2**. The most energetic species of the methanol-assisted **Path 2** (ΔG = 12.4, 10.8 and 11.2 kcal mol^{-1}) are less energetic than those of **Path 1** (ΔG = 12.5, 22.9 and 23.2 kcal mol^{-1}). However, **Path 2** precise of methanol, which can only be previously produced through **Path 1**. Therefore, one can expect that the reaction will evolve through **Path 1** during the first minutes, and will gradually switch to **Path 2** as methanol concentration increases. This situation resembles the cases of Morpholidine and DMF hemiaminal protonolysis when in the presence of **Fe-PNP**, where the methanol assisted paths were preferred over the other mechanisms. Remarkably, transition state **Mo-TS-7-8** with formanilide (12.5 kcal mol^{-1}) is substantially less energetic than with N-methylformanilide, N-methylacetanilide or its Fe analogue **Fe-TS-7-8** (22.9, 23.2 and 24.9 kcal mol^{-1} respectively). On the cases of N-methylformanilide and N-methylacetanilide, this is because of their more electron-rich C-N bond due to the electron-donating nature of the N methyl.

Hemiaminal C-N protonolysis with Mo-PNP

Path 1

Formanilide						
5.7	[6.0]	6.3	**[12.5]**	-9.5	[4.1]	-8.4
N-methylformanilide						
9.3	[15.6]	17.9	**[22.9]**	2.6	[3.0]	-6.8
N-methylacetanilide						
12.2	[14.9]	19.8	**[23.2]**	3.6	[4.0]	-3.2

Path 2

(X=MeO)

Formanilide						
-5.7		TS-4-10 [11.2]		**12.4**	[11.7]	-4.6
N-methylformanilide						
-2.2	[4.7]	5.1	[9.4]	**10.8**	[10.3]	-2.9
N-methylacetanilide						
-1.1	[6.6]	5.9		TS-9-4 **[11.2]**		-9.1
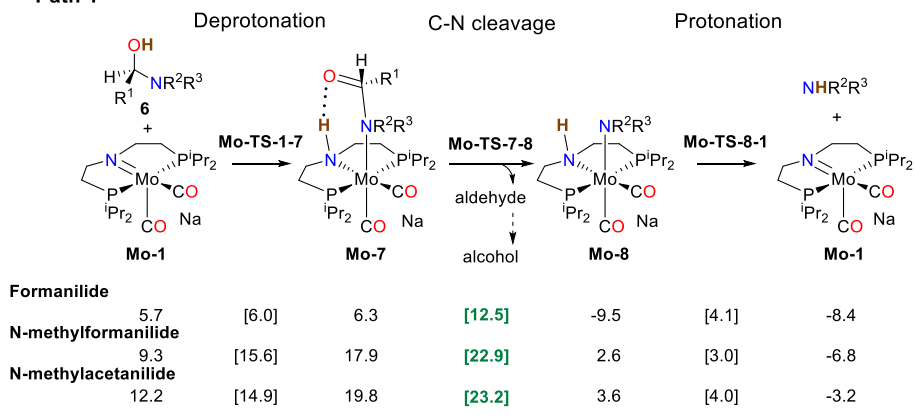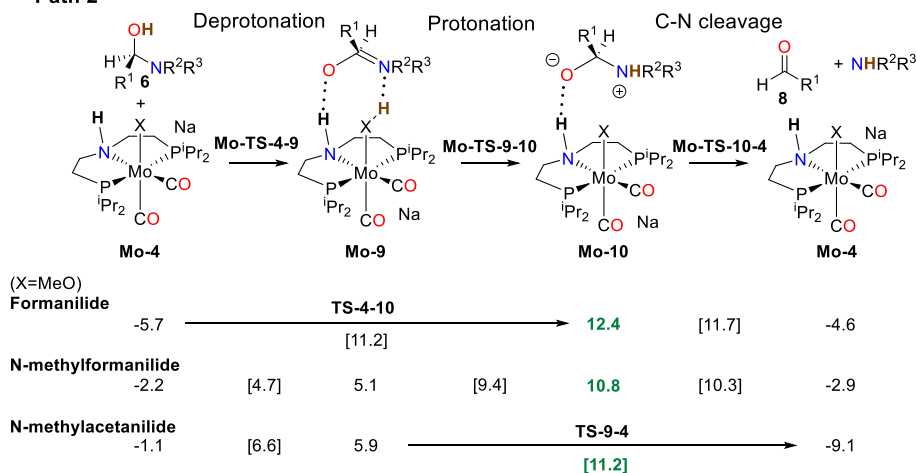
Figure 4.10 Calculated key steps of hemiaminal C-N bond protonolysis when in **Mo-1** catalysis experimental conditions.[31,51] In green, most energetic species.

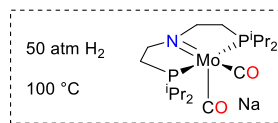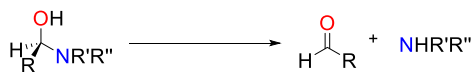# 4.2 Comparison between experimental and computational results.

Fe-PNP-catalyzed deaminative hydrogenation of amides

The species with the highest and the lowest energies in the reaction mechanisms of the Fe-catalyzed deaminative hydrogenation of amides are shown in Figure 4.11. The rate-limiting step for formanilide is the hemiaminal C-N cleavage (**Fe-TS-7-8^F** with 24.9 kcal mol^{-1}), whereas for morpholidine and DMF, is the hemiaminal proton transfer assisted by methanol (**TS-6-12^M** and **TS-6-12^D** with 28.1 and 29.6 kcal mol^{-1}) (see Figure 4.11). In the other hand, morpholidine and DMF share the same resting state, **Fe-2** with 0.0 kcal mol^{-1}, but not formanilide, which inhibits the catalyst with the formation of **Fe-4^F** with -2.0 kcal mol^{-1}. The formation of the methanol adduct **Fe-4^{MeOH}** is slightly endergonic (ΔG = 3.3 kcal mol^{-1}) but it could also play a role as inhibitor at large concentration of methanol and low temperatures.[63,64] Therefore, the effective energy barriers of formanilide, morpholidine and DMF hydrogenation are 26.9, 28.1 and 29.6 kcal mol^{-1} respectively, which are in qualitatively agreement with their experimental conversions of 58%, 36% and 0%.

Key species of Fe-PNP-catalyzed amide deaminative hydrogenation
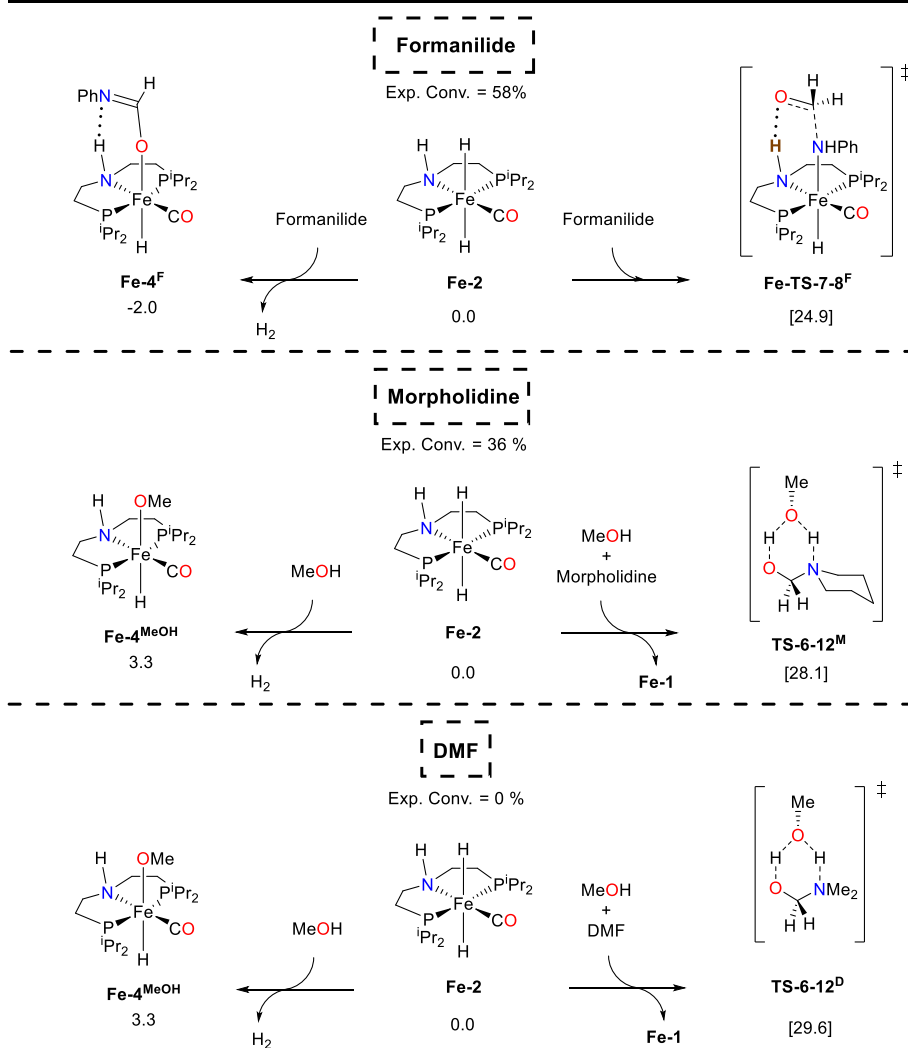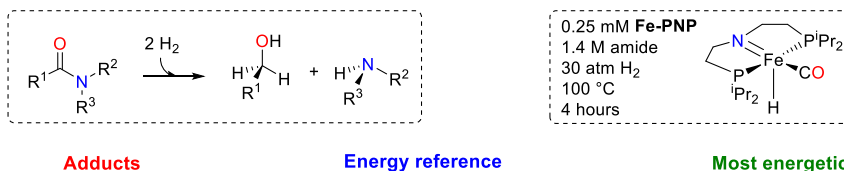
Figure 4.11 Catalyst adducts and most energetic species, in the reaction mechanisms of formanilide, DMF and morpholidine deaminative hydrogenation, when catalyzed by **Fe-PNP**.

Nevertheless, when formanilide is used as co-catalyst, the resting state and the TS with the highest energy change (see Figure 4.12). In this case, the species with the largest energy are the zwitterions 12^M and 12^D for morpholidine and DMF respectively, with energies of 23.4 and 23.8 kcal mol^{-1}. The adduct **Fe-4^F** becomes the least energetic species, at -2.0 kcal mol^{-1}. The effective barriers for morpholidine and DMF are 25.4 and 25.8 kcal mol^{-1} respectively, which qualitatively match their experimental conversions of >99% and 14%. The low conversion of DMF when compared to morpholidine, can be attributed to the global thermodynamic energy of the DMF reaction, which is close to thermoneutrality (ΔG = -1.5 kcal mol^{-1}, see Figure 4.3) and limits the conversion of DMF to a maximum of 32%.

The use of experimental data to validate and evaluate the precision of our computed mechanisms is not straightforward because of several factors: the multiple roles of formanilide in the reaction (as substrate, co-catalyst and inhibitor), thermoneutrality of the DMF hydrogenation reaction, the difficulty to estimate the real concentration of solved hydrogen, and the large difference in concentration of amide, hydrogen and catalysts in solution. Consequently, microkinetic models were constructed using the computed free energy barriers for the **Fe-PNP**-catalyzed formanilide and DMF deaminative hydrogenation (see Paper I for detailed information about their construction).[51]

Key species of Fe^H-PN^{H}P-catalyzed amide deaminative hydrogenation
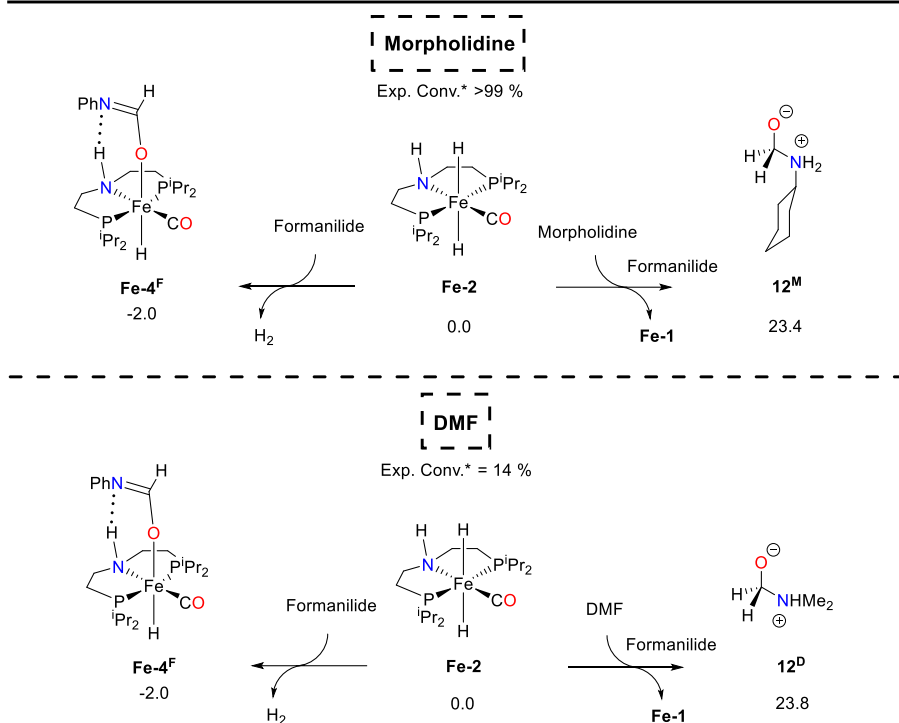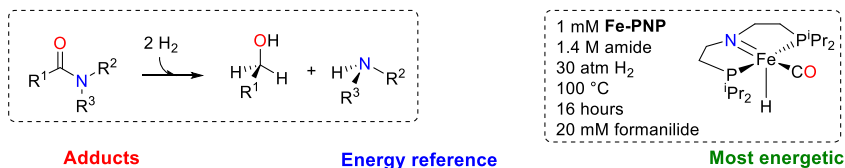
Figure 4.12 Catalyst adducts and most energetic species, in the reaction mechanisms of DMF and morpholidine deaminative hydrogenation when catalyzed by **Fe-PNP** and co-catalyzed by formanilide. * Experimental conversion at 60 atm H_2 and 120 ºC.

The microkinetic model for the hydrogenation of formanilide predicted a low conversion of 1 % (see Graph 4.1). Such calculated conversion diverges from the experimental formanilide conversion of 58%. The microkinetic model reproduced the experimental results after adding small corrections in the free energies of **Fe-TS-7-8^F** and **Fe-4^F** ($\Delta\Delta G =$ -2.9 and 2.5 kcal mol^{-1}, respectively), which are the stationary points with the highest and lowest energy in the overall reaction profile.

In the other hand, the DMF microkinetic model predicted a DMF conversion of 0 %. Such calculated conversion matched the experimental DMF conversion. However, when 20 eq. of formanilide were added in the microkinetic model (as co-catalyst), the calculated 31 % conversion did not match the experimental 14 % conversion (see Graph 4.2). Incorporation of the corrections done in the formanilide microkinetic model ($\Delta\Delta G =$ -2.9 and 2.5 kcal mol^{-1} to **Fe-TS-7-8^F** and **Fe-4^F**) considerably improved DMF predicted conversion to 15 %.

In conclusion, the mechanism inferred from the DFT calculations accounts for the experimental observations, since the energy deviations derived from the fit are within the error range expected for calculated Gibbs energies,[95,96] the approach used to calculate the concentration of solved hydrogen, and the standard deviation in experimental measurements.
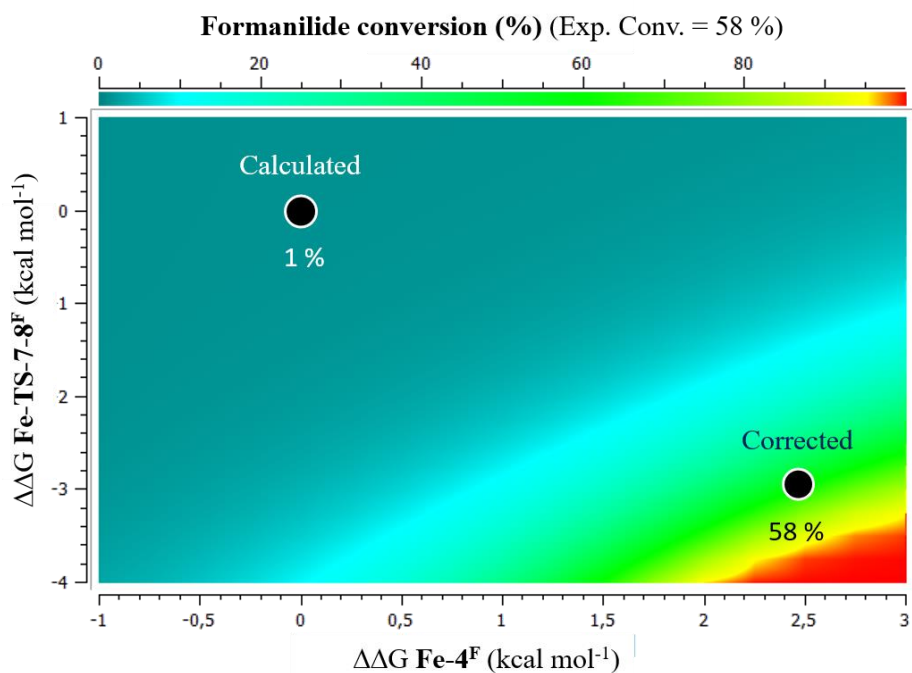
Graph 4.1 Microkinetic simulations of the formanilide deaminative hydrogenation. Formanilide conversion at 4 hours (%) vs ΔΔG **Fe-TS 7-8^F** vs ΔΔG **Fe-4^F** (kcal mol^{-1}). The simulations were based on the reaction mechanisms shown in Figure 4.4, Figure 4.5, Figure 4.8 and Table 4.1. The initial conditions are set up according to the experiments:[31] 1.4 M of formanilide, 0.162 M of H$_2$ [94] and 0.25 mM of **Fe^H-PN^{H}P**. H$_2$ concentration was kept constant throughout the kinetic simulations, consistent with the effectively constant pressure of H$_2$ used in the experiments.

DMF conversion (%) (Exp. conv. 14 %)
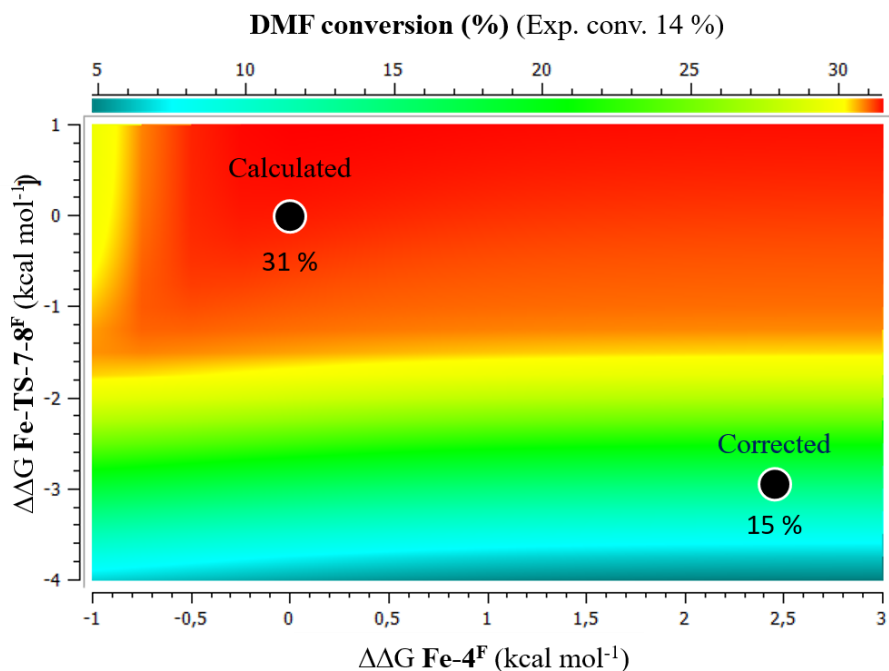
Graph 4.2 Microkinetic simulations of the DMF deaminative hydrogenation. DMF conversion at 16 hours (%) vs ΔΔG **Fe-TS-7-8^F** vs ΔΔG **Fe-4^F** (kcal mol^{-1}). The simulations were based on the reaction mechanisms shown in Figure 4.4Figure 4.5, Figure 4.8 and Figure 4.9 and Table 4.1. The initial conditions are set up according to the experiments:[31] 1.4 M of formanilide, 0.162 M of H$_2$ [94] 1 mM of **Fe^H-PN^{H}P** and 20mM of formanilide. H$_2$ concentration was kept constant throughout the kinetic simulations, consistent with the effectively constant pressure of H$_2$ used in the experiments.

Mo-PNP-catalyzed deaminative hydrogenation of amides

The most and least energetic species of the reaction mechanism of the **Mo-PNP**-catalyzed deaminative hydrogenation of amides are summarized in Figure 4.13. Using **Mo-2** as energy reference, both the **M-4** adducts and the most energetic species in the molybdenum-catalyzed reaction are more stable than those of the iron-catalyzed reaction (> 10 kcal mol^{-1} and > 3 kcal mol^{-1} respectively). Two species regulate the reaction rates of formanilide, and N-methylformanilide hydrogenation, due to their similar energies: species **Mo-TS-1-3** and **Mo-10^F** in the case of formanilide ($\Delta G = 13.3$ and 12.4 kcal mol^{-1}), and species **Mo-TS-1-3** and **Mo-TS-2-5^{MF}** in the case of methylformanilide ($\Delta G = 13.3$ and 13.1 kcal mol^{-1}). Species **Mo-TS-2-5MA** ($\Delta G = 20.9$ kcal mol^{-1}) is the rate limiting step of N-methylacetanilide hydrogenation by **Mo-PNP**.

The effective barriers of formanilide, N-methylformanilide and N-methylacetanilide (33.2, 22.8 and 32.5 kcal mol^{-1}) qualitatively match their experimental conversions (13 %, >99 % and 20 %). Remarkably, N-methylacetanilide has a non-zero conversion despite its prohibitively high 32.5 kcal mol^{-1} effective barrier: N-methylacetanilide reacts only at the beginning of the reaction, when the low concentration of ethanol makes the contribution of the species **Mo-4^{EtOH}** irrelevant, thus resulting in an initial effective barrier of 20.9 kcal mol^{-1}. Unfortunately, the non-zero conversion of formanilide cannot be explain by the proposed mechanism.

Key species of Mo^H-PN^{H}P-catalyzed amide deaminative hydrogenation
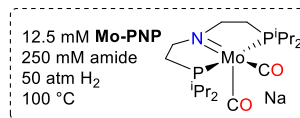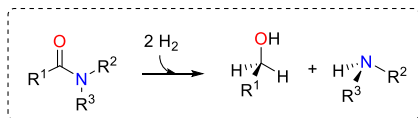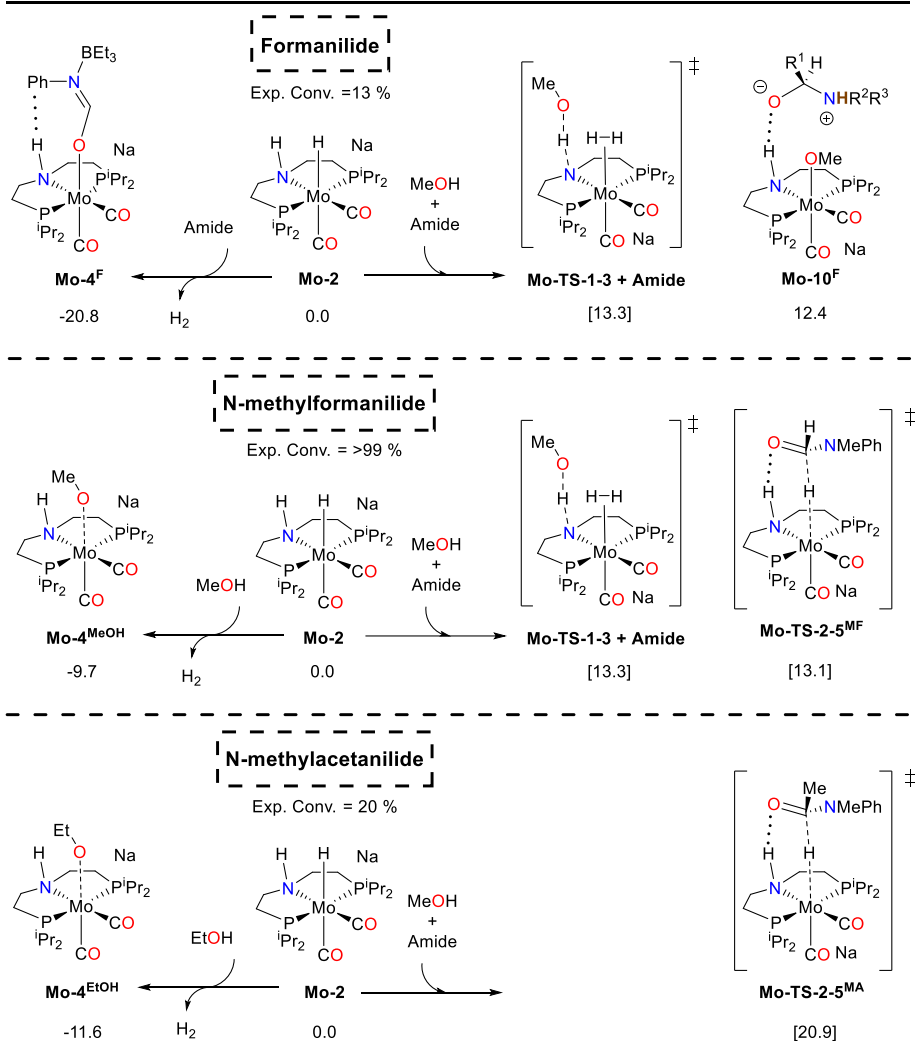
Figure 4.13 Catalyst adducts and most energetic species, in the reaction mechanisms of formanilide, N-methylformanilide and N-methylacetanilide deaminative hydrogenation, when catalyzed by **Mo^H-PN^{H}P**.

As in the case of Fe, microkinetic modelling was used to compare the calculated energies with the experimental conversions. In this case we simulated the hydrogenation of N-methylformanilide, and we studied the inhibiting effect of ethanol over this reaction (see Paper III for detailed information about its construction).[54] The microkinetic model predicted a considerable dependence of amide conversion on ethanol concentration: >99 %, 99 % and 55 % conversion in the presence of 0, 0.5 and 2 eq. of ethanol (straight-lines in Figure 4.14). The calculated conversions qualitatively matched the experimental conversions of >99%, 96 % and 35 % respectively. The microkinetic model was able to reproduce the experimental values after small corrections in the most and least energetic species ($\Delta\Delta G$ = +0.3, +0.4, -1.8 and +0.2 kcal mol^{-1} to **Mo-TS-2-5^{MF}**, **Mo-TS-1-3**, **Mo-4^{MeOH}** and **Mo-4^{EtOH}**) (dashed lines in Figure 4.14). An alternative source of error is the catalyst activation mechanism, which fitted the experimental conversions when introduced as a single irreversible reaction with a 25 kcal mol-1 barrier.
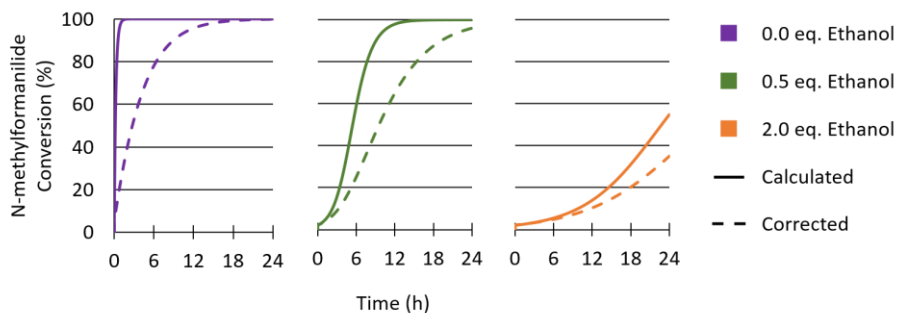
Figure 4.14 Fitted and unfitted microkinetic models of the **Mo^Cl-PN^HP** catalyzed N-methylformanilide deaminative hydrogenation when in the presence of 0, 0.5 and 2.0 eq. of ethanol. The simulations were based on the reaction mechanisms shown in Figure 4.5, Figure 4.6 and Figure 4.10 and Table 4.1 The initial conditions for the microkinetic model are set up according to the experiments:[54] 0.25 M of N-methylformanilide, 0.207 M of H_2,[94] 12.5mM of **Mo^Cl-PN^HP**. H_2 concentration was kept constant throughout the kinetic simulations, consistent with the effectively constant pressure of H_2 used in the experiments.

4.3 Reaction optimization.

Fe-PNP - catalyzed deaminative hydrogenation of amides

A rational approach involving DFT calculations has been used to design co-catalysts tailored for the deaminative hydrogenation of tertiary amides (*Paper II*).[53] This was possible thanks to the research on **Fe-PNP** catalyzed deaminative amide hydrogenation (*Paper I*),[51] which identified the role of the co-catalyst: proton shuttle for the formation of zwitterion **12**, here named $[\Delta G_{HT}]^{\ddagger}$ (see Figure 4.15). However, formanilide, the co-catalyst studied in *Paper I*, had the drawbacks of being parallelly hydrogenated by **Fe-2** on the course of the reaction and inhibiting the catalyst by the formation of adducts **Fe-4^F**, here named ΔG_{add} (see Figure 4.15).

In *Paper II*, I calculated the ΔG_{add} and $[\Delta G_{HT}]^{\ddagger}$ of a series of potential organic co-catalysts that could act as a proton shuttle for hemiaminal proton transfer (low $[\Delta G_{HT}]^{\ddagger}$), without inhibiting the catalyst (**Fe-4** > **Fe-2**), or being hydrogenated by **Fe-2**.
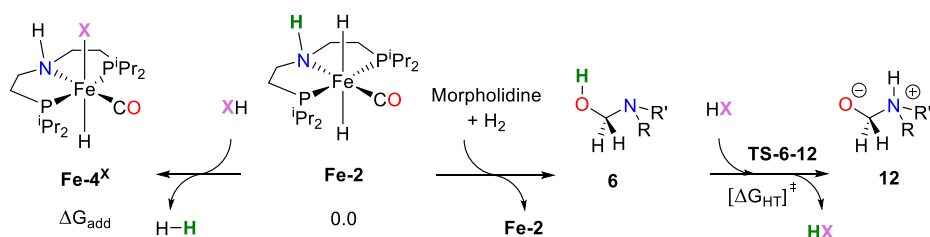
Figure 4.15 Key energies and species of tertiary alkyl amides deaminative hydrogenation when catalyzed by **Fe-1**.

The potential catalysts assessed (see Table 4.2) included molecules with either hydrogen-bond donor single-sites (entries 4, 5 and 8) or with both hydrogen-bond donor and acceptor sites which could act as push-pull proton shuttles (entries 1-3, 6 and 9). In molecules with C=O or C=N functional groups, only electron-rich systems were chosen to minimize the hydrogenation of the co-catalyst.

The calculated $[\Delta G_{HT}]^{\ddagger}$ and ΔG_{add} of morpholidine deaminative hydrogenation were used to estimate the effective energy barrier of the reaction: $\Delta G_{eff} = ([\Delta G_{HT}]^{\ddagger} - \Delta G_{add})$ except when $\Delta G_{add} > $ **Fe-2** and/or **TS-6-12^{MeOH}** $< [\Delta G_{HT}]^{\ddagger} < $ **12^{M}**, in which cases **Fe-2**, **TS-6-12^{MeOH}** or **12^{M}** substituted $[\Delta G_{HT}]^{\ddagger}$ and ΔG_{add}. The ΔG_{eff} of each potential co-catalyst was then compared to its corresponding experimental performance (see Table 4.2)

ΔG_{eff} qualitatively correlated to experimental TONs, with the exception of 1,2,3-triphenyl guanidine (entry 6), which may react differently as indicated by an immediate colour change upon treatment with **Fe-PNP**. Triazabicyclodecene (TBD, entry 1) and acetanilide (entry 2) experimentally proved to be co-catalysts more active than formanilide, being TBD the best performing co-catalyst among the tested, improving formanilide co-catalyst activity by a 130%.

Reaction scheme: formylmorpholine (1.4 M) + H$_2$ (30 atm) → [0.07 mol% **Fe-PNP**, 1.75 mol% [Co-cat], THF, 2h, 100 °C] → CH$_3$OH (methanol) + morpholine (HN–O)

Entry	Co-catalyst	[ΔG$_{HT}$]‡	ΔG$_{add}$	ΔG$_{eff}$	TON^a	Conv.^{a}
1	TBD (triazabicyclodecene)	22.1	8.7	23.4	830	59%
2	N-phenylacetamide (Me-C(O)-N(H)-Ph)	25.4	1.9	25.4	780	55%
3	N-phenylformamide (H-C(O)-N(H)-Ph)	21.7	-2.0	25.4	630	45%*
4	2,6-di-tert-butyl-4-methylphenol (BHT)	25.5	14.6	25.5	560	40%
5	Me—OH (methanol)	28.1	3.3	28.1	510	37%
6	triphenylguanidine	21.4	1.4	23.4	440	31%†
7	No additive	28.1	---	28.1	320	22%
8	morpholine (O-NH)	31.9	18.2	28.1	320	22%
9	urea (H$_2$N-C(O)-NH$_2$)	35.6	1.4	28.1	90	6%*

Table 4.2 Computational and experimental results on potential co-catalysts for morpholidine deaminative hydrogenation, **Fe-PNP** catalyzed. * co-catalyst is consumed in the course of the reaction. † Immediate colour change was observed upon treatment with **Fe-PNP**. ^{a} Experimental reaction conditions: 30 atm H$_2$, 5 μmol of [**Fe-PNP**] (0.07 mol%), 1.75 mol% of each additive and 7 mmol of morpholidine in 5 mL of THF at 100 °C for 2 h. TON and Conv. were determined by GC-FID analysis of the products and remaining starting material. Each entry is the average of two or more trials.

TBD was later proved to significantly enhance the hydrogenation of other inactive amides (when **Fe-PNP**-catalyzed) (see Table 4.3), and the hydrogenation of morpholidine when catalyzed by **Ru^{HBH3}-PN^{H}P** or **Ru^{HBH3}-PN^{H}N** (see Table 4.4). TBD could not co-catalyze N-phenylbenzamide deaminative hydrogenation, though acetanilide did (Table 4.3; entry 4c).

Entry	Amide	[TBD]	TON[b].
1		0	50
		1.75	300
2		0	1150
		0.45	5180
3		0	140
		1.75	230
4		0	120
		1.75	120
		1.75[c]	250[c]

Table 4.3 [a] Reaction conditions: 60 atm H2, 5 μmol of [Fe-PNP] (0.07 mol%), x μmol of TBD, and 7 mmol of substrate in 5 mL of THF at 120 ℃ for 16 h. [b] TON was determined by GC-FID and NMR analysis of the products and remaining starting material. Each entry is the average of three or more trials. [c] TBD was substituted by N-acetanilide (Table 4.2; entry 2).

Entry	Catalyst	Co-catalyst	TON[b]	Conv.[b]
1	**Fe-PNP**	None	320	23%
		TBD	830	59%
		Formanilide	630	45%
2	**Ru^{HBH_3}-PN^{H}P**	None	310	22%
		TBD	1200	86%
		Formanilide	0[c]	0%[c]
3	**Ru^{HBH_3}-PN^{H}N**	None	440	31%
		TBD	1170	84%
		Formanilide	1040	74%

Table 4.4 [a] Experimental reaction conditions: 30 atm H_2, 5 µmol of [Fe or Ru] (0.07 mol%), 125 µmol co-catalyst and 7 mmol of morpholidine in 5 mL of THF at 100 ºC for 2 h. For [Ru] co-catalysts 10 µmol of NEt_3 was added to activate the catalyst. [b] Determined by GC-FID analysis of the products and remaining starting material. Each entry is the average of two or more trials. [c] Formanilide reacts irreversibly with this Ru catalyst to form an adduct (see *Paper II* for details).

Mo^{Cl}-PN^{H}P - catalyzed deaminative amide hydrogenation

In a similar fashion to the case of **Fe-PNP**, I attempted to optimize the **Mo^{Cl}-PN^{H}P**-catalyzed amide hydrogenation with the information obtained in its mechanistic study. Mo reaction mechanism shows a clear dependence on the counter-cation type (see Table 4.5) and location (see *Paper III* S.I.):[54] the energy difference between transition state **Mo-TS-2-5^{MF}** (rate-limiting step) and adduct **Mo-4^{MeOH}** (catalyst resting state) swings from 28.8 kcal mol^{-1} to 22.9 and 23.0 kcal mol^{-1} with the alkaline counterions Li$^+$, Na$^+$ and K$^+$, respectively. The extreme case of counterion absence shows an even lower effective energy barrier (ΔG_{eff} = 19.9 kcal mol^{-1}). These calculations were later tested experimentally: **Mo^{Cl}-PN^{H}P** was activated with LiHBH$_3$, NaHBH$_3$ or KHBH$_3$, and then used to hydrogenate N-methylformanilide at 80 °C and 50 atm of H$_2$. The resulting experimental conversions qualitatively agreed with their respective calculated effective energy barriers (see Table 4.5). Unfortunately, none of the tested counter-cations resulted in an improved reaction performance. To approach the limit of counter-cation absence, the sterically hindered counter-cation PPh$_4$$^+$ or the Na$^+$-trap crown ether 15-crown-5 were tested experimentally. However, they decreased the reaction yield, contrary to the computational predictions. This unexpected behaviour may be attributed to the probably low solubility of the ion pairs **[Mo^H-PN^{H}P]$^-$//PPh4$^+$** and **[Mo^H-PN^{H}P]$^-$//15-crown-5-Na$^+$**.

Table 4.5 Free energies (kcal mol^{-1}) for the isodesmic reaction between **Mo-4^{MeOH}** and **Mo-TS-2-5^{F}**. *Yields of **Mo^{Cl}-PN^{H}P**-catalyzed N-methylformanilide deaminative hydrogenation after 24h at 80 ºC with 5 mol% of alkali metal hydrides, 0.25 M of N-methylformanilide, 50 atm of H$_2$, 12.5mM of **Mo^{Cl}-PN^{H}P**
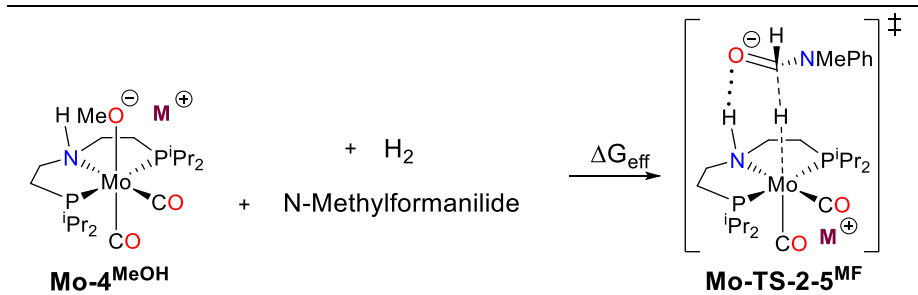
Counter-cation (M)	ΔG$_{eff}$ (kcal mol^{-1})	Yield (%)*
Li$^+$	28.8	9
Na$^+$	22.9	75
K$^+$	23.0	75
Absence of counter-cation	19.9	

5   **Conclusions and Future Outlook**

The main conclusions of the computational mechanistic study on the **Fe-PNP** catalyzed deaminative hydrogenation of amides were the following:

- Reliable energies and molecular geometries of amides and **Fe-PNP** complexes can be obtained with the use of the M06 functional and double-z basis sets, together with energy refinements with functional M06 and triple-z basis set.

- Deaminative hydrogenation of amides by **Fe-PNP** follows a three-step process consisting of (1) amide C=O hydrogenation, (2) C-N bond protonolysis, and (3) aldehyde C=O hydrogenation. The rate-limiting step of both secondary and tertiary amides is the C-N bond protonolysis, which proceeds by a different pathway for the two substrates. While **Fe-PNP** promotes the cleavage of the C-N bond of secondary amides, the C-N bond of tertiary amides is too electron-rich to be broken by **Fe-PNP**. In the latter case, secondary amides can act as proton-shuttles, and thus assist the C-N bond protonolysis.

- Catalyst **Fe-PNP** can dehydrogenate weak acids such as secondary amides or methanol, which can block the catalyst active-site and prevent its hydrogenation. This reaction is reversible but significant enough to hamper the catalyst activity.

- TBD has proved to co-catalyze the deaminative hydrogenation of tertiary amides thanks to (I) its proton-shuttle abilities, that facilitate the cleavage of tertiary amides C-N bonds, (II) its steric hindrance, that avoid TBD from blocking **Fe-PNP** active site, and (III) its difficult hydrogenation by **Fe-PNP**.

Particular conclusions of the computational mechanistic study on the **Mo^H-PN^HP** catalyzed deaminative hydrogenation of amides were the following:

- Deaminative hydrogenation of amides by **Mo^H-PN^HP** follows the same three-step pathway of **Fe-PNP**: (1) amide C=O hydrogenation, (2) C-N bond protonolysis, and (3) aldehyde C=O hydrogenation. However, in the case of **Mo^H-PN^HP**, the rate-limiting step is amide-dependent: In the case of formamides, their rate-limiting step is the C-N bond protonolysis, which is assisted by **Mo^H-PN^HP** and a methanol molecule; in the case of acetamides, their rate-limiting step is the amide C=O hydrogenation, because their more electron-rich carbonyl is harder to hydrogenate than that of formamides.

- Secondary amides and alcohols can block **Mo-PNP** active site. This inhibition is more significant than in the case of **Fe-PNP**, and therefore, the more energy demanding hydrogenations of acetamides can only be performed by **Fe-PNP**.

- The alkaline countercation of **Mo^H-PN^{H}P** stabilizes the catalyst negative charge, while modifying the hydricity of the catalyst. The substitution of the alkaline cation by a larger molecule enhances the catalyst hydricity but it reduces its solubility.

Only three substrates have been computed per catalyst. A broader scope of amides remains to be investigated computationally in future work, as well as a broader scope of base metal Noyori-type catalysts. A broader scope of amides could solidify the conclusions of the thesis, while a broader scope of metals could lead to a rational catalyst design that maximizes the catalyst hydricity while minimizes the formation of adducts between primary or secondary amides and the catalyst. Also, further research on orbital analysis of **Mo^H-PN^{H}P** interaction with its countercation would help to understand how it modifies the catalyst hydricity.

Appendix

Method benchmarking.

In order to select the best method describing the reactivity of **Fe-PNP**, the performance of several density functionals against geometric and energetic benchmarks were tested.

The density functionals used for the study were BLYP, B3LYP, PBE, PBE(0), TPSS, TPSSh, M06-L, M06 and ωB97XD.[69,97–105] Three parameter Grimme dispersion corrections[106] were used in non-GGA functionals without dispersion corrections: BLYP, B3LYP, PBE and PBE(0). The basis sets used were the double-z quality LANL2DZ[107] on iron and 6-31+G** for all other elements.[108]

Catalysts A, **B** and **C** were selected for geometric benchmarking since their molecular structure has been resolved by single-crystal X-ray diffraction.[60] The experimental geometries of **A**, **B** and **C** were compared against DFT gas-phase geometry optimizations (see Graph 0.1). Bonds Fe-P, Fe-N, Fe-C and C≡O were selected for an RMSD analysis because they were the most sensitive to density functional changes. All functionals gave acceptable global RMSD, though functionals PBE(0)+D3, TPSS, TPSSh and M06 were identified as the best candidates, giving global RMSD smaller than 0.02 Å.

Catalyst A   **Catalyst B**   **Catalyst C**
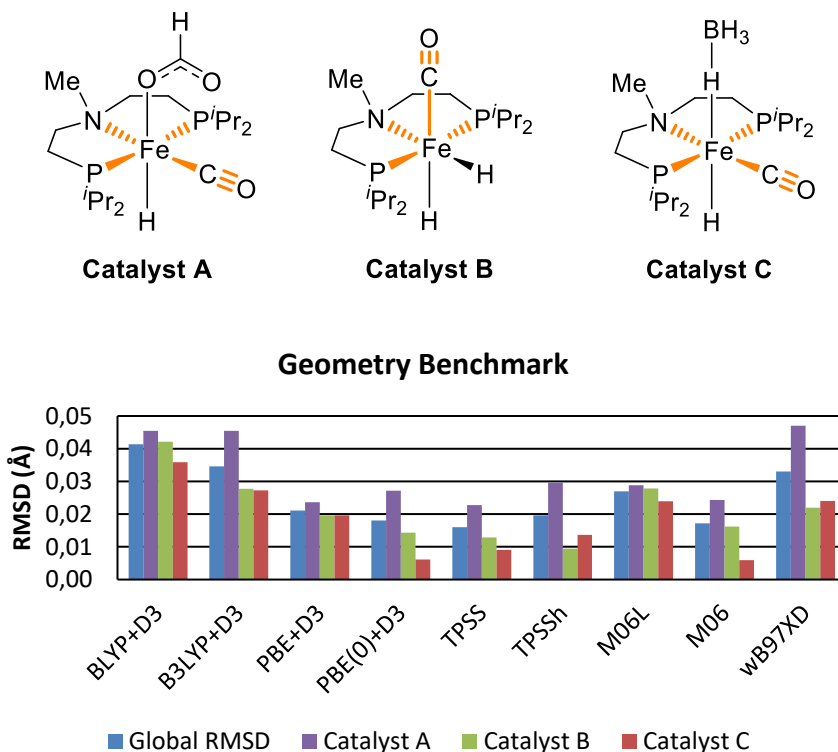
Graph 0.1 Geometry benchmark results of **Catalyst A**, **B** and **C**. Experimental bond distances (Exp.) **1**, **2**, **3**, **4** and **5** by single-crystal x-ray diffraction in front of gas-phase density functional theory geometry optimizations with **BLYP+D3**, **B3LYP**, **PBE+D3**, **TPSS**, **TPSSh**, **M06L+D3**, **M06+D3** and **ωB97XD** functionals and double-z quality basis set (LANL2DZ on iron and 6-31+G** for all other elements).

Next, an energy benchmark of **Reactions 1**, **2** and **3** (see Figure 0.1) was performed to assess the energy accuracy in the calculation of **Fe^H-PN^{Me}P** and **Fe^H-PN^{H}P** complexes, and to discriminate between the functionals that performed best in the geometry benchmark. The tested reactions are the isomerizations of the **Fe-PN^{H}P** and **Fe-PN^{Me}P** complexes (**Reaction 1** and **2** in Figure 0.1) and a hydrogen transfer from a **Fe^H-PN^{H}P** catalyst to a CO_2 molecule (**Reaction 3** in Figure 0.1).

Geometry optimizations of these reactions complexes were performed with the M06 functional. Then we computed their reaction potential energies (ΔE_r) with single point CCSD(T)/cc-pVTZ calculations as energy benchmarks. The coupled-cluster energies were then compared with ΔE_r calculated with functionals PBE(0)+D3, TPSSh and M06 (LANL2TZ on Fe, 6-311+G** on the rest)[109,110] (see Graph 0.2). The DFT computed reaction energies for **Reactions 1** and **2** matched the coupled-cluster energies, with a deviation smaller than 1 kcal mol^{-1}. However, the coupled-cluster computed reaction energy for **Reaction 3** could only be reproduced with the M06 functional. Therefore we concluded that, when compared to the other tested density functionals, the M06 functional provide both the most accurate energies and acceptable geometry optimizations of complexes of amides and iron Noyori-type catalysts.
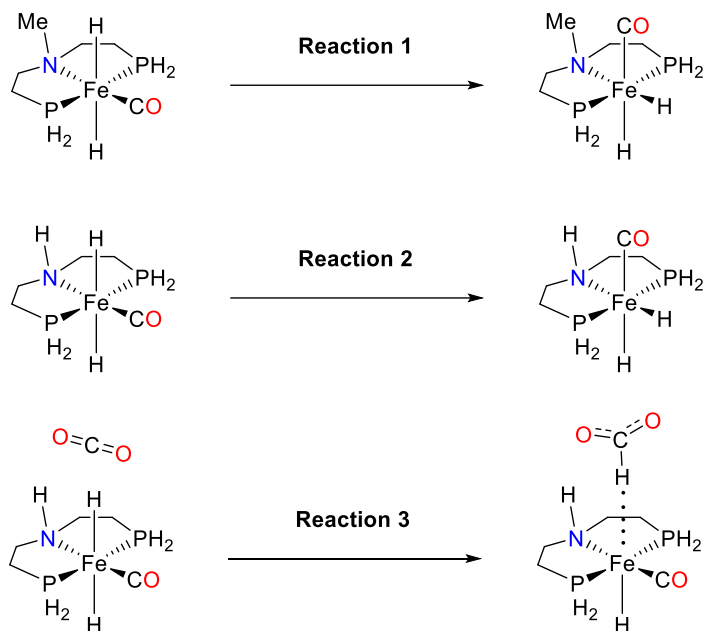
Figure 0.1 Reactions selected for the energy benchmarks. Phosphines iso-propyls were replaced by hydrogens to make CCSD(T) calculations feasible.
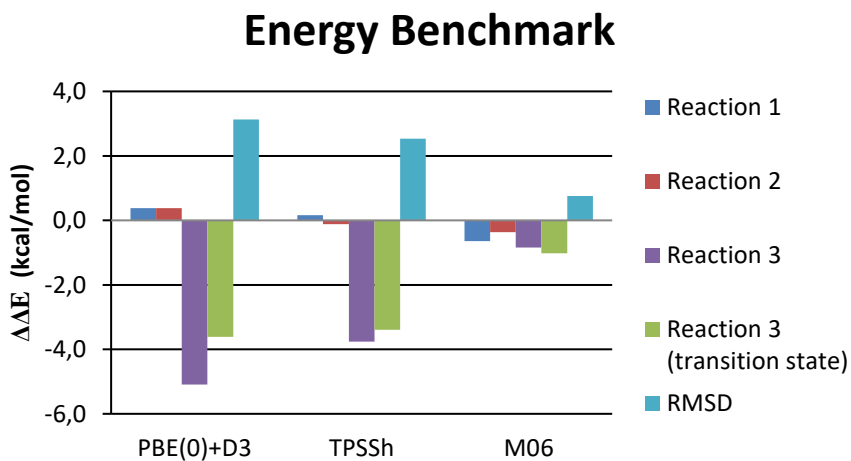
Graph 0.2 Quantitative deviation of DFT $\Delta_r E$ and $\Delta E^{\ddagger}$ relative to CCSD(T) energies of reaction 1, 2, 3 and reaction 3 transition state.

Finally, we tested M06 performance in geometry optimizations of molybdenum Noyori-type catalysts. Single-crystal X-ray diffractions of **Catalysts D**, **E** and **F** were used as geometry benchmarks, and they were compared against DFT geometry optimizations with the M06 functional and double-z quality basis set (LANL2DZ on iron and 6-31+G** for all other elements). Bonds Mo-P, Mo-N, Mo-Cl, Mo-nitrile and Mo-C constitute molybdenum first coordination sphere; therefore, they were selected for an RMSD analysis. M06 RMSD of 0.03 Å (see Graph 0.3) support the use of M06 for geometry optimizations of molybdenum Noyori-type catalysts.
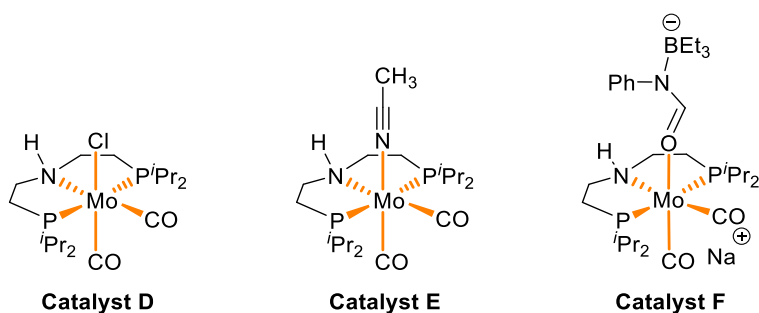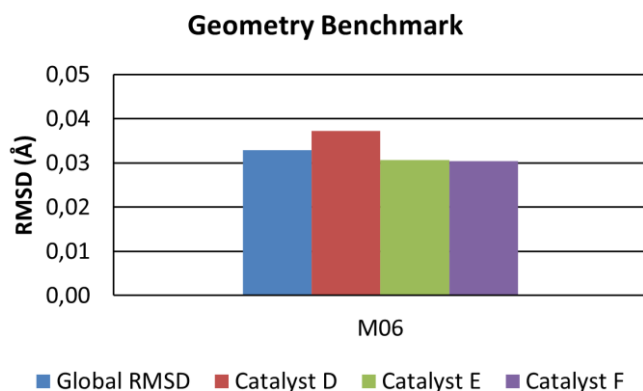
Graph 0.3 Root mean square deviation (Å) of marked distances of **Catalysts D**, **E** and **F** calculated geometries with respect their single-crystal X-ray diffraction geometries.

Selected Methodology

The M06 functional was used for both geometry optimizations (with double-z basis set) and energy refinement (with triple-z basis set). Analytic frequency calculations of stationary points were performed to classify them in either energy minima or saddle points. Free energies were calculated from double-z basis set analytic frequency calculations. Our calculations contain thermal and pressure corrections to emulate the experimental conditions of 373.15 K and 30 atm in the case of **Fe-PNP**-catalyzed reactions, and 373.15 K and 50 atm in the case of $\textbf{Mo}^{\textbf{Cl}}\textbf{-PN}^{\textbf{H}}\textbf{P}$-catalyzed reactions. Solvent effects of THF were introduced with the continuum SMD model. The ultrafine (99,590) grid was used in all calculations for higher numerical accuracy. All calculations were carried out with the Gaussian09 (RevD.01) software package.[111]

Microkinetic models were constructed with the COPASI (version 4.22) software.[83] The models were based on deterministic time course simulations with the LSODA algorithm.[87] Temperature, reaction times and initial concentrations were adjusted to experimental values and will be specified at each case. Hydrogen pressurized reactions were simulated as a constant hydrogen saturated concentration of 0.162M, calculated using the molar fraction of H_2 in a H_2 saturated solution of THF at 33.4 atm and 100 ºC (0.01461 H_2 mol / solution mol), assuming incompresibility of THF and that $[H_2] <<< [THF]$.[94] Elementary reactions and their associated reaction energies and barriers are specified in the supporting information of their corresponding articles.

Bibliography

(1)   Boaz, N. W.; Mackenzie, E. B.; Debenham, S. D.; Large, S. E.;
        Ponasik, J. A. Synthesis and Application of Phosphinoferrocenyl-
        Aminophosphine Ligands for Asymmetric Catalysis. *J. Org. Chem.*
        2005, *70*, 1872–1880. https://doi.org/10.1021/jo048312y.

(2)   Tang, W.; Zhang, X. New Chiral Phosphorus Ligands for
        Enantioselective Hydrogenation. *Chem. Rev.* **2003**, *103*, 3029–3069.
        https://doi.org/10.1021/cr020049i.

(3)   Crabtree, R. H. Homogeneous Catalysis. In *The organometallic
        chemistry of the transition metals*; John Wiley & Sons, Inc.: Hoboken,
        New Jersey, 2014; p 224.

(4)   Crabtree, R. H. Alkyls and Hydrides. In *The organometallic chemistry
        of the transition metals*; John Wiley & Sons, Inc.: Hoboken, New
        Jersey, 2014; p 69.

(5)   Hartwig, J. F. Homogeneous Hydrogenation. In *Organotransition
        metal chemistry: from bonding to catalysis*; Murdzek, J., Ed.;
        University Science Books: Sausalito, Calif, 2010; p 575.

(6)   Hartwig, J. F. Hydrofunctionalization and Oxidative Functionalization
        of Olefins. In *Organotransition metal chemistry: from bonding to
        catalysis*; Murdzek, J., Ed.; University Science Books: Sausalito,
        Calif, 2010; p 667.

(7)   Dobereiner, G. E.; Crabtree, R. H. Dehydrogenation as a Substrate-
        Activating Strategy in Homogeneous Transition-Metal Catalysis.
        Chem. Rev. **2010**, *110*, 681–703. https://doi.org/10.1021/cr900202j.

(8)   Stephan, D. W. Frustrated Lewis Pairs: From Concept to Catalysis.
        Acc. Chem. Res. **2015**, *48*, 306–316.
        https://doi.org/10.1021/ar500375j.

(9)   Stephan, D. W.; Erker, G. Frustrated Lewis Pair Chemistry:
        Development and Perspectives. *Angew. Chemie - Int. Ed.* **2015**, *54*,
        6400–6441. https://doi.org/10.1002/anie.201409800.

(10)   Stephan, D. W. The Broadening Reach of Frustrated Lewis Pair
        Chemistry. *Science (80-.).* **2016**, *354*, aaf7229.
        https://doi.org/10.1126/science.aaf7229.

(11)   Piccirilli, L.; Pinheiro, D. L. J.; Nielsen, M. Recent Progress with
        Pincer Transition Metal Catalysts for Sustainability. *Catalysts* **2020**,

10, 1–115. https://doi.org/10.3390/catal10070773.

(12)   Kuriyama, W.; Matsumoto, T.; Ogata, O.; Ino, Y.; Aoki, K.; Tanaka, S.; Ishida, K.; Kobayashi, T.; Sayo, N.; Saito, T. Catalytic Hydrogenation of Esters. Development of an Efficient Catalyst and Processes for Synthesising (R)-1,2-Propanediol and 2-(l-Menthoxy)Ethanol. *Org. Process Res. Dev.* **2012**, *16*, 166–171. https://doi.org/10.1021/op200234j.

(13)   Filonenko, G. A.; Van Putten, R.; Hensen, E. J. M.; Pidko, E. A. Catalytic (de)Hydrogenation Promoted by Non-Precious Metals-Co, Fe and Mn: Recent Advances in an Emerging Field. *Chem. Soc. Rev.* **2018**, *47*, 1459–1483. https://doi.org/10.1039/c7cs00334j.

(14)   Alig, L.; Fritz, M.; Schneider, S. First-Row Transition Metal (De)Hydrogenation Catalysis Based on Functional Pincer Ligands. *Chem. Rev.* **2018**, *119*, 2681–2751. https://doi.org/10.1021/acs.chemrev.8b00555.

(15)   Peris, E.; Crabtree, R. H. Key Factors in Pincer Ligand Design. *Chem. Soc. Rev.* **2018**, *47*, 1959–1968. https://doi.org/10.1039/c7cs00693d.

(16)   Perutz, R. N.; Sabo-Etienne, S. The σ-CAM Mechanism: σ Complexes as the Basis of σ-Bond Metathesis at Late-Transition-Metal Centers. *Angew. Chemie - Int. Ed.* **2007**, *46*, 2578–2592. https://doi.org/10.1002/anie.200603224.

(17)   Pattabiraman, V. R.; Bode, J. W. Rethinking Amide Bond Synthesis. *Nature* **2011**, *480*, 471–479. https://doi.org/10.1038/nature10702.

(18)   De Figueiredo, R. M.; Suppo, J. S.; Campagne, J. M. Nonclassical Routes for Amide Bond Formation. *Chem. Rev.* **2016**, *116*, 12029–12122. https://doi.org/10.1021/acs.chemrev.6b00237.

(19)   Acosta-Guzmán, P.; Mateus-Gómez, A.; Gamba-Sánchez, D. Direct Transamidation Reactions: Mechanism and Recent Advances. *Molecules* **2018**, *23*, 2382. https://doi.org/10.3390/molecules23092382.

(20)   Valeur, E.; Bradley, M. Amide Bond Formation: Beyond the Myth of Coupling Reagents. *Chem. Soc. Rev.* **2009**, *38*, 606–631. https://doi.org/10.1039/b701677h.

(21)   Mahesh, S.; Tang, K. C.; Raj, M. Amide Bond Activation of Biological Molecules. *Molecules* **2018**, *23*, 2615. https://doi.org/10.3390/molecules23102615.

(22)   Arthur, G. *The Amide Linkage: Selected Structural Aspects in*

Chemistry, Biochemistry, and Materials Science., 1st ed.; Wiley-Interscience: Hoboken, 2000.

(23)   Kar, S.; Goeppert, A.; Kothandaraman, J.; Prakash, G. K. S. Manganese-Catalyzed Sequential Hydrogenation of CO2 to Methanol via Formamide. *ACS Catal.* **2017**, *7*, 6347–6351. https://doi.org/10.1021/acscatal.7b02066.

(24)   Kothandaraman, J.; Goeppert, A.; Czaun, M.; Olah, G. A.; Prakash, G. K. S. Conversion of CO_2 from Air into Methanol Using a Polyamine and a Homogeneous Ruthenium Catalyst. *J. Am. Chem. Soc.* **2016**, *138*, 778–781. https://doi.org/10.1021/jacs.5b12354.

(25)   Rezayee, N. M.; Huff, C. A.; Sanford, M. S. Tandem Amine and Ruthenium-Catalyzed Hydrogenation of CO_2 to Methanol. *J. Am. Chem. Soc.* **2015**, *137*, 1028–1031. https://doi.org/10.1021/ja511329m.

(26)   Kar, S.; Kothandaraman, J.; Goeppert, A.; Prakash, G. K. S. Advances in Catalytic Homogeneous Hydrogenation of Carbon Dioxide to Methanol. *J. CO2 Util.* **2018**, *23*, 212–218. https://doi.org/10.1016/j.jcou.2017.10.023.

(27)   Smith, A. M.; Whyman, R. Review of Methods for the Catalytic Hydrogenation of Carboxamides. *Chem. Rev.* **2014**, *114*, 5477–5510. https://doi.org/10.1021/cr400609m.

(28)   Di Gioia, M. L.; Belsito, E. L.; Leggio, A.; Leotta, V.; Romio, E.; Siciliano, C.; Liguori, A. Reduction of Amide Carbonyl Group and Formation of Modified Amino Acids and Dipeptides. *Tetrahedron Lett.* **2015**, *56*, 2062–2066. https://doi.org/10.1016/j.tetlet.2015.02.074.

(29)   Nystrom, R. F.; Brown, W. G. Reduction of Organic Compounds by Lithium Aluminum Hydride. III. Halides, Quinones, Miscellaneous Nitrogen Compounds. *J. Am. Chem. Soc.* **1948**, *70*, 3738–3740. https://doi.org/10.1021/ja01191a057.

(30)   Weygand, F.; Eberhardt, G.; Linden, H.; Schäfer, F.; Eigen, I. Angewandte Chemie. *Angew. Chem.* **1962**, *53*, 525–531. https://doi.org/10.1016/0009-2509(62)87032-8.

(31)   Jayarathne, U.; Zhang, Y.; Hazari, N.; Bernskoetter, W. H. Selective Iron-Catalyzed Deaminative Hydrogenation of Amides. *Organometallics* **2017**, *36*, 409–416. https://doi.org/10.1021/acs.organomet.6b00816.

(32)   Gusev, D. G. Rethinking the Dehydrogenative Amide Synthesis. *ACS Catal.* **2017**, *7*, 6656–6662. https://doi.org/10.1021/acscatal.7b02415.

(33)   Balaraman, E.; Gnanaprakasam, B.; Shimon, L. J. W.; Milstein, D. Direct Hydrogenation of Amides to Alcohols and Amines under Mild Conditions. *J. Am. Chem. Soc.* **2010**, *132*, 16756–16758. https://doi.org/10.1002/chin.201116025.

(34)   John, J. M.; Bergens, S. H. A Highly Active Catalyst for the Hydrogenation of Amides to Alcohols and Amines. *Angew. Chemie - Int. Ed.* **2011**, *50*, 10377–10380. https://doi.org/10.1002/anie.201103137.

(35)   Cabrero-Antonino, J. R.; Alberico, E.; Drexler, H.-J.; Baumann, W.; Junge, K.; Junge, H.; Beller, M. Efficient Base-Free Hydrogenation of Amides to Alcohols and Amines Catalyzed by Well-Defined Pincer Imidazolyl-Ruthenium Complexes. *ACS Catal.* **2016**, *6*, 47–54. https://doi.org/10.1021/acscatal.5b01955.

(36)   Garg, J. A.; Chakraborty, S.; Ben-David, Y.; Milstein, D. Unprecedented Iron-Catalyzed Selective Hydrogenation of Activated Amides to Amines and Alcohols. *Chem. Commun.* **2016**, *52*, 5285–5288. https://doi.org/10.1039/C6CC01505K.

(37)   Spletstoser, J. T.; White, J. M.; Tunoori, A. R.; Georg, G. I. Mild and Selective Hydrozirconation of Amides to Aldehydes Using Cp 2Zr(H)Cl: Scope and Mechanistic Insight. *J. Am. Chem. Soc.* **2007**, *129*, 3408–3419. https://doi.org/10.1021/ja066362+.

(38)   Jones, G.; Stanforth, S. P. The Vilsmeier Reaction of Non-Aromatic Compounds. *Organic Reactions*. 2000, pp 355–686. https://doi.org/10.1002/0471264180.or056.02.

(39)   Chardon, A.; Morisset, E.; Rouden, J.; Blanchet, J. Recent Advances in Amide Reductions. *Synthesis (Stuttg).* **2018**, *65*, 984–997. https://doi.org/10.1055/s-0036-1589144.

(40)   Amines, A.; Khalimon, A. Y.; Gudun, K. A.; Hayrapetyan, D. Base Metal Catalysts for Deoxygenative Reduction of Amides to Amines. *Catalysts* **2019**, *9*, 490–515.

(41)   Kilner, M.; Tyers, D. V.; Crabtree, S. P.; Wood, M. A. WO 03/093208 A1, 2003.

(42)   Vom Stein, T.; Meuresch, M.; Limper, D.; Schmitz, M.; Hölscher, M.; Coetzee, J.; Cole-Hamilton, D. J.; Klankermayer, J.; Leitner, W. Highly Versatile Catalytic Hydrogenation of Carboxylic and Carbonic

Acid Derivatives Using a Ru-Triphos Complex: Molecular Control over Selectivity and Substrate Scope. *J. Am. Chem. Soc.* **2014**, *136*, 13217–13225. https://doi.org/10.1021/ja506023f.

(43) Kita, Y.; Higuchi, T.; Mashima, K. Hydrogenation of Amides Catalyzed by a Combined Catalytic System of a Ru Complex with a Zinc Salt. *Chem. Commun.* **2014**, *50*, 11211–11213. https://doi.org/10.1039/C4CC04481A.

(44) John, J. M.; Loorthuraja, R.; Antoniuk, E.; Bergens, S. H. Catalytic Hydrogenation of Functionalized Amides Under Basic and Neutral Conditions. *Catal. Sci. Technol.* **2015**, *5*, 1181–1186. https://doi.org/10.1039/C4CY01227E.

(45) Miura, T.; Held, I. E.; Oishi, S.; Naruto, M.; Saito, S. Catalytic Hydrogenation of Unactivated Amides Enabled by Hydrogenation of Catalyst Precursor. *Tetrahedron Lett.* **2013**, *54*, 2674–2678. https://doi.org/10.1016/j.tetlet.2013.03.047.

(46) Takada, Y.; Iida, M.; Iida, K.; Miura, T.; Saito, S. Versatile Ruthenium Complex "RuPCY" for Directed Catalytic Hydrogen Management in Organic Synthesis. *J. Synth. Org. Chem.* **2016**, *74*, 1078–1089. https://doi.org/10.5059/yukigoseikyokaishi.74.1078.

(47) Zhang, L.; Han, Z.; Zhao, X.; Wang, Z.; Ding, K. Highly Efficient Ruthenium-Catalyzed N-Formylation of Amines with H_2 and CO_2. *Angew. Chemie - Int. Ed.* **2015**, *54*, 6186–6189. https://doi.org/10.1002/anie.201500939.

(48) Schneck, F.; Assmann, M.; Balmer, M.; Harms, K.; Langer, R. Selective Hydrogenation of Amides to Amines and Alcohols Catalyzed by Improved Iron Pincer Complexes. *Organometallics* **2016**, *35*, 1931–1943. https://doi.org/10.1021/acs.organomet.6b00251.

(49) Rezayee, N. M.; Samblanet, D. C.; Sanford, M. S. Iron-Catalyzed Hydrogenation of Amides to Alcohols and Amines. *ACS Catal.* **2016**, *6*, 6377–6383. https://doi.org/10.1021/acscatal.6b01454.

(50) Shi, L.; Tan, X.; Long, J.; Xiong, X.; Yang, S.; Xue, P.; Lv, H.; Zhang, X. Direct Catalytic Hydrogenation of Simple Amides: A Highly Efficient Approach from Amides to Amines and Alcohols. *Chem. - A Eur. J.* **2017**, *23*, 546–548. https://doi.org/10.1002/chem.201604904.

(51) Artús Suàrez, L.; Culakova, Z.; Balcells, D.; Bernskoetter, W. H.; Eisenstein, O.; Goldberg, K. I.; Hazari, N.; Tilset, M.; Nova, A. The Key Role of the Hemiaminal Intermediate in the Iron-Catalyzed

Deaminative Hydrogenation of Amides. *ACS Catal.* **2018**, *8*, 8751–8762. https://doi.org/10.1021/acscatal.8b02184.

(52)   Lane, E. M.; Zhang, Y.; Hazari, N.; Bernskoetter, W. H. Sequential Hydrogenation of CO 2 to Methanol Using a Pincer Iron Catalyst. *Organometallics* **2019**, *38*, 3084–3091. https://doi.org/10.1021/acs.organomet.9b00413.

(53)   Artús Suàrez, L.; Jayarathne, U.; Balcells, D.; Bernskoetter, W. H.; Hazari, N.; Jaraiz, M.; Nova, A. Rational Selection of Co-Catalysts for the Deaminative Hydrogenation of Amides. *Chem. Sci.* **2020**, *11*, 2225–2230. https://doi.org/10.1039/C9SC03812D.

(54)   Leischner, T.; Artús Suàrez, L.; Spannenberg, A.; Junge, K.; Nova, A.; Beller, M. Highly Selective Hydrogenation of Amides Catalysed by a Molybdenum Pincer Complex: Scope and Mechanism. *Chem. Sci.* **2019**, *10*, 10566–10576. https://doi.org/10.1039/c9sc03453f.

(55)   Papa, V.; Cabrero-Antonino, J. R.; Alberico, E.; Spanneberg, A.; Junge, K.; Junge, H.; Beller, M. Efficient and Selective Hydrogenation of Amides to Alcohols and Amines Using a Well-Defined Manganese-PNN Pincer Complex. *Chem. Sci.* **2017**, *8*, 3576–3585. https://doi.org/10.1039/c7sc00138j.

(56)   Alberico, E.; Sponholz, P.; Cordes, C.; Nielsen, M.; Drexler, H. J.; Baumann, W.; Junge, H.; Beller, M. Selective Hydrogen Production from Methanol with a Defined Iron Pincer Catalyst under Mild Conditions. *Angew. Chemie - Int. Ed.* **2013**, *52*, 14162–14166. https://doi.org/10.1002/anie.201307224.

(57)   Bornschein, C.; Werkmeister, S.; Wendt, B.; Jiao, H.; Alberico, E.; Baumann, W.; Junge, H.; Junge, K.; Beller, M. Mild and Selective Hydrogenation of Aromatic and Aliphatic (Di)Nitriles with a Well-Defined Iron Pincer Complex. *Nat. Commun.* **2014**, *5*, 4111–4121. https://doi.org/10.1038/ncomms5111.

(58)   Chakraborty, S.; Dai, H.; Bhattacharya, P.; Fairweather, N. T.; Gibson, M. S.; Krause, J. A.; Guan, H. Iron-Based Catalysts for the Hydrogenation of Esters to Alcohols. *J. Am. Chem. Soc.* **2014**, *136*, 7869–7872. https://doi.org/10.1021/ja504034q.

(59)   Werkmeister, S.; Junge, K.; Wendt, B.; Alberico, E.; Jiao, H.; Baumann, W.; Junge, H.; Gallou, F.; Beller, M. Hydrogenation of Esters to Alcohols with a Well-Defined Iron Complex. *Angew. Chemie - Int. Ed.* **2014**, No. 33, 8722–8726. https://doi.org/10.1002/anie.201402542.

(60)   Zhang, Y.; MacIntosh, A. D.; Wong, J. L.; Bielinski, E. A.; Williard, P. G.; Mercado, B. Q.; Hazari, N.; Bernskoetter, W. H. Iron Catalyzed CO2 Hydrogenation to Formate Enhanced by Lewis Acid Co-Catalysts. *Chem. Sci.* **2015**, *6*, 4291–4299. https://doi.org/10.1039/C5SC01467K.

(61)   Xu, R.; Chakraborty, S.; Bellows, S. M.; Yuan, H.; Cundari, T. R.; Jones, W. D. Iron-Catalyzed Homogeneous Hydrogenation of Alkenes under Mild Conditions by a Stepwise, Bifunctional Mechanism. *ACS Catal.* **2016**, *6*, 2127–2135. https://doi.org/10.1021/acscatal.5b02674.

(62)   Chakraborty, S.; Brennessel, W. W.; Jones, W. D. A Molecular Iron Catalyst for the Acceptorless Dehydrogenation and Hydrogenation of N-Heterocycles. *J. Am. Chem. Soc.* **2014**, *136*, 8564–8567. https://doi.org/10.1021/ja504523b.

(63)   Bielinski, E. A.; Förster, M.; Zhang, Y.; Bernskoetter, W. H.; Hazari, N.; Holthausen, M. C. Base-Free Methanol Dehydrogenation Using a Pincer-Supported Iron Compound and Lewis Acid Co-Catalyst. *ACS Catal.* **2015**, *5*, 2404–2415. https://doi.org/10.1021/acscatal.5b00137.

(64)   Lane, E. M.; Uttley, K. B.; Hazari, N.; Bernskoetter, W. Iron-Catalyzed Amide Formation from the Dehydrogenative Coupling of Alcohols and Secondary Amines. *Organometallics* **2017**, *36*, 2020–2025. https://doi.org/10.1021/acs.organomet.7b00258.

(65)   Leischner, T.; Spannenberg, A.; Junge, K.; Beller, M. Molecular Defined Molybdenum-Pincer Complexes and Their Application in Catalytic Hydrogenations. *Organometallics* **2018**, *37*, 4402–4408. https://doi.org/10.1021/acs.organomet.8b00410.

(66)   Hohenberg, P.; Kohn, W. Inhomogeneous Electron Gas. *Phys. Rev.* **1964**, *136*, B864–B871. https://doi.org/10.1103/PhysRev.136.B864.

(67)   Levy, M. Elementary Concepts in Density Functional Theory. In *Theoretical and Computational Chemistry*; Elsevier, 1996; Vol. 4, pp 3–24. https://doi.org/10.1016/S1380-7323(96)80083-5.

(68)   Kohn, W.; Sham, L. J. Self-Consistent Equations Including Exchange and Correlation Effects. *Phys. Rev.* **1965**, *140*, A1133–A1138. https://doi.org/http://dx.doi.org/10.1103/PhysRev.140.A1133.

(69)   Zhao, Y.; Truhlar, D. G. The M06 Suite of Density Functionals for Main Group Thermochemistry, Thermochemical Kinetics, Noncovalent Interactions, Excited States, and Transition Elements: Two New Functionals and Systematic Testing of Four M06-Class Functionals and 12 Other Function. *Theor. Chem. Acc.* **2008**, *120*,

215–241. https://doi.org/10.1007/s00214-007-0310-x.

(70)   Ramabhadran, R. O.; Raghavachari, K. Extrapolation to the Gold-Standard in Quantum Chemistry: Computationally Efficient and Accurate CCSD(T) Energies for Large Molecules Using an Automated Thermochemical Hierarchy. *J. Chem. Theory Comput.* **2013**, *9*, 3986–3994. https://doi.org/10.1021/ct400465q.

(71)   Balabanov, N. B.; Peterson, K. A. Systematically Convergent Basis Sets for Transition Metals. I. All-Electron Correlation Consistent Basis Sets for the 3d Elements Sc-Zn. *J. Chem. Phys.* **2005**, *123*, 064107–064123. https://doi.org/10.1063/1.1998907.

(72)   Marenich, A. V.; Cramer, C. J.; Truhlar, D. G. Universal Solvation Model Based on Solute Electron Density and on a Continuum Model of the Solvent Defined by the Bulk Dielectric Constant and Atomic Surface Tensions. *J. Phys. Chem. B* **2009**, *113*, 6378–6396. https://doi.org/10.1021/jp810292n.

(73)   Lewars, E. G. *Computational Chemistry. Introduction to the Theory and Applications of Molecular and Quantum Mechanics.*, 3rd ed.; Springer International Publishing: Peterborough, ON, Canada, 2016; Vol. 43. https://doi.org/10.1007/978-3-319-30916-3.

(74)   Cramer, C. J. *Essentials of Computational Chemistry*, 2nd ed.; John Wiley & Sons, Ltd: West Sussex, England, 2004; Vol. 69.

(75)   Miertuš, S.; Scrocco, E.; Tomasi, J. Electrostatic Interaction of a Solute with a Continuum. A Direct Utilizaion of AB Initio Molecular Potentials for the Prevision of Solvent Effects. *Chem. Phys.* **1981**, *55*, 117–129. https://doi.org/10.1016/0301-0104(81)85090-2.

(76)   Tomasi, J.; Mennucci, B.; Cancès, E. The IEF Version of the PCM Solvation Method : An Overview of a New Method Addressed to Study Molecular Solutes at the QM Ab Initio Level. *J. Mol. Struct.* **1999**, *464*, 211–226.

(77)   Marenich, A. V.; Cramer, C. J.; Truhlar, D. G. Generalized Born Solvation Model SM12. *J. Chem. Theory Comput.* **2013**, *9*, 609–620. https://doi.org/10.1021/ct300900e.

(78)   Klamt, A.; Schüürmann, G. COSMO: A New Approach to Dielectric Screening in Solvents with Explicit Expressions for the Screening Energy and Its Gradient. *J. Chem. Soc. Perkin Trans. 2* **1993**, No. 5, 799–805. https://doi.org/10.1039/P29930000799.

(79)   Mikkelsen, K. V.; Ågren, H.; Jensen, H. J. A.; Helgaker, T. A

Multiconfigurational Self-Consistent Reaction-Field Method. *J. Chem. Phys.* **1988**, *89*, 3086–3095. https://doi.org/10.1063/1.454965.

(80)   Cortis, C. M.; Langlois, J. M.; Beachy, M. D.; Friesner, R. A. Quantum Mechanical Geometry Optimization in Solution Using a Finite Element Continuum Electrostatics Method. *J. Chem. Phys.* **1996**, *105*, 5472–5484. https://doi.org/10.1063/1.472388.

(81)   Atkins, P.; de Paula, J.; Keller, J. *Atkins' Physical Chemistry*, 11th Editi.; Oxford University Press: Oxford, 2018.

(82)   Jensen, F. *Introduction to Computational Chemistry*, 3rd Editio.; John Wiley & Sons Inc: New York, United States, 2017.

(83)   Hoops, S.; Gauges, R.; Lee, C.; Pahle, J.; Simus, N.; Singhal, M.; Xu, L.; Mendes, P.; Kummer, U. COPASI - A Complex Pathway SImulator. *Bioinformatics* **2006**, *22*, 3067–3074. https://doi.org/10.1093/bioinformatics/btl485.

(84)   Hindmarsh, A. C. ODEPACK, a Systematized Collection of Ode Solvers. 1982, pp 427–429.

(85)   Hindmarsh, A. C. LSODE and LSODI, Two New Initial Value Ordinary Differential Equation Solvers. *ACM SIGNUM Newsl.* **1980**, *15*, 10–11. https://doi.org/10.1017/CBO9781107415324.004.

(86)   Hindmarsh, A. C. *ODE Solvers for Use with the Method of Lines*; Vichnevetsky, R., Stepleman, R. S., Eds.; IMACS: New Brunswick, 1981.

(87)   Petzold, L. Automatic Selection of Methods for Solving Stiff and Nonstiff Systems of Ordinary Differential Equations. *SIAM J Sci Stat Comput* **1983**, *4*, 136–148. https://doi.org/10.1137/0904010.

(88)   Qu, S.; Dai, H.; Dang, Y.; Song, C.; Wang, Z.-X. X.; Guan, H. Computational Mechanistic Study of Fe-Catalyzed Hydrogenation of Esters to Alcohols: Improving Catalysis by Accelerating Precatalyst Activation with a Lewis Base. *ACS Catal.* **2014**, *4*, 4377–4388. https://doi.org/10.1021/cs501089h.

(89)   Chakraborty, S.; Lagaditis, P. O.; Förster, M.; Bielinski, E. A.; Hazari, N.; Holthausen, M. C.; Jones, W. D.; Schneider, S. Well-Defined Iron Catalysts for the Acceptorless Reversible Dehydrogenation-Hydrogenation of Alcohols and Ketones. *ACS Catal.* **2014**, *4*, 3994–4003. https://doi.org/10.1021/cs5009656.

(90)   Chen, X.; Jing, Y.; Yang, X. Unexpected Direct Hydride Transfer Mechanism for the Hydrogenation of Ethyl Acetate to Ethanol

Catalyzed by SNS Pincer Ruthenium Complexes. *Chem. - A Eur. J.* **2016**, *22*, 1950–1957. https://doi.org/10.1002/chem.201504058.

(91)   Nguyen, D. H.; Trivelli, X.; Capet, F.; Paul, J. F.; Dumeignil, F.; Gauvin, R. M. Manganese Pincer Complexes for the Base-Free, Acceptorless Dehydrogenative Coupling of Alcohols to Esters: Development, Scope, and Understanding. *ACS Catal.* **2017**, *7*, 2022–2032. https://doi.org/10.1021/acscatal.6b03554.

(92)   Cabrero-Antonino, J. R.; Adam, R.; Papa, V.; Beller, M. Homogeneous and Heterogeneous Catalytic Reduction of Amides and Related Compounds Using Molecular Hydrogen. *Nat. Commun.* **2020**, *11*, 1–18. https://doi.org/10.1038/s41467-020-17588-5.

(93)   Dub, P. A.; Gordon, J. C. The Role of the Metal-Bound N–H Functionality in Noyori-Type Molecular Catalysts. *Nat. Rev. Chem.* **2018**, *2*, 396–408. https://doi.org/10.1038/s41570-018-0049-z.

(94)   Brunner, E. Solubility of Hydrogen in 10 Organic Solvents at 298.15, 323.15, and 373.15 K. *J. Chem. Eng. Data* **1985**, *30*, 269–273. https://doi.org/10.1021/je00041a010.

(95)   Plata, R. E.; Singleton, D. A. A Case Study of the Mechanism of Alcohol-Mediated Morita Baylis-Hillman Reactions. the Importance of Experimental Observations. *J. Am. Chem. Soc.* **2015**, *137*, 3811–3826. https://doi.org/10.1021/ja5111392.

(96)   Besora, M.; Vidossich, P.; Lledós, A.; Ujaque, G.; Maseras, F. Calculation of Reaction Free Energies in Solution: A Comparison of Current Approaches. *J. Phys. Chem. A* **2018**, *122*, 1392–1399. https://doi.org/10.1021/acs.jpca.7b11580.

(97)   Becke, A. D. Density-Functional Thermochemistry. III. The Role of Exact Exchange. *J. Chem. Phys.* **1993**, *98*, 5648–5652. https://doi.org/10.1063/1.464913.

(98)   Adamo, C.; Barone, V. Toward Reliable Density Functional Methods without Adjustable Parameters: The PBE0 Model. *J. Chem. Phys.* **1999**, *110*, 6158–6170. https://doi.org/10.1063/1.478522.

(99)   Tao, J.; Perdew, J. P.; Staroverov, V. N.; Scuseria, G. E. Climbing the Density Functional Ladder: Nonempirical Meta–Generalized Gradient Approximation Designed for Molecules and Solids. *Phys. Rev. Lett.* **2003**, *91*, 3–6. https://doi.org/10.1103/PhysRevLett.91.146401.

(100) Chai, J.-D.; Head-Gordon, M. Long-Range Corrected Hybrid Density Functionals with Damped Atom–Atom Dispersion Corrections. *Phys.*

Chem. Chem. Phys. **2008**, *10*, 6615–6620.
https://doi.org/10.1039/b810189b.

(101) Becke, A. D. Density-Functional Exchange-Energy Approximation With Correct Asymptotic Behavior. *Phys. Rev. A* **1988**, *38*, 3098–3100. https://doi.org/10.1103/PhysRevA.38.3098.

(102) Lee, C.; Yang, W.; Parr, R. G. Development of the Colle-Salvetti Correlation-Energy Formula into a Functional of the Electron Density. *Phys. Rev. B* **1988**, *37*, 785–789. https://doi.org/10.1103/PhysRevB.37.785.

(103) Miehlich, B.; Savin, A.; Stoll, H.; Preuss, H. Results Obtained with the Correlation Energy Density Functionals of Becke and Lee, Yang and Parr. *Chem. Phys. Lett.* **1989**, *157*, 200–206. https://doi.org/10.1016/0009-2614(89)87234-3.

(104) Perdew, J. P.; Burke, K.; Ernzerhof, M. Generalized Gradient Approximation Made Simple- ERRATA. *Phys. Rev. Lett.* **1996**, *77*, 3865–3868. https://doi.org/10.1103/PhysRevLett.77.3865.

(105) Zhao, Y.; Truhlar, D. G. A New Local Density Functional for Main-Group Thermochemistry, Transition Metal Bonding, Thermochemical Kinetics, and Noncovalent Interactions. *J. Chem. Phys.* **2006**, *125*, 1–17. https://doi.org/10.1063/1.2370993.

(106) Grimme, S.; Antony, J.; Ehrlich, S.; Krieg, H. A Consistent and Accurate Ab Initio Parametrization of Density Functional Dispersion Correction (DFT-D) for the 94 Elements H-Pu. *J. Chem. Phys.* **2010**, *132*, 1–18. https://doi.org/10.1063/1.3382344.

(107) Hay, P. J.; Wadt, W. R. Ab Initio Effective Core Potentials for Molecular Calculations. Potentials for the Transition Metal Atoms Sc to Hg. *J. Chem. Phys.* **1985**, *82*, 270–283. https://doi.org/10.1063/1.448799.

(108) Hehre, W. J.; Ditchfield, R.; Pople, J. A. Self—Consistent Molecular Orbital Methods. XII. Further Extensions of Gaussian—Type Basis Sets for Use in Molecular Orbital Studies of Organic Molecules. *J. Chem. Phys.* **1972**, *56*, 2257–2261. https://doi.org/10.1063/1.1677527.

(109) Krishnan, R.; Binkley, J. S.; Seeger, R.; Pople, J. A. Self-Consistent Molecular Orbital Methods. XX. A Basis Set For Correlated Wave Functions. *J. Chem. Phys.* **1980**, *72*, 650–654. https://doi.org/10.1063/1.438955.

(110) McLean, A. D.; Chandler, G. S. Contracted Gaussian Basis Sets for

Molecular Calculations. I. Second Row Atoms, Z=11-18. *J. Chem. Phys.* **1980**, *72*, 5639–5648. https://doi.org/10.1063/1.438980.

(111)   Gaussian 09, Revision D.01, M. J. Frisch, G. W. Trucks, H. B. Schlegel, G. E. Scuseria, M. A. Robb, J. R. Cheeseman, G. Scalmani, V. Barone, B. Mennucci, G. A. Petersson, H. Nakatsuji, M. Caricato, X. Li, H. P. Hratchian, A. F. Izmaylov, J. Bloino, G. Zheng, J. L. Sonnenberg, M. Hada, M. Ehara, K. Toyota, R. Fukuda, J. Hasegawa, M. Ishida, T. Nakajima, Y. Honda, O. Kitao, H. Nakai, T. Vreven, J. A. Montgomery, Jr., J. E. Peralta, F. Ogliaro, M. Bearpark, J. J. Heyd, E. Brothers, K. N. Kudin, V. N. Staroverov, T. Keith, R. Kobayashi, J. Normand, K. Raghavachari, A. Rendell, J. C. Burant, S. S. Iyengar, J. Tomasi, M. Cossi, N. Rega, J. M. Millam, M. Klene, J. E. Knox, J. B. Cross, V. Bakken, C. Adamo, J. Jaramillo, R. Gomperts, R. E. Stratmann, O. Yazyev, A. J. Austin, R. Cammi, C. Pomelli, J. W. Ochterski, R. L. Martin, K. Morokuma, V. G. Zakrzewski, G. A. Voth, P. Salvador, J. J. Dannenberg, S. Dapprich, A. D. Daniels, O. Farkas, J. B. Foresman, J. V. Ortiz, J. Cioslowski, and D. J. Fox, Gaussian, Inc., Wallingford CT, 2013.

Paper II

Artús Suàrez, L.; Jayarathne, U.; Balcells, D; Bernskoetter, W. H.; Hazari, N.; Jaraiz, M.; Nova, A. Chem. Sci., **2020**, *11*, 2225-2230

EDGE ARTICLE

Check for updates

Rational selection of co-catalysts for the deaminative hydrogenation of amides†

Lluís Artús Suàrez, [ID] ‡[a] Upul Jayarathne,‡[b] David Balcells,[a] Wesley H. Bernskoetter, [ID] *[b] Nilay Hazari, [ID] [c] Martín Jaraiz [ID] [de] and Ainara Nova [ID] *[af]

The catalytic hydrogenation of amides is an atom economical method to synthesize amines. Previously, it was serendipitously discovered that the combination of a secondary amide co-catalyst with (^{iPr}PNP) Fe(H)(CO) (^{iPr}PNP = N[CH$_2$CH$_2$(P^{i}Pr$_2$)]$_2^-$), results in a highly active base metal system for deaminative amide hydrogenation. Here, we use DFT to develop an improved co-catalyst for amide hydrogenation. Initially, we computationally evaluated the ability of a series of co-catalysts to accelerate the turnover-limiting proton transfer during C−N bond cleavage and poison the (^{iPr}PNP)Fe(H)(CO) catalyst through a side reaction. TBD (triazabicyclodecene) was identified as the leading co-catalyst. It was experimentally confirmed that when TBD is combined with (^{iPr}PNP)Fe(H)(CO) a remarkably active system for amide hydrogenation is generated. TBD also enhances the activity of other catalysts for amide hydrogenation and our results provide guidelines for the rational design of future co-catalysts.

Introduction

The selective hydrogenation of carbonyl complexes is one of the most important and widely used catalytic reactions in organic synthesis.[1–3] However, the reduction of electron rich carboxylic acid derivatives, such as amides, is still difficult.[4,5] The ubiquity of the amide functional group in biological systems, pharmaceuticals, and industrial chemicals[6] has spurred considerable effort to create efficient catalytic systems for amide hydrogenation. Nevertheless, amides are still typically reduced using waste generating stoichiometric reagents, such as LiAlH$_4$, and to date only a small number of homogenous catalysts can

directly hydrogenate amides to amines.[5,7–12] These catalysts, which include both precious and base metal systems, provide proof-of-principle that this atom economic transformation is possible, but can still be improved.[1]

Current mechanistic models for transition metal catalyzed amide reduction, in particular deaminative hydrogenation to produce an amine and an alcohol, propose a sequential reduction of the amide to an intermediate hemiaminal (step 1, Scheme 1), which then undergoes C−N bond cleavage to yield an amine and an aldehyde (step 2). Subsequent hydrogenation of the aldehyde affords the corresponding alcohol (step 3).[13,14]

Most well-defined catalysts for deaminative hydrogenation rely on a Noyori-type,[14,15] bifunctional pathway whereby a metal-hydride and adjacent ligand based proton are delivered to the carbonyl C=O moiety (Scheme 1). Intriguingly, recent mechanistic studies indicate that while the Noyori-type catalyst structure is essential for facilitating the dihydrogen addition steps of the process (1 and 3, in Scheme 1), the proton transfer between the O- and N-ends of the hemiaminal (step 2), which

[a] *Hylleraas Centre for Quantum Molecular Sciences, Department of Chemistry, University of Oslo, P. O. Box 1033, Blindern, N-0315 Oslo, Norway. E-mail: ainara. nova@kjemi.uio.no*

[b] *Department of Chemistry, University of Missouri, Columbia, Missouri, 65211, USA*

[c] *Department of Chemistry, Yale University, P. O. Box 208107, New Haven, Connecticut, 06520, USA*

[d] *Department of Electronics, ETSIT, University of Valladolid, Paseo Belén 15, 47011 Valladolid, Spain*

[e] *IU CINQUIMA, University of Valladolid, Paseo de Belén 7, 47011 Valladolid, Spain*

[f] *Department of Chemistry, UiT-The Arctic University of Norway, N-9037 Tromsø, Norway*

† Electronic supplementary information (ESI) available: Experimental details (including procedure for co-catalyst screening and synthesis of (^{Ph}PN^{H}P) RuH(CO)(HCONPh)) and computational details (including information on the microkinetic models with DMF and 4-formylmorpholine, results obtained with diphenylformanilide, and optimized coordinates. CCDC 1943231. For ESI and crystallographic data in CIF or other electronic format see DOI: 10.1039/c9sc03812d

‡ These authors contributed equally to this study.
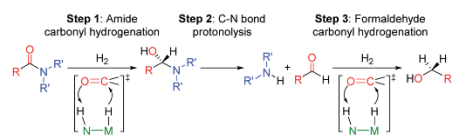
Scheme 1 Proposed reaction steps for the deaminative hydrogenation of amides to amines and methanol catalyzed by Noyori type catalysts represented as N(H)−M(H).

129

triggers the cleavage of the C–N bond, does not involve necessarily the metal catalyst.[13] In addition, step 2 is the turnover-limiting step, indicating that novel methods to facilitate hemiaminal cleavage are required to improve catalytic amide hydrogenation.

Our laboratories have previously investigated amide hydrogenation catalyzed by the iron(II) complex, $(^{iPr}PNP)Fe(H)(CO)$ $(^{iPr}PNP = N[CH_2CH_2(P^iPr_2)]_2^-)$ ($\mathbf{Fe^N}$) using both computational and experimental methods (Scheme 2).[5,13] In deaminative amide hydrogenation using $\mathbf{Fe^N}$, a key serendipitous finding was that the reaction is promoted by a co-catalytic amount of a secondary amide (formamide in Scheme 2). This effect was particularly pronounced in the hydrogenation of tertiary alkylic amides, such as DMF, which are important because they are key intermediates in the homogeneous hydrogenation of CO_2 to methanol mediated by amines.[16,17] The interplay of the two amide equivalents (i.e. one reactant and one co-catalyst) adds complexity to the mechanism. Computational studies indicate that the secondary amide lowers the barrier to the proton transfer that occurs in hemiaminal C–N bond cleavage ($\Delta G_{HT}^{\ddagger}$, in Scheme 2) because the NH moiety acts as a proton-shuttle.[13] However, the use of a secondary amide as a co-catalyst has two major pitfalls: (1) secondary amides can form stable adducts with $\mathbf{Fe^N}$ (ΔG_{add}, in Scheme 2) via 1,2-addition across the iron–amide bond, which lowers the concentration of the active species in catalysis; and (2) the amide co-catalyst can be consumed during the reaction, which undermines its contribution as a co-catalyst and introduces a product separation problem.[5] Here, we use a rational approach involving DFT

calculations to design co-catalysts tailored for the deaminative hydrogenation of tertiary amides. Our best co-catalyst, tri-azabicyclodecene (TBD), acts as push–pull proton shuttle for C–N bond cleavage, and leads to significant improvement in iron catalyzed deaminative amide hydrogenation. Importantly, the improvement from TBD also occurs for a number of other transition metal catalysts for deaminative amide hydrogenation, suggesting that the addition of co-catalysts of this type is a general strategy for improving amide reduction.
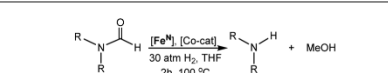
Results and discussion

Computational co-catalyst design

On the basis of the mechanism shown in Scheme 2, DFT calculations were performed on a series of potential organic co-catalysts for the hydrogenation of DMF using $\mathbf{Fe^N}$ (Table 1; see ESI† for computational details). The co-catalysts assessed included molecules with either single site hydrogen bond donors (entries 4–7 and 10) or with both hydrogen bond donor and acceptor sites which could act as push–pull proton shuttles (entries 1–3, 8 and 11). Various aryl and alkyl substituents (i.e. H, Me, ^iPr, ^tBu, Ph) were introduced into the pool of co-catalysts, to sample a wide range of stereoelectronic effects. In molecules with C=O or C=N functional groups, only electron-rich systems were chosen to minimize the hydrogenation of the co-catalyst. Although there are co-catalysts that are hydrogenated when used as reactants (e.g. formanilide and acetamide),[5] when they are used in catalytic concentrations their consumption is slower than that of the reactants, enabling their co-catalytic effect.[13] The ability of each potential co-catalyst to assist with the hemiaminal proton transfer[5,18,19] involved in the C–N bond cleavage (step 2 in Scheme 1) was quantified by computing the transition state(s) associated with this process ($\Delta G_{HT}^{\ddagger}$; Scheme 2 and Fig. 1), which can be either concerted (with TBD, methanol and morpholine) or step-wise (all other co-catalysts). In the latter, the N-protonation of the hemiaminal is followed by its O-deprotonation, which is rate-limiting for all co-catalysts except urea. The thermodynamic preference of the co-catalyst to trap the iron complex was quantified by computing the free energy for the formation of the off-cycle adducts from $\mathbf{Fe^N}$ (ΔG_{add}; Scheme 2 and Fig. 1). In this framework, all co-catalysts were screened with the aim of finding an optimal balance between a low $\Delta G_{HT}^{\ddagger}$ and a thermoneutral or endergonic value of ΔG_{add}. Catalyst hydrogenation (ΔG_{hyd}; Scheme 2) competes with adduct formation and, thus, there is an interplay between the free energies of both reactions. In the case of $\mathbf{Fe^N}$, ΔG_{hyd} (which will depend on the nature of the catalyst) was calculated to be -10.2 kcal mol^{-1} under the experimental conditions.[13] The value of $\Delta G_{add} - \Delta G_{hyd}$ (ΔG_P, in Table 1) is therefore a measure of how adduct formation may limit the reaction by catalyst poisoning (i.e. a more positive value is indicative of less deactivation). For example, the production of methanol may be expected to inhibit catalysis by adduct formation with $\mathbf{Fe^N}$ (entry 7; $\Delta G_{add} = -6.9$ kcal mol^{-1}). However, catalyst hydrogenation is even more favorable ($\Delta G_{hyd} = -10.2$ kcal mol^{-1}) making the $\mathbf{FeH^{NH}}$ the likely preferred species ($\Delta G_P = 3.3$ kcal mol^{-1}).
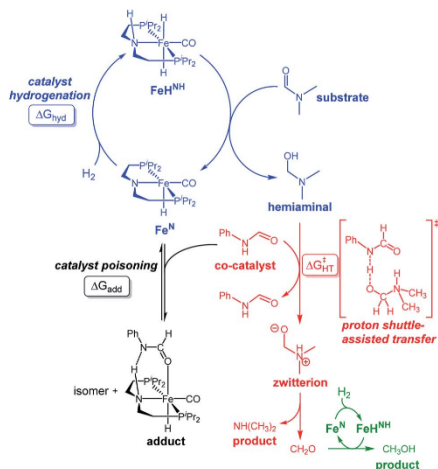
Scheme 2 Reaction mechanism for the deaminative hydrogenation of amides by Noyori-type catalysts. Isomer = Fe N-bound form of the adduct. Color code: hemiaminal formation (blue), C–N cleavage by proton transfer (red), formaldehyde hydrogenation (green) and adduct formation (black).

130

Table 1 Evaluation of co-catalysts for the hydrogenation of tertiary amides with Fe^N

Entry	Co-catalyst	$\Delta G_{HT}^{\ddagger}{}^{a}$	$\Delta G_{add}{}^{b}$	$\Delta G_{P}{}^{c}$	TON^d	Conv.^{d}
1		21.3	−1.5	8.7	830	59%
2		25.3	−8.3	1.9	780	55%
3		22.6	−12.2	−2.0	630	45%
4		24.3	−11.5	−1.3	—	—
5		21.8	−11.4	−1.2	—	—
6		25.5	4.4	14.6	560	40%
7	CH$_3$OH	29.6	−6.9	3.3	510	37%
8		22.3	−9.3	1.4	440	31%
9	No additive	—	—	—	320	22%
10		34.6	8.0	18.2	320	22%
11		35.3	−8.8	1.4	90	6%

^{a} $\Delta G_{HT}^{\ddagger}$ (in kcal mol^{-1}) corresponds to the calculated energy of the proton-transfer transition state with the highest energy for DMF assisted by the co-catalysts (Scheme 2, Fig. 1). ^{b} ΔG_{add} (in kcal mol^{-1}) corresponds to the calculated energy for the formation of the adduct (isomer with the lowest energy) formed by [Fe^N] with the co-catalysts (Scheme 2, Fig. 1). ^{c} $\Delta G_P = \Delta G_{add} - \Delta G_{hyd}$ (−10.2 kcal mol^{-1} for all co-catalysts). ^{d} Experimental reaction conditions: 30 atm H$_2$, 5 μmol of [Fe^N] (0.07 mol%), (1.75 mol%) of each additive and 7 mmol of 4-formylmorpholine in 5 mL of THF at 100 °C for 2 h. TON and conv. were determined by GC-FID analysis of the products and remaining starting material. Each entry is the average of two or more trials.

The DFT calculations using DMF as a model substrate yielded optimal results for TBD (triazabicyclodecene) as a co-catalyst (Table 1, entry 1). The basic and rigid character of the guanidine scaffold provides a low proton transfer barrier ($\Delta G_{HT}^{\ddagger} = 21.3$ kcal mol^{-1}), facilitating the C–N bond cleavage of the hemiaminal intermediate. Additionally, TBD yielded a ΔG_{add} close to zero (−1.5 kcal mol^{-1}) and the second largest $\Delta G_{add} - \Delta G_{hyd}$ (8.7 kcal mol^{-1}), suggesting that the formation of the adduct does not compete with the hydrogenation of the amide. 1,2,3-Triphenylguanidine (entry 8) yielded a similar $\Delta G_{HT}^{\ddagger}$ barrier, but with a more negative ΔG_{add} value
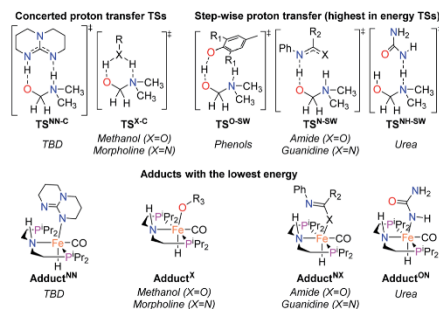
Fig. 1 TSs and adducts obtained from DFT calculations to compute the assisted proton transfer barrier ($\Delta G_{HT}^{\ddagger}$) and adduct formation free energy (ΔG_{add}) for the co-catalysts shown in Table 1.

(−9.3 kcal mol^{-1}), likely due to its lower basicity compared to TBD. Acetanilide (entry 2) also afforded promising results, in this case showing that replacement of H by Me in the originally reported formanilide co-catalyst (entry 3) changes $\Delta G_{add} - \Delta G_{hyd}$ from negative to positive, meaning lower competition of the adduct formation towards amide hydrogenation. Among single site hydrogen bond donors, phenols (entries 4–6) exhibited some promise as a proton shuttle, although sterically large substituents were required to alleviate formation of iron adducts (**Adduct^O**, Fig. 1). Interestingly, morpholine and urea yield the largest energy barrier of all of the co-catalysts (34.6 and 35.3 kcal mol^{-1}, respectively).[13] This result suggests that a purely basic co-catalyst, although beneficial to prevent adduct formation, does not assist with the hemiaminal proton transfer. Overall, the computational results indicate that the best co-catalysts are those which provide spatially separated hydrogen bond donor and acceptor sites which can act as push–pull proton shuttles, together with a basic character and/or steric bulky groups to prevent the formation of adducts.

The high co-catalytic activity predicted for TBD (entry 1) was further analyzed by performing microkinetic modelling[20–22] using the complex reaction network we previously found for amide hydrogenation (see ESI†).[13] Under the conditions typically used experimentally (1.4 M of DMF, 0.02 M of TBD, 1 mM of Fe^N and fixed concentration of 0.162 M of H$_2$, at 100 °C),[5] the microkinetic model yielded a high conversion of 27% over a short reaction time of 2 hours. This conversion is substantially higher than the conversion with formanilide as co-catalyst (12%). The same trend was observed by using 4-formylmorpholine as the substrate (see ESI†),[23] a benchmark tertiary amide used in our prior studies on Fe^N-catalyzed catalyzed deaminative hydrogenation. In this case, the conversions with TBD and formanilide were 56% and 46%, respectively.
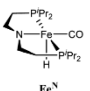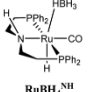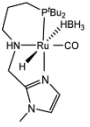
Experimental co-catalyst and catalyst testing

The computational predictions of co-catalyst efficacy were examined experimentally using 4-formylmorpholine (Table 1).

131

Each potential co-catalyst was tested in catalytic trials with a 1.75 mol% loading, along with 0.07 mol% **Fe^N** under previously optimized conditions.[5] Due to the high activity of the catalyst, the variable amount of time required to manipulate the pressure vessel between trials, and the need to equilibrate the vessel at the reaction temperature, it was not possible to acquire reliable initial rate measurements (conversions < 10%). Instead, reaction times were limited to 2 hours to minimize conversion and provide kinetically relevant comparisons. The reaction progress was monitored by amide conversion because of chromatographic issues in quantifying the morpholine product. However, no signals other than starting materials, morpholine and methanol were observed by GC-FID. As predicted by DFT, TBD proved a remarkable co-catalyst, affording a greater than two fold enhancement in TON (compare entries 1 and 9) over the short reaction time. Examination of the influence of TBD loading from 0 to 250 μmol (see ESI; Fig. S7†) indicated a strong correlation between TON and [TBD], saturating at approximately 200 μmol. The computational results also successfully predicted the relative ability of the other co-catalysts. For additives in which ΔG_P is positive, the best co-catalysts should be those which lower the $\Delta G_{HT}^{\ddagger}$ involved in the hemiaminal C–N bond cleavage, as illustrated in entries 1, 2, 6 and 7. In cases where iron deactivation is problematic due to a large negative ΔG_{add}, then the key barrier to amide hydrogenation is approximated by the total energy difference between $\Delta G_{add} - \Delta G_{hyd}$ and $\Delta G_{HT}^{\ddagger}$, which explains the superior performance of acetanilide over formanilide (entries 2 and 3). The only discernable variation from this trend is the unexpectedly poor performance of 1,2,3-triphenylguanidine (entry 8), which may react in a different manner as indicated by an immediate color change upon treatment with **Fe^N**. The use of urea in the reaction appeared to inhibit the reaction (lower conversion than without additive), which is likely due to other irreversible reactions with the iron species or difficulties in drying the very hydroscopic parent amide. Still, our rational co-catalyst design has led to the identification of a remarkably active catalytic system for selective amide hydrogenation.

The few homogenous transition metal catalysts reported for deaminative hydrogenation are all proposed to follow similar pathways (Scheme 1), with Noyori-type bifunctional mechanisms being prominent.[14,15] Given the importance of non-metal mediated hemiaminal cleavage in our computed mechanism, we hypothesized that the co-catalytic enhancements observed here with **Fe^N** should be generalizable to other systems. Indeed, highly active ruthenium catalysts recently reported by Beller and Sanford[24–26] also exhibit substantial enhancement in activity upon co-catalytic addition of TBD or formanilide (Table 2). The (^{Ph}PN^{H}P)Ru(H)(CO)(BH$_4$) (**RuBH$_4$^{NH}**) precatalyst (^{Ph}PN^{H}P = HN[CH$_2$CH$_2$(PPh$_2$)]$_2$) exhibited a near 4-fold increase in TON for 4-formylmorpholine hydrogenation over a short 2 hour reaction time in the presence of TBD, making it one of the most active systems for hydrogenation of this benchmark substrate. In this case, formanilide inhibits the reaction by forming a stable ruthenium adduct (Fig. S6†). In contrast, with the (PNN)Ru(H)(CO)(BH$_4$) (**Ru^{PNN}**) (PNN = 3-(di-*tert*-butylphosphino)-*N*-[(1-methyl-1*H*-imidazol-2-l)methyl]propylamine)

Table 2 Comparison of co-catalysts for amide hydrogenation with pincer supported group 8 catalysts[a]
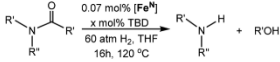
Catalyst	Co-catalyst	TON[b]	Conv.[b]
Fe^N	None	320	23%
	TBD	830	59%
	HCONHPh	630	45%
RuBH$_4$^{NH}	None	310	22%
	TBD	1200	86%
	HCONHPh	0[c]	0[c]
Ru^{PNN}	None	440	31%
	TBD	1170	84%
	HCONHPh	1040	74%
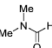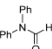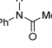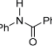
[a] Reaction conditions: 30 atm H$_2$, 5 μmol of [Fe or Ru] (0.07 mol%), 125 μmol of co-catalyst, and 7 mmol of 4-formylmorpholine in 5 mL of THF at 100 °C for 2 h. For [Ru] co-catalysts 10 μmol of NEt$_3$ was added to activate the catalyst. [b] Determined by GC-FID analysis of the products and remaining starting material. Each entry is the average of two or more trials. [c] Formanilide reacts irreversibly with this Ru catalyst to form an adduct, see ESI for details.

precatalyst, the relative difference in performance between TBD and formanilide is not as large, likely because the steric bulk of the *tert*-butyl substituents on the phosphine donors lowers the stability of a formanilide adduct.

The co-catalytic effect of TBD with **Fe^N** across different classes of amides was also investigated experimentally (Table 3). Examples of dialkyl and diaryl formamides (entries 1 and 2) exhibited significant enhancement in TON in the presence of TBD compared to the reaction without co-catalyst. *N*-Phenylacetamide (entry 3), a substrate that previously proved challenging for **Fe^N**, was also hydrogenated with greater productivity in the presence of TBD. However, no enhancement was observed upon TBD treatment of the corresponding benzamide (entry 4). This may be due to steric limitation at the carbonyl moiety created by the larger phenyl substituent. In this case, substituting TBD for a smaller co-catalyst provided a modest increase in TON. These results suggest the co-catalytic effect of TBD and related shuttles may be effective with more diverse amides. Admittedly, the enhancement observed with diphenylformanilide was initially unexpected because a mechanism involving the iron-catalyst instead of formanilide, was previously proposed for the hemiaminal C–N bond cleavage using aryl amide substrates.[13] However, the calculated $\Delta G_{HT}^{\ddagger}$ using the

132

Table 3 Co-catalytic enhancement of amide hydrogenations using TBD[a]

Entry	Substrate	[TBD]	TON[b]
1		0	50
		1.75	300
2		0	1150
		0.45	5180
3		0	140
		1.75	230
4		0	120
		1.75	120
		1.75[c]	250[c]

[a] Reaction conditions: 60 atm H_2, 5 μmol of [Fe] (0.07 mol%), x μmol of TBD, and 7 mmol of substrate in 5 mL of THF at 120 °C for 16 h. [b] TON was determined by GC-FID and NMR analysis of the products and remaining starting material. Each entry is the average of three or more trials. [c] TBD was substituted by N-phenylacetamide (Table 1; entry 2).
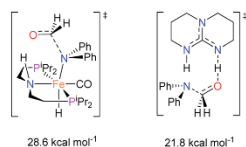
Fig. 2 Gibbs energies associated with the C–N bond cleavage TSs for diphenylformamide assisted by Fe^N and the TBD co-catalyst.

diphenylformanilide hemianimal intermediate and TBD is lower ($\Delta G^\ddagger = 21.8$ kcal mol^{-1}) than the barrier for the iron-assisted mechanism ($\Delta G^\ddagger = 28.6$ kcal mol^{-1}, see Fig. 2). This result is in agreement with the enhanced reactivity observed for the hydrogenation of diphenylformanilide using TBD as co-catalyst (see Fig. 2).

Conclusions

In conclusion, this work establishes the basis for co-catalyst optimization in amide deaminative hydrogenation reactions using Noyori-type catalysts. Key factors in the co-catalyst design include a push–pull motif of hydrogen bonding sites to assist the C–N bond cleavage of the hemiaminal and controlled acidity and steric hindrance to prevent catalyst poisoning. Notably, these design principles yielded co-catalysts enhancing the activity of systems based on different transition metals. The generality of the co-catalyst effect and its mechanistic

understanding provide new opportunities for the catalytic hydrogenation of challenging electron-rich carbonyl compounds.

Conflicts of interest

There are no conflicts to declare.

Acknowledgements

Notes and references

1 J. Magano and J. R. Dunetz, *Org. Process Res. Dev.*, 2012, **16**, 1156–1184.

2 G. Zhang and S. K. Hanson, *Chem. Commun.*, 2013, **49**, 10151–10153.

3 G. Zhang, B. L. Scott and S. K. Hanson, *Angew. Chem., Int. Ed.*, 2012, **51**, 12102–12106.

4 A. M. Smith and R. Whyman, *Chem. Rev.*, 2014, **114**, 5477–5510.

5 U. Jayarathne, Y. Zhang, N. Hazari and W. H. Bernskoetter, *Organometallics*, 2017, **36**, 409–416.

6 G. Arthur, *The Amide Linkage: Selected Structural Aspects in Chemistry, Biochemistry, and Materials Science*, Wiley-Interscience, Hoboken, 1st edn, 2000.

7 S. Kar, A. Goeppert, J. Kothandaraman and G. K. S. Prakash, *ACS Catal.*, 2017, **7**, 6347–6351.

8 D. G. Gusev, *ACS Catal.*, 2017, **7**, 6656–6662.

9 E. Balaraman, B. Gnanaprakasam, L. J. W. Shimon and D. Milstein, *J. Am. Chem. Soc.*, 2010, **132**, 16756–16758.

10 J. M. John and S. H. Bergens, *Angew. Chem., Int. Ed.*, 2011, **50**, 10377–10380.

11 M. Beller, W. Baumann, E. Alberico, H.-J. J. Drexler, J. R. Cabrero-Antonino, H. Junge, K. Junge, E. Alberico, H.-J. J. Drexler, W. Baumann, K. Junge, H. Junge and M. Beller, *ACS Catal.*, 2016, **6**, 47–54.

12 J. A. Garg, S. Chakraborty, Y. Ben-David and D. Milstein, *Chem. Commun.*, 2016, **52**, 5285–5288.

13 L. Artús Suàrez, Z. Culakova, D. Balcells, W. H. Bernskoetter, O. Eisenstein, K. I. K. I. Goldberg, N. Hazari, M. Tilset and A. Nova, *ACS Catal.*, 2018, **8**, 8751–8762.

14 P. A. Dub and J. C. Gordon, *Nat. Rev. Chem.*, 2018, **2**, 396–408.

15 L. Alig, M. Fritz and S. Schneider, *Chem. Rev.*, 2018, **119**, 2681–2751.

16 S. Kar, J. Kothandaraman, A. Goeppert and G. K. S. Prakash, *J. CO₂ Util.*, 2018, **23**, 212–218.

17 C. Tang, K. Sordakis, H. Junge, M. Beller, L. K. Vogt, G. Laurenczy and P. J. Dyson, *Chem. Rev.*, 2017, **118**, 372–433.

133

18 A. Wakatsuki, Y. Kabe, M. Matsumoto, N. Watanabe and H. K. Ijuin, *Tetrahedron Lett.*, 2018, **59**, 971–977.

19 B. Yuan, R. He, W. Shen, Y. Xu, X. Liu and M. Li, *ChemistrySelect*, 2016, **1**, 2971–2978.

20 The microkinetic model was performed using COPASI 4.22 software.

21 S. Hoops, R. Gauges, C. Lee, J. Pahle, N. Simus, M. Singhal, L. Xu, P. Mendes and U. Kummer, *Bioinformatics*, 2006, **22**, 3067–3074.

22 M. Besora and F. Maseras, *Wiley Interdiscip. Rev.: Comput. Mol. Sci.*, 2018, **1372**, 1–13.

23 Microkinetic models show that 4-formylmorpholine reacts in a similar manner than DMF (see ESI†).

24 C. Bornschein, K. P. J. Gustafson, O. Verho, M. Beller and J. E. Bäckvall, *Chem.–Eur. J.*, 2016, **22**, 11583–11586.

25 R. Adam, E. Alberico, W. Baumann, H. J. Drexler, R. Jackstell, H. Junge and M. Beller, *Chem.–Eur. J.*, 2016, **22**, 4991–5002.

26 N. M. Rezayee, C. A. Huff and M. S. Sanford, *J. Am. Chem. Soc.*, 2015, **137**, 1028–1031.

134

Electronic Supplementary Information

Rational Selection of Co-Catalysts for the Deaminative Hydrogenation of Amides

Lluís Artús Suàrez, Upul Jayarathne, David Balcells, Wesley Bernskoetter,* Nilay Hazari, Martín Jaraiz, Ainara Nova*

Table of Contents:

Experimental Details

All manipulations were carried out using standard vacuum, Schlenk line, canula or glovebox techniques. Hydrogen was purchased from Airgas and used as received. The catalysts **Fe^N** and **Ru^PNN** were prepared as previously described.[1,2] All other chemicals including **RuBH4^NH** were purchased from Aldrich, Fisher, VWR, Strem or Cambridge Isotope Laboratories. Amide substrates and additives were purified by sublimation and distillation or vacuum transfer after drying over appropriate drying agents.[3] All other non-volatile solids were dried under vacuum at 50 °C. Solvents were dried and deoxygenated using literature procedures.[3] ^{1}H, ^{13}C and ^{31}P NMR spectra were recorded on Bruker 300 MHz DRX, 500 MHz DRX or 600 MHz spectrometers at ambient temperature, unless otherwise noted. ^{1}H and ^{13}C chemical shifts are referenced to residual solvent signals; ^{31}P chemical shifts are referenced to an external standard of H_3PO_4. Probe temperatures were calibrated using ethylene glycol and methanol as previously described.[4] High pressure catalytic hydrogenation reactions were performed using a Parr 5500 series compact reactor with glass insert.

General procedure and sample spectra for screening the co-catalytic effect

Inside a glovebox, the catalyst (5 μmol) was added as a solution to a glass reactor liner (50 mL). Then amide (7 mmol) and 5 mL of THF were added in succession using a micro syringe. Subsequently, the relevant additive (25 μmol) was added and the Parr reactor sealed and removed from the glovebox. The reactor was pressurized with Commercial grade hydrogen at ambient temperature (450 psi) and heated (100 °C) with mechanical stirring. After 2h heating was stopped, and the reactor was immediately immersed in to a cold ice bath and the H_2 was slowly vented. The products and the remaining reactants were analysed by ^{1}H NMR spectroscopy or GC FID using mesitylene as an internal standard. GC Method: 0.418 mL of mesitylene was added to the reaction solution and the final volume was adjusted to 10 mL by adding THF. An aliquot of 0.02 mL from this mixture was diluted to 0.2 mL and analyzed using a Thermo Fisher GC (Trace 1300; Column – TG 5MS AMINE 30m x 0.25 mm x 0.25 μm; start at 40 °C, ramp 25 °C. hold 2 min). Response factors were calculated using standards. NMR Method: The reaction solution was diluted either to 10 mL or 9 mL. An aliquot of 0.1 mL was mixed with 0.05 mL of 1M mesitylene to prepare the NMR sample.
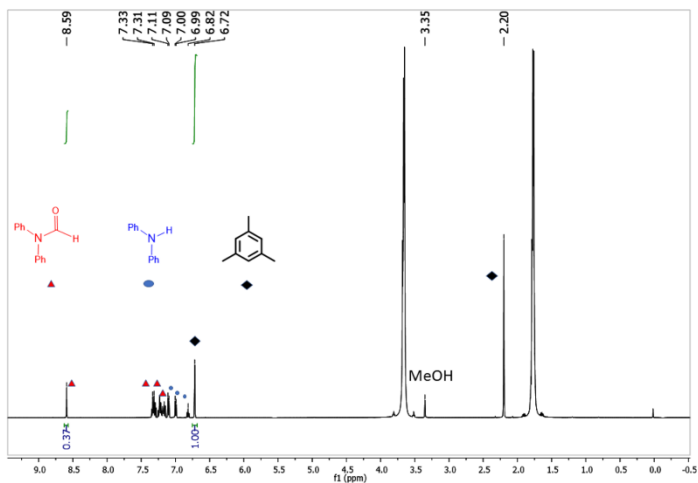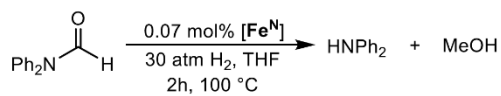
Figure S1: Sample ^{1}H NMR spectrum of product solution from hydrogenation of diphenylformamide using **Fe^N** with no additives. The labelled peaks identfy the species present. Two large solvent peaks for residual THF are also observed.
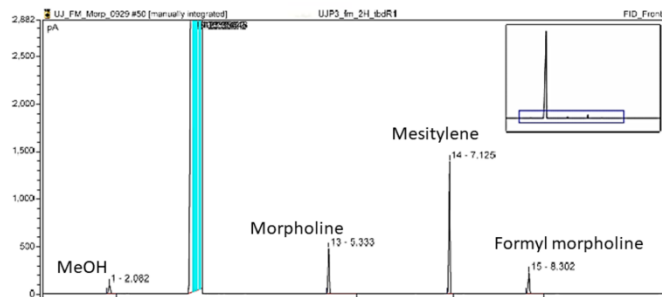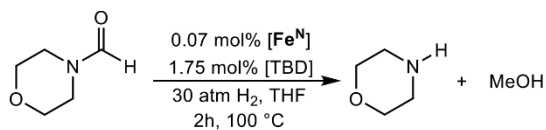
Figure S2: Sample GC-FID chromatogram of product solution from the hydrogenation of formylmorpholine formamide using **Fe^N** in the presence of TBD. The labelled peaks identfy the species present along with the off scale solvent signal.

Synthesis of (^{Ph}PN^{H}P)RuH(CO)(HCONPh)

Inside the glovebox, a sample of **RuBH₄^{NH}** (0.023 g, 0.039 mmol) was transferred to a J-Young tube using 1 mL of THF. Then a solution of NEt₃ in THF (1M, 0.117 mL, 0.117 mmol) was added to the reaction mixture, followed by HCONHPh in THF (1M, 0.043 mL, 0.043 mmol). A drop of deuterated benzene was added, and the tube was tightly closed before it was removed from the glovebox. This mixture was heated at 50 °C and the reaction monitored using ^{31}P NMR spectroscopy until it reached completion. After that, the tube was taken back in to the glovebox and all the volatiles were evaporated under reduced pressure. A near colorless solid was obtained and crystals suitable for X-ray diffraction were obtained by slow diffusion of pentane into a concentrated THF solution of the product. Yield: 0.013 g (40 %). ^{1}H NMR (THF-d_8; 50 MHz, 23 °C) (two isomers observed): major isomer: 10.98 (s, 1H, N-*H*), 8.02 (s, 1H, *H*CO, overlap with *Ph*H), 8.02(s, 4H, *Ph*H), 7.41(m 10H, *Ph*H), 7.32(s,br 1H, *Ph*H), 7.26-7.22(q,t, 6H, *Ph*H), 6.43(m 2H, *Ph*H), 5.55(d, 2H, *Ph*H), 3.35 (m, 2H, C*H₂*), 3.02 (t, 2H, C*H₂*), 2.87 (d, 2H, C*H₂*), 2.16 (m, 2H, C*H₂*), -14.24 (t, 1H, Fe-H); ^{31}P{^{1}H} NMR (THF-d_8): 58.955; ^{13}C{^{1}H} NMR (THF-d_8): δ 174.07 (s, *H*CO), 137.69-137.43 (m, *Ph*H), 135.14 (s, *Ph*H), 132.39 (s, *Ph*H), 130.67 (s, *Ph*H), 129.47-128.75 (m, *Ph*H), 127.22 (s, *Ph*H), 125.67 (s, *Ph*H), 121.34 (s, *Ph*H), 52.17 (t, C*H₂*), 32.89 (t, C*H₂*).
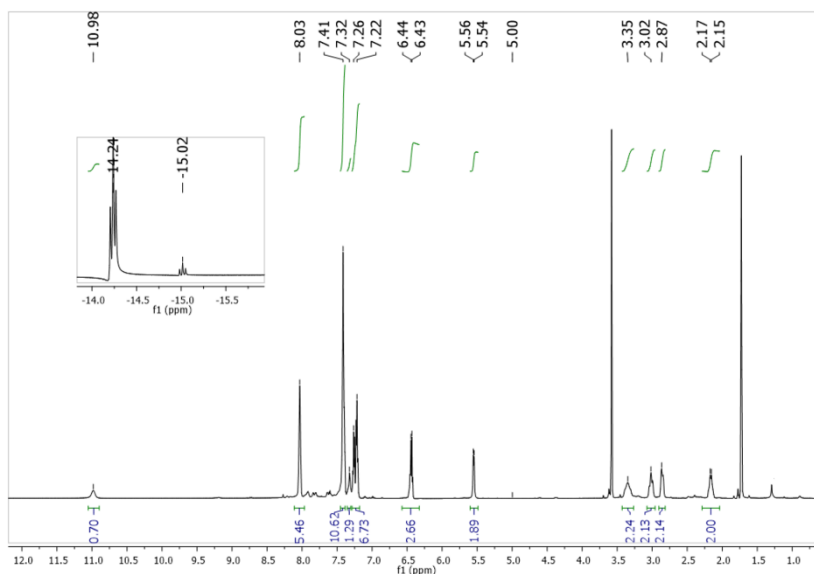
Figure S3: ^{1}H NMR of (^{Ph}PN^{H}P)RuH(CO)(HCONPh) (two isomers observed) in THF-d_8.
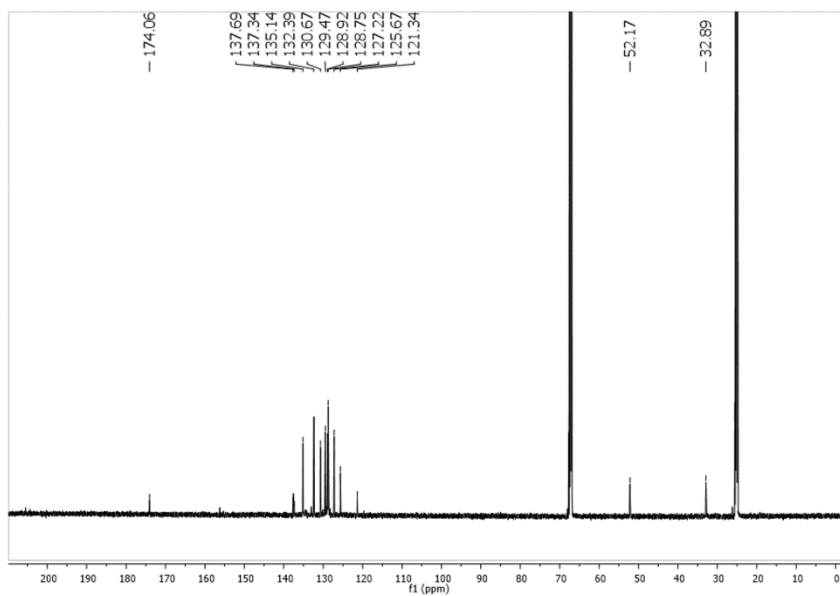
Figure S4: $^{13}C\{^1H\}$ NMR of ($^{Ph}PN^HP$)RuH(CO)(HCONPh) in THF-d_8.
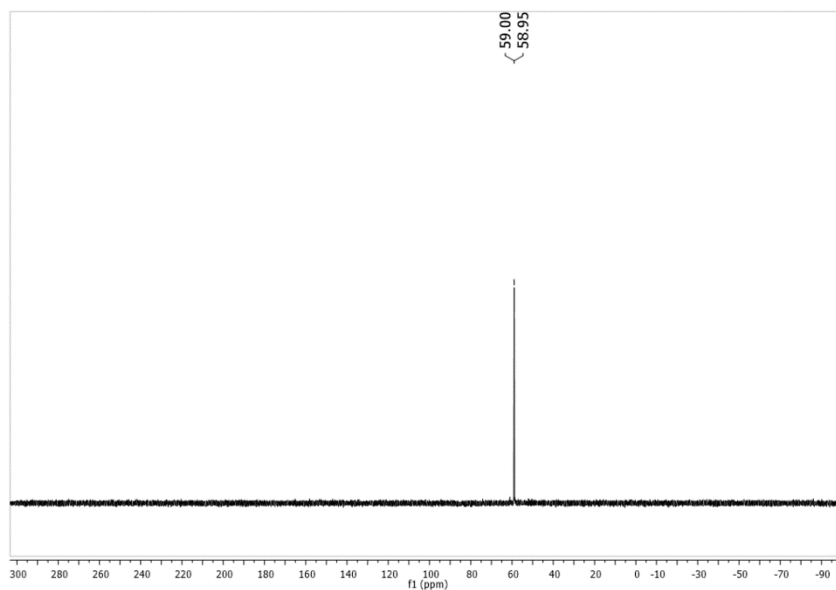
Figure S5: $^{31}P\{^1H\}$ NMR of ($^{Ph}PN^HP$)RuH(CO)(HCONPh) (two isomers observed) in THF-d_8.
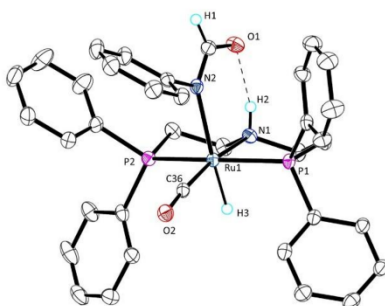
Figure S6: Molecular structure of ($^{Ph}PN^HP$)RuH(CO)(HCONPh) with thermal ellipsoids at 50% probability. Hydrogen atoms and an additional formanilide molecule, co-crystalized with the complex, have been removed for clarity. Selected bond lengths (Å) and angles (deg): Ru(1)−N(2) 2.236(2), Ru(1)−P(2) 2.3082(8), Ru(1)−P(1) 2.3203(8), Ru(1)−N(1) 1.195 (2); P(1)−Ru(1)−P(2) 163.64(3), N(2)−Ru(1)−N(1) 93.01 (9).

Comparative influence of base activator and co-catalysts

Table S1 distinguished the possible roles of the co-catalyst in promoting C−N scission and acting as a base activator. Entries 1 and 2 suggest that TBD can work as an activator, presumably by scavenging BH_3 from ($^{Ph}PN^HP$)RuH(CO)(BH_4). Significantly, comparison of the entries 2, 4, 5 and 6 suggest that the effect of a base catalyst activator saturates at 2 eq per metal and that the influence of TBD as a co-catlayst for C−N bond scission far exceeds any potential influence from acting as a simple catalyst activator.

Table S1: Influence of base activator and co-catalysts on 4-formylmorpholine hydrogenation using ($^{Ph}PN^HP$)RuH(CO)(BH_4).[a]
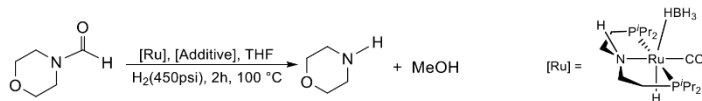
Entry	NEt$_3$	TBD	HCONHPh	2,6-diisopropyl-4-methylphenol	TON[b] (Con %)
1	2 eq	25 eq	-------	-------	1200 (86%)
2	-------	25 eq	-------	-------	1040 (74%)
3	2 eq	-------	-------	25 eq	822 (59%)
4	2 eq	-------	-------	-------	310 (22%)
5	25 eq	-------	-------	-------	290 (21%)
6	-------	-------	-------	-------	210 (15%)
7	2 eq	-------	25 eq	-------	NR (0%)

[a] Reaction conditions: 30 atm H$_2$(~ 450 psi), 5 *μmol* of [Ru] (0.018 mol %), 125 *μmol* of each additive, 10 or 125 *μmol* of NEt$_3$ and 7 mmol of formyl morpholine in 5 mL of THF at 100 °C for 2h. [b] Determined using GC-FID analysis of the products and remaining starting material. Each entry is average of two or more trials.

Discussion of aldehyde hydrogenation

The microkinetic modeling of the catalytic reaction suggests that the intermediate aldehyde is hydrogenated rapidly under the reaction conditions and plays little or no role in the reaction rate (See Reaction 4; Table S2). In the case of formylmorpholine hydrogenation, the intermediate aldehyde is formaldehyde. Given the difficulty in obtaining dry formaldehyde in a non-polymer form we have substituted benzaldehyde for a comparison of the hydrogenation of aldehydes and formamides. Using 0.07mol% of Fe^N, 100 °C, and 30 atm H_2 in THF, both formylmorpholine and benzaldhyde are hydrogenated to nearly full conversion (>96%). However, although both reactions give high conversion, the uptake of hydrogen gas is noticeably different. The benzaldhyde reaction ceased uptake of hydrogen after *ca* 30 mintues while formylmorphline continued to consume hydrogen for *ca* 90 minutes. While these observations are insufficient to establish reliable rate meaasurements they confirm the computational conclusions that aldehyde hydrogenation is a viable intermediate step in catalysis and that it is facile relative to formamide hydrogenation.

Influence of [TBD] on Catlaysis
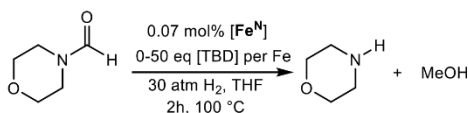
Entry	TBD	TON
1	0 eq	320
2	5eq	515
3	10eq	650
4	25eq	830
5	50 eq	965
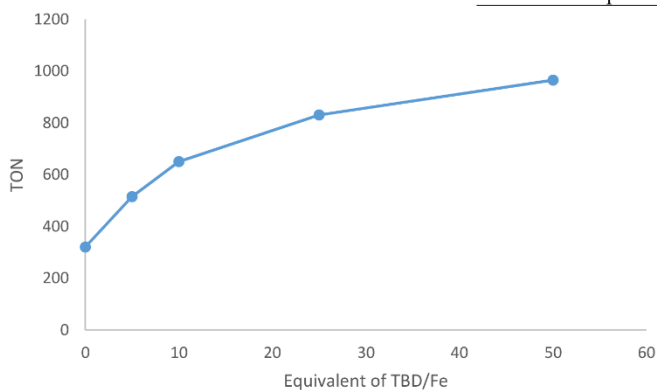
Figure S7: Correlation between TBD loading and TON for formylmorpholine hydrogenation. Experimental conditions: 30 atm H_2(~ 450 psi), 5 *μmol* of [Fe^N] (0.07 mol %), 0-250 *μmol* of TBD, and 7 mmol of formyl morpholine in 5 mL of THF at 100 °C for 2h. TON determined using GC-FID analysis of the products and remaining starting material. Each point is average of two or more trials.

Computational Details

DFT calculations were carried out with the Gaussian09 software package.[5] The hybrid meta-GGA M06[6] functional was selected on the basis of geometry and energy benchmarks.[7] Structures were fully optimized without any geometry or symmetry constraints, combining the double-z LANL2DZ (on Fe and Ru, including relativistic effects)[8,9] and 6-31+G** (on all other elements)[10,11] basis sets. Vibrational frequencies were computed at the same level of theory to classify all stationary points as either saddle points (transition states, with a single imaginary frequency) or energy minima (reactants, intermediates and products, with only real frequencies). These calculations were also used to obtain the thermochemistry corrections (zero-point, thermal and entropy energies) at the experimental p = 30 atm and T = 373 K conditions. The energy of the optimized geometries was refined by single point calculations with triple-z quality basis sets, including the LANL2TZ[8,9] on Fe and the 6-311+G** on all other elements.[12] The energies reported in the text were obtained by adding the thermochemistry corrections to the refined potential energies. The solvation effects of THF were included in both the geometry optimizations and energy refinements using the continuum SMD model.[13] The ultrafine (99,590) grid was used in all calculations to increase numerical accuracy and to facilitate convergence. Microkinetic models were carried out with the COPASI 4.22 software.[14] A data set collection of input files and computational results is available in the ioChem-BD repository[15] and can be accessed online via https://dx.doi.org/10.19061/iochem-bd-6-14.

The mechanism proposed in Scheme 2 is the result of a thorough mechanistic investigation of the deaminative hydrogenation of DMF by Fe^N.[7] In this study several mechanisms proposed for the hydrogenation of esters were investigated with fomanilide and DMF. The conclusion of this study was that the mechanism for the hemiaminal C–N bond protonolysis (Step 2 in Scheme 1) depends on the substrate (formanilide or DMF) and the presence of reagents able to assist the proton transfer. In the case of DMF, formanilide could act as a co-catalyst to assist in protonolysis. In contrast, when formanilide is the reactant, the protonolysis is assisted by Fe^N. This difference originates from the basicity of the –NMe2 group in DMF, which deprotonates formanilide, while NPhH is difficult to protonate but can form an imido intermediate with the Fe-catalyst.

Microkinetic models:

Microkinetic models were constructed to: (1) predict catalytic activity upon using TBD as co-catalyst instead of formanilide, with (^{iPr}PNP)Fe(H)(CO) (**Fe^N**) and DMF, and (2) account for the experimental conversions observed with 4-formylmorpholine as substrate.

Microkinetic models were constructed with the COPASI software[14] (version 4.22). Association reactions were assumed to have low energy barriers ($\Delta G^{\ddagger} \leq 5$ kcal mol^{-1}), and thus have no impact on the global kinetics of the reaction. The initial concentrations used in the simulations were those reported in the corresponding experiments[16] (1.4 M of amide, 1mM of catalyst, 0.162 M of hydrogen and 25 mM of co-catalyst). The concentration of hydrogen was kept constant, in line with the effectively constant pressure of hydrogen used in the reactor (30 atm). H$_2$ concentration was approximated using the molar fraction of H$_2$ in a saturated solution of H$_2$ in THF at 33.4 atm and 100 ºC (0.01461 H$_2$ mol / solution mol) asuming incompresibility of THF and that [H$_2$] << [THF].[17] As in the experiments, simulations were carried out for a total time of 2 hours at T = 373 K. The models were based on deterministic time course simulations with the LSODA algorithm.[18]

1) DMF with formanilide and TBD as co-catalysts

The DMF conversion *vs* time traces using **Fe^N** and formanilide or TBD as co-catalysts were obtained by running a microkinetic model based on the mechanism reported in our previous work[7] (Figure S8). The elementary steps of the mechanism underlying the microkinetic model are given in Figure S9, together with the $\Delta G^{\ddagger}$ values derived from the DFT calculations published in our previous work[7] and presented in Table S2. This model predicts conversions of 12 and 27% for the formanilide and TBD-assisted reactions respectively. The formation of the 1,2-addition adduct with between **Fe^N** and the product MeOH (reaction 11) was included in the microkinetic moldel to evaluate the influence of this reaction on DMF conversion. However, the % conversion with and without this reaction were the same, suggesting that the adduct formation with MeOH is not relevant in this process.

DMF conversion

Conversion (%) / Time (h)

— Assisted by formanilide   — Assisted with tbd
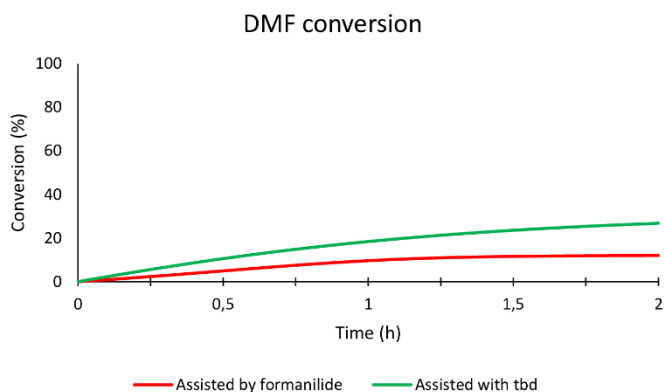
Figure S8: Microkinetic simulations of assisted DMF deaminative hydrogenation.

Reaction 1: $FeH^{NH} + DMF \rightleftharpoons Fe^{NH}DMFH$

Reaction 2: $Fe^{NH}DMFH \rightleftharpoons Hemiaminal^{DMF} + Fe^{N}$

Reaction 3: $Hemiaminal^{DMF} + Formanilide \rightleftharpoons Dimethylamine + Formaldehyde + Formanilide$

Reaction 4: $Formaldehyde + FeH^{NH} \rightleftharpoons Methanol + Fe^{N}$

Reaction 5: $Fe^{N} + Formanilide \rightleftharpoons Adduct^{Formanilide}$

Reaction 6: $Fe^{N} + H_2 + Formanilide \rightleftharpoons FeH^{NH} + Formanilide$

Reaction 7: $Fe^{N} + H_2 \rightleftharpoons FeH^{NH}$

Reaction 8: $Formanilide + FeH^{NH} \rightleftharpoons Aniline + Formaldehyde + Fe^{N}$

Reaction 9: $Hemiaminal^{DMF} + TBD \rightleftharpoons Dimethylamine + Formaldehyde + TBD$

Reaction 10: $Fe^{N} + TBD \rightleftharpoons Adduct^{TBD}$

Reaction 11: $Fe^{N} + Methanol \rightleftharpoons Adduct^{Methanol}$

Figure S9: Implemented reactions in the DMF microkinetic simulations.

144

	$\Delta G^{\ddagger}$ Forward (kcal mol^{-1})	$\Delta G^{\ddagger}$ Backwards (kcal mol^{-1})
Reaction 1	23.1	0.6
Reaction 2	0.9	2.8
Reaction 3	13.5	10.3
Reaction 4	6.0	11.1
Reaction 5	4.0	16.2
Reaction 6	4.0	14.2
Reaction 7	11.6	21.8
Reaction 8	21.9	6.5
Reaction 9	13.5	10.3
Reaction 10	4.0	5.4
Reaction 11	5.0	11.9

Table S2: Reactions and corresponding Gibbs energies (kcal mol^{-1}) used in the microkinetic model of the deaminative hydrogenation of DMF.

2) 4-formylmorpholine with formanilide and TBD as co-catalyst

The conversions of 4-formylmorpholine *vs* time catalyzed by **Fe^{N}** and using formanilide and TBD as co-catalysts (Figure S10), were obtained by running the microkinetic model shown in Figure S6. In this case, the energies of reactions 1, 2, 3 and 9 were replaced by reactions 12, 13, 14 and 15 (Figure S11), in which 4-formylmorpholine is used instead of DMF (see Table S3). This model predicts conversions of 46 and 56% for the formanilide and TBD-assisted reactions respectively. Experimental conversions of 4-formylmorpholine hydrogenation with 25 eq of formanilide or TBD as co-catalyst could be fitted by correcting the energy of methanol by $\pm$ 0.2 kcal mol^{-1}. The similar energies obtained for the reactions 1, 2, 3 and 9 using DMF and 11, 12, 13 and 14 using morpholidine indicate that the same mechanism is expected for the two substrates.
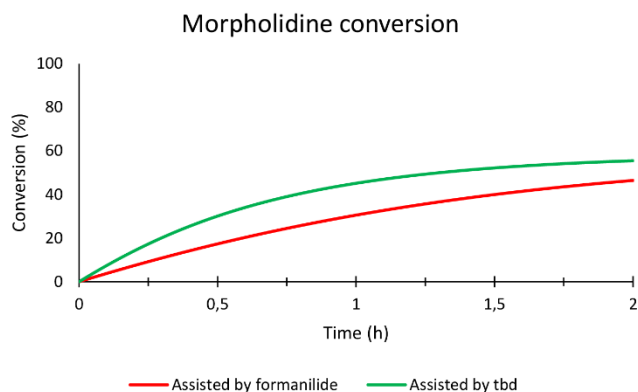
Figure S10: Microkinetic simulations of assisted 4-formylforpholine deaminative hydrogenation

Reaction 12: FeH^{NH} + Morpholidine ⇌ $\text{Fe}^{\text{NH}}\text{MorpholidineH}$

Reaction 13: $\text{Fe}^{\text{NH}}\text{MorpholidineH}$ ⇌ Hemiaminal$^{\text{Morpholidine}}$ + Fe^{N}

Reaction 14:   Hemiaminal$^{\text{Morpholidine}}$ + Formanilide ⇌ Morpholine + Formaldehyde + Formanilide

Reaction 15:   Hemiaminal$^{\text{Morpholidine}}$ + TBD ⇌ Morpholine + Formaldehyde + TBD
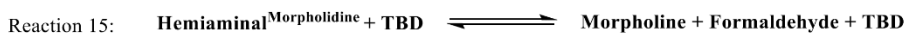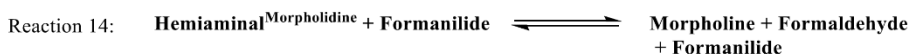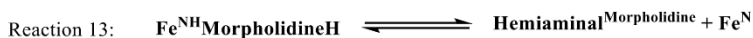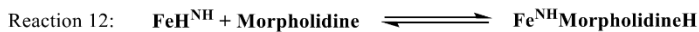
Figure S11: Reactions used together with 4, 5, 6, 7, 8, 10 and 11 to perform the 4-formylmorpholine microkinetic simulations.

	$\Delta G^{\ddagger}$ Forward (kcal mol^{-1})	$\Delta G^{\ddagger}$ Backwards (kcal mol^{-1})
Reaction 12	22.5	1.5
Reaction 13	0.5	2.5
Reaction 14	14.6	11.0
Reaction 15	14.6	11.0

Table S3: Reactions and corresponding Gibbs energies (kcal mol^{-1}) used in the microkinetic model of the deaminative hydrogenation of DMF.

Gibbs energies of organic reaction intermediates

The formation of hemiaminal and formaldehyde intermediates from DMF and 4-formylmorpholine is endergonic in both cases by ca 10 kcal/mol (see Figure S12). Therefore their concentration in solution is expected to be very low (eg: 0.1 μM of hemiaminal according to the microkinetic model). This may explain why these species are not observed in the crude ^{1}H NMR spectrum.

		Step 1: Amide C=O Hydrogenation	Step 2: C-N bond protonolysis	Step 3: Formaldehyde C=O Hydrogenation
	amide	hemiaminal	formaldehyde	methanol
DMF	0.0	10.5	13.8	-1.5
Morpholidine	0.0	8.8	12.4	-2.8
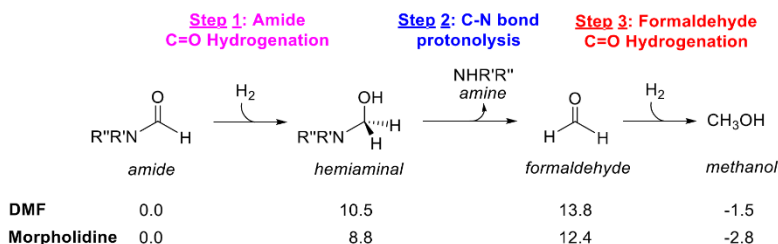
Figure S12: Gibbs energies (in kcal mol^{-1}) for the hydrogenation of DMF (R' = Me, R'' = Me) and morpholidine (R'R'' = O(CH$_2$)$_4$) to amines and methanol calculated in THF solvent (SMD) at 30 atm and 373 K.

Amide influence on $\Delta G_{HT}^{\ddagger}$

The $\Delta G^{\ddagger}_{HT}$ barriers obtained for DMF and 4-formylmorpholine using different co-catalysts were computed to determine the influence of the substrate. As shown in Table S4, similar values were obtained for the three co-catalysts, indicating that DMF can be used as a model for morpholine.

$\Delta G^{\ddagger}_{HT}$ (kcal mol^{-1})	TBD	Triphenylguanidine	Methanol
DMF	21.3	22.3	29.6
4-Formylmorpholine	22.6	21.4	28.1

$\Delta G^{\ddagger}_{HT}$	N-methylformanilide	Formanilide
DMF	25.3	22.6
4-Formylmorpholine	25.4	21.7

Table S4: Comparison between DMF and 4-formylmorpholine of $\Delta G_{HT}^{\ddagger}$ (kcal mol^{-1}).

References

1 E. A. Bielinski, P. O. Lagaditis, Y. Zhang, B. Q. Mercado, C. Würtele, W. H. Bernskoetter, N. Hazari and S. Schneider, *J. Am. Chem. Soc.*, 2014, **136**, 10234–10237.

2 M. Beller, W. Baumann, E. Alberico, H.-J. J. Drexler, J. R. Cabrero-Antonino, H. Junge, K. Junge, E. Alberico, H.-J. J. Drexler, W. Baumann, K. Junge, H. Junge and M. Beller, *ACS Catal.*, 2016, **6**, 47–54.

3 M. A. Giardello, R. K. Rosen, R. H. Grubbs, F. J. Timmers and A. B. Pangborn, *Organometallics*, 2002, **15**, 1518–1520.

4 J. Sandström, *Dynamic NMR Spectroscopy*, Academic Press, New York, 1982.

5 Gaussian 09, Revision D.01, M. J. Frisch, G. W. Trucks, H. B. Schlegel, G. E. Scuseria, M. A. Robb, J. R. Cheeseman, G. Scalmani, V. Barone, B. Mennucci, G. A. Petersson, H. Nakatsuji, M. Caricato, X. Li, H. P. Hratchian, A. F. Izmaylov, J. Bloino, G. Zheng, J. L. Sonnenberg, M. Hada, M. Ehara, K. Toyota, R. Fukuda, J. Hasegawa, M. Ishida, T. Nakajima, Y. Honda, O. Kitao, H. Nakai, T. Vreven, J. A. Montgomery, Jr., J. E. Peralta, F. Ogliaro, M. Bearpark, J. J. Heyd, E. Brothers, K. N. Kudin, V. N. Staroverov, T. Keith, R. Kobayashi, J. Normand, K. Raghavachari, A. Rendell, J. C. Burant, S. S. Iyengar, J. Tomasi, M. Cossi, N. Rega, J. M. Millam, M. Klene, J. E. Knox, J. B. Cross, V. Bakken, C. Adamo, J. Jaramillo, R. Gomperts, R. E. Stratmann, O. Yazyev, A. J. Austin, R. Cammi, C. Pomelli, J. W. Ochterski, R. L. Martin, K. Morokuma, V. G. Zakrzewski, G. A. Voth, P. Salvador, J. J. Dannenberg, S. Dapprich, A. D. Daniels, O. Farkas, J. B. Foresman, J. V. Ortiz, J. Cioslowski, and D. J. Fox, Gaussian, Inc., Wallingford CT, 2013., .

6 Y. Zhao and D. G. Truhlar, *Theor. Chem. Acc.*, 2008, **120**, 215–241.

7 L. Artús Suàrez, Z. Culakova, D. Balcells, W. H. Bernskoetter, O. Eisenstein, K. I. Goldberg, N. Hazari, M. Tilset and A. Nova, *ACS Catal.*, 2018, **8**, 8751–8762.

8 P. J. Hay and W. R. Wadt, *J. Chem. Phys.*, 1985, **82**, 270–283.

9 W. R. Wadt and P. J. Hay, *J. Chem. Phys.*, 1985, **82**, 284–298.

10 W. J. Hehre, R. Ditchfield and J. A. Pople, *J. Chem. Phys.*, 1972, **56**, 2257–2261.

11 W. Kohn, A. D. Becke and R. G. Parr, *J. Phys. Chem.*, 1996, **1**, 12974–12980.

12 A. D. McLean and G. S. Chandler, *J. Chem. Phys.*, 1980, **72**, 5639–5648.

13 A. V. Marenich, C. J. Cramer and D. G. Truhlar, *J. Phys. Chem. B*, 2009, **113**, 6378–6396.

14 S. Hoops, R. Gauges, C. Lee, J. Pahle, N. Simus, M. Singhal, L. Xu, P. Mendes and U. Kummer, *Bioinformatics*, 2006, **22**, 3067–3074.

15 M. Álvarez-Moreno, C. De Graaf, N. López, F. Maseras, J. M. Poblet and C. Bo, *J. Chem. Inf. Model.*, 2015, **55**, 95–103.

16 U. Jayarathne, Y. Zhang, N. Hazari and W. H. Bernskoetter, *Organometallics*, 2017, **36**, 409–416.

17 E. Brunner, *J. Chem. Eng. Data*, 1985, **30**, 269–273.

18 L. Petzold, *SIAM J Sci Stat Comput*, 1983, **4**, 136–148.

Paper III

EDGE ARTICLE

Check for updates

Highly selective hydrogenation of amides catalysed by a molybdenum pincer complex: scope and mechanism†

Thomas Leischner,[a] Lluis Artús Suarez, [b] Anke Spannenberg,[a] Kathrin Junge,[a] Ainara Nova [*b] and Matthias Beller [*a]

A series of molybdenum pincer complexes has been shown for the first time to be active in the catalytic hydrogenation of amides. Among the tested catalysts, **Mo-1a** proved to be particularly well suited for the selective C–N hydrogenolysis of *N*-methylated formanilides. Notably, high chemoselectivity was observed in the presence of certain reducible groups including even other amides. The general catalytic performance as well as selectivity issues could be rationalized taking an anionic Mo(0) as the active species. The interplay between the amide C=O reduction and the catalyst poisoning by primary amides accounts for the selective hydrogenation of *N*-methylated formanilides. The catalyst resting state was found to be a Mo–alkoxo complex formed by reaction with the alcohol product. This species plays two opposed roles – it facilitates the protolytic cleavage of the C–N bond but it encumbers the activation of hydrogen.

Introduction

The reduction of carboxylic acid derivatives *via* catalytic homogeneous hydrogenation represents an attractive atom-economic and environmentally benign methodology.[1,2] To date, the vast majority of homogeneous catalysts for these transformations rely on noble metals.[3] The limited availability of these elements along with their toxicity and pollutive nature initiated efforts for their replacement. Significant progress in this direction has been achieved in the past decade, in particular with respect to iron,[4] manganese[5] and cobalt[6] based systems. Thus, several examples of base metal catalysed hydrogenations of aldehydes, ketones, carboxylic acids, esters and nitriles have been reported in recent years, some of them with remarkable activities and selectivities.[2a,7] On the contrary, hydrogenation of amides is known to a much less extent.[8] The latter can be attributed to the extremely low electrophilicity of the carbonyl group, which renders their hydrogenation particularly challenging.

In general, catalytic hydrogenation of amides can proceed *via* either C–N (hydrogenolysis) or C–O (hydrogenation) bond cleavage of the intermediate hemiaminal (Scheme 1). While the

C–O bond scission results in the formation of the alkylated/benzylated amine as the only by-product, the C–N bond cleavage leads to the free amine and the corresponding alcohol. Recently, an additional amide hydrogenation pathway was demonstrated, where the alkylated/benzylated amine is produced by a hydrogen borrowing/autotransfer mechanism from the initially formed alcohol and amine under specific acidic reaction conditions.[9] Until today, the development of catalytic systems that enable these chemoselective transformations continues to be challenging and therefore are subject of ongoing research.

Initial efforts in this direction mainly focused on homogeneous ruthenium catalysts.[10] Since the inspiring report by Cole-

[a]Leibniz Institut für Katalyse e. V., Albert-Einstein-Straße 29a, Rostock, 18059, Germany. E-mail: Matthias.Beller@catalysis.de

[b]Hylleraas Centre for Quantum Molecular Sciences, Department of Chemistry, University of Oslo, P.O. Box 1033, Blindern, N-0315, Oslo, Norway. E-mail: Ainara.nova@kjemi.uio.no
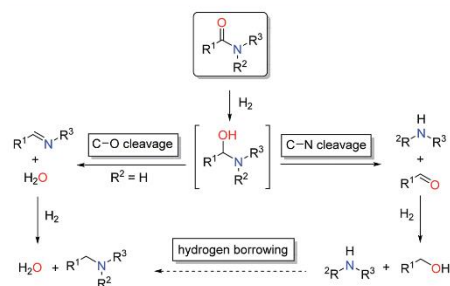
Scheme 1 Pathways for amide reduction.

151

Hamilton and co-workers in 2012, various Ru-based systems for the highly selective scission of either the C–N or the C–O bond have been described.[10]

In sharp contrast, reports on homogeneous base metal catalysts for this important reaction are particularly scarce. Pioneering work in this area was published by the groups of Milstein, Langer and Sanford only as late as 2016.[11–13] For the first time, they could demonstrate the ability of certain iron PNP pincer complexes (**Fe-1** as well as **Fe-2a/b**, Scheme 2) to promote the C–N bond cleavage in a number of different amides.

More specifically, Milstein and co-workers reported, that **Fe-1**, after activation with KHMDS, induced the hydrogenolysis of activated aliphatic and aromatic 2,2,2-trifluoroacetamides. However, no reaction was observed, with more common substrates such as *N*-phenylacetamide and *N*-phenylbenzamide.[11] The protocols described by Sanford (**Fe-2a**) and Langer (**Fe-2b**) showed more general substrate scopes and obtained notable conversions and yields also for unactivated amides.[12,13]

Additionally, Bernskoetter and co-workers showed that the pentavalent iron PNP-pincer complex **Fe-3** is particularly active for the hydrogenolysis of a number of secondary formanilides and *N*-formylmorpholine (Scheme 2). The system stands out due to its extremely low catalyst loading (0.018–0.07 mol%) and notably operates under base-free conditions. Interestingly, the group of Bernskoetter demonstrated that an addition of 20 equivalents of formanilide resulted in a significantly improved activity of the system towards otherwise almost unreactive *N*-methylformanilide. Based on NMR experiments, the authors concluded that the catalyst adopts a different resting state in the presence of the additive (**Fe-4**, Scheme 2) and thus is less prone towards deactivating side reactions.[14] The computational study of this reaction also suggested that the formanilide additive is involved in the C–N bond cleavage of the hemiaminal intermediate, which is the rate limiting step.[15]

Recently, our group reported the very first example of a manganese catalysed deaminative hydrogenation of amides

under relatively mild conditions.[16] After activation with exogenous base, the PNN pincer complex **Mn-1** (Scheme 2) exhibits remarkable activity for the hydrogenation of a broad scope of secondary and tertiary amides to the corresponding alcohols and amines. Notably, also more challenging primary amides were successfully cleaved in modest yields, tough more forcing conditions were shown to be necessary. The generality of the system was finally highlighted by the cleavage of the amide bond in the herbicide diflufenican. To date, **Mn-1** represents one of the most active and broadly applicable non-noble metal catalysts for amide hydrogenation. In a related study, Prakash and co-workers demonstrated that the manganese PNP pincer complex **Mn-2** is a suitable catalyst for the hydrogenation of formamides. The reaction proceeds *via* cleavage of the C–N bond to produce methanol and the corresponding amine.[17]

In 2018, we published the synthesis of a number of structurally related molybdenum PNP pincer complexes. Among the described complexes, **Mo-1a** (Table 1) was shown to be active in the catalytic hydrogenation of different acetophenones and styrenes.[18] Similar Mo-systems have also been used for the hydrogenation of CO_2, imines and nitriles.[19] Based on these reports and our previous work, we became interested in the behaviour of such base-metal catalysts for the reductive cleavage of amides. Herein, we demonstrate its suitability for the hydrogenolysis of *N*-methylated formanilides under relatively mild conditions. To the best of our knowledge, PNP pincer supported molybdenum complexes have not been described for such transformations. Interestingly, the optimal catalyst

Scheme 2 Base metal catalysts reported for the hydrogenolysis (C–N bond cleavage) of amides.

Table 1 Hydrogenation of *N*-methylformanilide **1a** to *N*-methylaniline **2a** and methanol **3** using Mo catalysts **Mo-1a–c** and **Mo-2**

Entry[a,b]	[Mo]	T [°C]	Conv.[c] [%]	2a[c] [%]
1	**Mo-1a**	130	>99	99
2	**Mo-1b**	130	>99	99
3	**Mo-1c**	130	>99	99
4	**Mo-2**	130	10	9
5[d]	—	130	10	8
6	**Mo-1a**	100	>99	98
7	**Mo-1b**	100	>99	99
8	**Mo-1c**	100	76	73
9	**Mo-1a**	80	89%	86%
10	**Mo-1b**	80	87%	84%
11[e]	**Mo-1a**	80	49	47
12[e]	**Mo-1b**	80	46	46

[a] Standard reaction conditions: *N*-methylformanilide **1a** (67.6 mg, 0.5 mmol), NaBHEt$_3$ (50 μL, 0.05 mmol, 10 mol%), 2 mL toluene, 50 bar H$_2$, 24 h. [b] Yield of **3** was not determined. [c] Conversion of **1a** and yield of **2a** were determined by GC using hexadecane as internal standard. [d] No catalyst was used. [e] Reaction was performed with 2.5 mol% of Mo catalyst.

152

exhibits a high selectivity for formamides. This preference has been rationalized by means of DFT calculations, which suggest that the produced MeOH reacts with the catalyst and changes the mechanism and rate limiting step of the reaction. This result, which is not observed in related Fe-catalysts, indicates that the catalyst design strategy should be adapted to the nature of the metal centre.

Results and discussion

Catalytic hydrogenation of amides using molybdenum pincer complexes

At the outset of our study, we explored molybdenum-based PNP pincer complexes **Mo-1a–c** and **Mo-2** (Table 1), recently synthesised by our group, as potential catalysts for the hydrogenation of amides. Using *N*-methylformanilide **1a** as benchmark substrate, preliminary experiments were conducted using 5 mol% of Mo catalyst in toluene at 50 bar H$_2$ and 130 °C, in the presence of 10 mol% of NaBHEt$_3$. The reaction proceeded smoothly for complexes **Mo-1a–c** to afford *N*-methylaniline **2a** in quantitative yield along with methanol as the only by-product (Table 1, entries 1–3). However, complex **Mo-2** failed to display any catalytic activity (Table 1, entry 4). Next, the activity of the complexes was tested at reduced temperatures (Table 1, entries 6–10). It was found, that complexes **Mo-1a** as well as **Mo-1b** were equally efficient, when the reaction was conducted at 100 °C. Catalyst **Mo-1c**, however, gave a somewhat lower conversion and yield. Further reduction of the reaction temperature to 80 °C resulted once again in similar conversions and yields for **Mo-1a** and **Mo-1b**, respectively. Based on these observations, the catalyst loading was reduced to 2.5 mol% under otherwise identical reaction conditions (Table 1, entries 11 and 12). It turned out, that changing this parameter also led to almost identical outcomes for both catalytic systems. Therefore we concluded that, under reaction conditions, **Mo-1a** and **Mo-1b** very likely form the same active species. On the basis of the obtained results and due to the more challenging synthesis of **Mo-1b**, we decided to focus on catalyst **Mo-1a** in the due course of the study.

Selecting 80 °C reaction temperature and 5 mol% of **Mo-1a** (Table 1, entry 8) as the optimal setting for further optimization, we tested several different solvents. In contrast to previous work on manganese catalysed hydrogenolysis of amides, toluene was found to give the best results. Cyclohexane yielded slightly lower activities, while *n*-heptane as well as polar solvents, were shown to be significantly less suitable for the attempted transformation (Fig. 1).

Subsequently, we studied the influence of dihydrogen pressure, catalyst loading as well as the amount of additive used on the reaction outcome (Table 1, see ESI†). Lowering the pressure to 30 bar H$_2$ resulted in a sharp drop in activity. However, no loss of reactivity was observed when the amount of NaBHEt$_3$ was decreased to 5 mol%. A rise of the reaction temperature to 100 °C resulted in full conversion of the benchmark substrate to *N*-methylaniline in the presence of 5 mol% NaBHEt$_3$ and **Mo-1a**, respectively. Further mitigation of the catalyst loading as well as
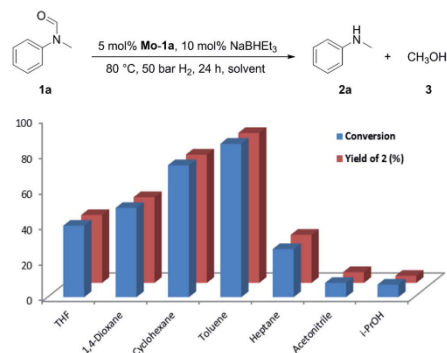
Fig. 1 Study of the solvent effect in the hydrogenation of *N*-methylformanilide **1a** to *N*-methylaniline **2a** and methanol **3** catalysed by **Mo-1a**.

the amount of NaBHEt$_3$, however, had negative effects on the catalytic performance of the system.

Having optimised conditions in hand, we proceeded to the application of **Mo-1a** in the hydrogenation of a variety of different *N*-methylformanilides to the corresponding anilines and methanol (Table 2).

Most substrates were hydrogenated in good to excellent yields under optimised conditions at 100 °C and 50 bar H$_2$ over 24 h, using toluene as solvent. In general, *meta*- and *para*-substitution were well tolerated, while substituents in *ortho*-position (Table 2, entries 19 and 20) appeared to be troublesome, probably due to steric hindrance. Amides containing electron donating groups were less reactive under standard conditions as compared to the benchmark substrate. In some cases higher reaction temperatures were required, in order to achieve good conversions (Table 2, entries 2, 6, 7). Notably, the thiomethyl substituted derivative (Table 2, entry 3) was fully hydrogenated and no catalyst poisoning effect was observed. Moreover, the system tolerated fluoro-substituents (Table 2, entries 8, 17, 20) and no dehalogenation products were detected. Interestingly, the system showed a good functional group tolerance towards substrates containing other reducible moieties such as benzyl ethers, C=C double bonds and esters (Table 2, entries 6, 12, 13). Noteworthy, no double bond isomerisation occurred during the reduction of a stilbene derivative (Table 2, entry 12). Additionally, pyridines, nitriles and nitro arenes remained unaffected under our reaction conditions; however, only poor to modest conversions were observed when the reaction was carried out at 130 °C (Table 2, entries 11, 14, 15). Presumably, this effect originates from substrate coordination to the metal centre and subsequent catalyst deactivation. The system turned out to be sensitive towards halides other than fluorine. Hence, during one of the hydrogenations, small amounts of the dehalogenation product were detected (Table 2, entry 9).

153

Edge Article

Table 2 Substrate scope in the hydrogenation of *N*-methylformanilides to *N*-methylanilines **2** and methanol **3** catalysed by **Mo-1a**

Table 2 *(Contd.)*

Entry[a,b]	Formamide	Conv[c]. (%)	Yield[d] of **2** (%)
1	**1a**	>99	94
2[e]	**1b**	>99	96
3	**1c**	>99	95
4	**1d**	83	80
5	**1e**	87	84
6[e]	**1f**	56	52
7[eg]	**1g**	46	43
8	**1h**	98	93
9	**1i**	40	34[f]

Entry[a,b]	Formamide	Conv[c]. (%)	Yield[d] of **2** (%)
10	**1j**	>99	>99
11[e]	**1k**	52	50
12	**1l**	95	92
13	**1m**	>99	97
14[e]	**1n**	14	12[f]
15[e]	**1o**	8	6[f]
16	**1p**	>99	97
17	**1q**	>99	98

154

Table 2 (*Contd.*)

Entry[a,b]	Formamide	Conv.[c]. (%)	Yield[d] of **2** (%)
18	**1r**	>99	93
19[e]	**1s**	12	9[f]
20[e]	**1t**	18	15[f]

[a] Standard reaction conditions: *N*-methylformanilide (0.5 mmol), **Mo-1a** (12.5 mg, 5 mol%), NaBHEt₃ (50 µL, stock solution 0.5 M in THF, 5 mol%), 2 mL toluene, 50 bar H₂, 24 h. [b] Yield of **3** was not determined. [c] Conversions of *N*-methylformanilides were determined by GC using hexadecane as internal standard. [d] Isolated yields. [e] Reaction was carried out at 130 °C. [f] Yields were determined by GC using hexadecane as internal standard. [g] Yield was determined based on the hydrochloride salt.

Subsequently, we investigated the more general applicability of our PNP pincer complex **Mo-1a** in the hydrogenation of other amides. Initial experiments focussed on the role of the nitrogen

substitution on the reaction outcome. For this purpose, a series of different secondary and tertiary formanilides were subjected to our protocol (Scheme 3). The presence of an NH moiety turned out to be detrimental, as was observed for the parental formanilide (**4a**). This is in sharp contrast with the results obtained with Fe pincer complexes, in which formanilide derivatives give the highest conversion.[14] In order to further validate this, 2,2,2-trifluoroacetanilide (**6a**) and simple benzanilide (**7a**) were employed and results comparable to formanilide (**4a**) were obtained. Likewise, only low conversions and yields were obtained in the case of *N*-ⁱPr- (**4b**) and *N*-allylformanilide (**4c**), respectively. Surprisingly, when *N*-allylformanilide was tested as substrate, the formation of *N*-allylaniline was only observed in traces. The main product was identified to be aniline, thus hinting at a deallylation pathway that additionally takes place to the envisaged hydrogenolysis. In contrast, *N*,*N*-diphenylformanilide (**4d**) was reduced smoothly and *N*,*N*-diphenylamine was isolated in excellent yield. Next, the hydrogenation of *N*-methylacetanilide (**5**) and the more activated 2,2,2-*N*-methyltrifluoroacetanilide (**6b**), respectively, were attempted. In either case, only poor conversions were determined demonstrating the high preference of this complex for specific formanilides. This was further supported by the low reactivity of *N*-methylbenzanilide (**7b**) and some aliphatic formamides (see Table 2, ESI†).

Based on these observations, we were curious to demonstrate selective formamide reduction in the presence of other amide moieties. In a proof of concept experiment, the hydrogenation of the benchmark amide in the presence of benzamide **7a** was conducted (Scheme 4, eqn (a)). It could be shown that **Mo-1a** was capable to cleave *N*-methylformanilide (**1a**) with extremely high preference. Notably, the reaction still proceeded with 80% conversion with respect to *N*-methylformanilide (**1a**). To further highlight the scope of our system, we designed model substrate **9** combining two amide functionalities in one structure. After 24 h reaction, the intended hydrogenolysis of

Scheme 3 Hydrogenation of different amides (**4–7**) to the corresponding amines and alcohols catalysed by **Mo-1a**. [a]Conversions of amides were determined by GC using hexadecane as internal standard. [b]Yields were determined by GC using hexadecane as internal standard and refer to anilines, yields of alcohols were not determined. [c]Isolated yields of anilines.

4a R = H, 13%[a] (11%)[b] **6a** R = H, 14%[a] (11%)[b] **7a** R = H, 19%[a] (14%)[b]
4b R = *i*-Pr, 8%[a] (4%)[b] **6b** R = CH₃, 26 %[a] (20%)[b] **7b** R = CH₃, 31%[a] (28%)[b]
4c R = C₃H₅,14%[a] (1%)[b]
4d R = Ph, 91%[a] (86%)[c]

Scheme 4 Selective hydrogenations of (a) *N*-methylformanilide **1a** in the presence of benzamide **7a** and (b) *N*-methyl-*N*-(4-(*N*-methylformamide)phenyl)benzamide **9**. Standard conditions: substrate(s) 0.5 mmol (each), **Mo-1a** (12.5 mg, 0.025 mmol, 5 mol%), NaBHEt₃ (50 µL, 0.5 M stock solution in THF, 0.025 mmol, 5 mol%), toluene (2 mL), 50 bar H₂, 100 °C, 24 h. [a]Conversions determined by GC using hexadecane as internal standard. [b]Yields determined by GC using hexadecane as internal standard. [c]Isolated yield.

155

the formamide moiety in **9** had occurred smoothly and the target molecule **10** was isolated in a very high yield (92%). Notably, no cleavage of the benzamide was observed.

We believe these results could pave the way towards new and selective deprotection strategies in organic synthesis mediated by this base metal PNP pincer complex.

Reaction mechanism

In order to understand the general reactivity of **Mo-1a** and its performance with different amides, DFT calculations and supporting experiments were conducted. Scheme 5 shows the experiments performed to determine the active catalyst species. Treatment of **Mo-1a** with NaBHEt$_3$ resulted in rapid hydrogen evolution. The nature of the gas was determined in a scale up experiment (100 μmol of **Mo-1a**) using GC-analysis. This observation prompted us to assume that the obtained reaction product was likely to be a pincer amido species such as **Mo-3**, in which Mo(I) has been reduced to Mo(0). This conclusion was further supported by HR-ESI mass spectrometry of the corresponding reaction mixture. When the distinct reactivity of the catalyst towards formanilide was studied, we isolated **Mo-4** in form of colorless needles from the reaction mixture (Fig. 2; for detailed experimental procedure see ESI†).

Notably, the crystal structure of **Mo-4** (Fig. 2 and Scheme 5) features two anionic Mo(0) complexes neutralized by two Na$^+$ cations interacting with the CO ligands. In order to investigate, whether **Mo-4** is involved in the catalytic cycle, the reduction of N-methylformanilide was carried out using 2.5 mol% of **Mo-4** under conditions optimized for **Mo-1a**. In fact, we observed full conversion of the substrate and isolated N-methylaniline in 92% yield. Thus, we conclude, that the catalytically active species contains a Mo(0) center. This is also consistent with the EPR-silent nature of the product formed in the activation of **Mo-1a** by NaBHEt$_3$.
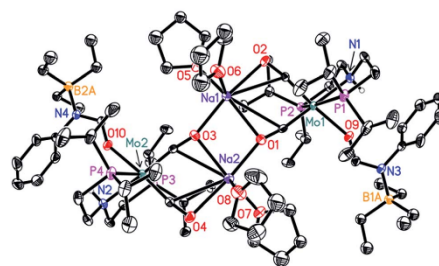

Fig. 2 Molecular structure of **Mo-4** in the crystal (see Scheme 5 for a graphical representation). Displacement ellipsoids correspond to 30% probability. Hydrogen atoms except the N-bound are omitted for clarity.

The observed activity of **Mo-4** suggests that the Mo(0)-complexes **Mo-3** and **Mo-5**, shown in Scheme 5, are presumably the main catalytic intermediates. Similar species have been proposed for the isoelectronic Fe(II)-complexes **Fe-2**, **Fe-3** and the Mn(I)-complex **Mn-2** (Scheme 2).[20]

Based on these results, DFT calculations, with the M06 functional, including toluene solvation with the SMD model, were used to get further insights into the reaction mechanism (see computational details and ESI for details†). The hydrogenation of **Mo-3** to yield **Mo-5**, was found to be almost isoenergetic, with a small preference for **Mo-3** at 1 bar and **Mo-5** at 50 bar (Scheme 5). These energies agree with the bubbling of H$_2$ observed experimentally during the catalyst activation reaction.

As represented in Scheme 1, amide hydrogenolysis is proposed to consist in three steps: amide C=O reduction, C–N bond protonolysis of the formed hemiaminal, and aldehyde C=O reduction. These steps were computed for N-methylformanilide and the energy profiles for the preferred pathways are given in Fig. 3 and 5, and the ESI.†

The mechanism for the amide C=O hydrogenation by **Mo-5** consists of the hydride transfer from Mo to the amide carbonyl group (**Mo-ts-6-7**), followed by proton transfer from the ligand nitrogen to the amide oxygen (**Mo-ts-7-8**). This pathway was computed for formanilide (**Mo-ts-6-7^{NH}** in Fig. 3) and N-methylformanilide. With both substrates, the hydride transfer has the highest energy barrier (10.6 kcal mol^{-1} with formanilide and 13.1 kcal mol^{-1} with N-methylformanilide). Interestingly, these energies are lower than those reported by us for the analogous Fe catalyst with formanilide (15.8 kcal mol^{-1}, **Fe-ts-6-7** in Fig. 3).[15]

The mechanism for the C–N bond cleavage from the formed hemiaminal (Scheme 1) was also investigated. In the case of **Fe-3**, this step was reported to proceed via the transition state **Fe-ts-C^H–N^H** (Fig. 4).[15] With Mo and N-methylformanilide, the same pathway involves a Gibbs energy barrier of 22.9 kcal mol^{-1} (**Mo-ts-C^H–N^{Me}**). An increase of less than 1 kcal mol^{-1} is observed by changing the substrate to N-methylacetanilide (**Mo-ts-C^{Me}–N^{Me}**).
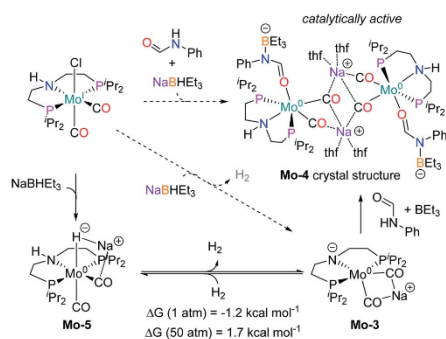
Scheme 5 Reactions performed to get insight on the active catalytic species (in dashed arrows) with the experimental observed products (H$_2$ and the crystal structure of **Mo-4**, in color) and the intermediates proposed (**Mo-3** and **Mo-5**). Gibbs energies calculated for the dehydrogenation of **Mo-5** at different pressure.
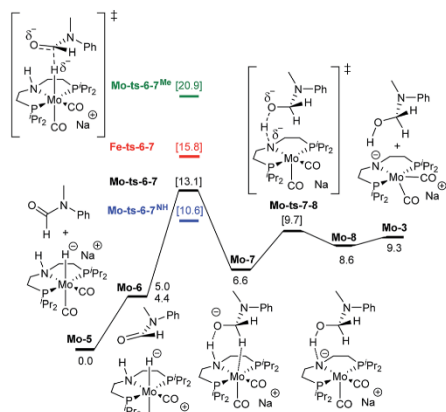
156

Fig. 3 Reaction pathway for the hemiaminal formation from the *N*-methyl formanilide with **Mo-5**. Gibbs energies in toluene (SMD) at 50 atm and 373 K are given in kcal mol⁻¹. In blue and green, energies for the hydride transfer using formanilide and *N*-methylacetanilide, respectively. In red, energy for the hydride transfer using the reported **Fe-3** complex at 30 atm (Scheme 2).[15]

Fig. 5 Reaction pathway of the MeOH assisted hemiaminal proton transfer and posterior C–N bond cleavage. Gibbs energies in toluene (SMD) at 50 atm and 373 K are given in kcal mol⁻¹.

The similar energy barriers obtained with these substrates did not account for the large differences in yield observed experimentally (99% Conv. in *N*-methylformanilide *vs.* 20% Conv. in *N*-methylacetanilide). In addition, the lower energy barriers obtained with Mo compared to Fe are inconsistent with the higher H_2 pressure and time required to accomplish amide hydrogenation with **Mo-1a** compared to **Fe-3**.[14]

These discrepancies were explained by considering the reaction of **Mo-3** with methanol leading to the Mo-methoxy intermediate **Mo-9a** (Fig. 5). This reaction, which involves the deprotonation of MeOH by the amido ligand (**Mo-ts-3-9a**), has a low energy barrier ($\Delta G^{\ddagger} = 2.8$ kcal mol⁻¹) and is highly exergonic ($\Delta G = -11.4$ kcal mol⁻¹). The formation of related M-methoxy species have been observed for similar Fe, Ru, Os and Mn PNP-pincer complexes.[20c,21,22] This species can promote the protonolysis of the C–N bond by assisting the OH-deprotonation and *N*-protonation of the hemiaminal
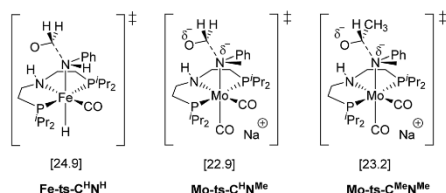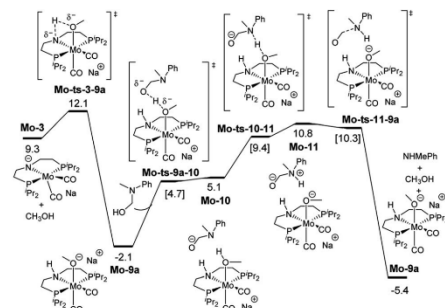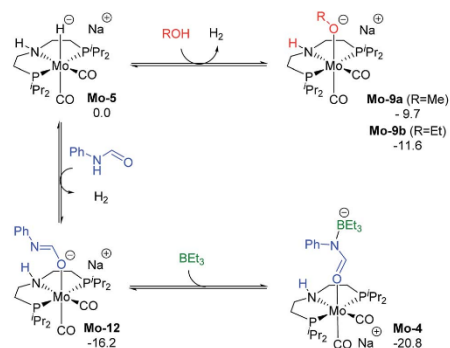
intermediate (**Mo-ts-11-9a**). The highest energy of this process is 10.8 kcal mol⁻¹, which corresponds to the zwitterion hemiaminal intermediate interacting with the methoxide–Mo complex (**Mo-11**). This energy is lower than the energy barrier for the hydride transfer (13.1 kcal mol⁻¹), indicating that the C–N bond cleavage is not the rate limiting step once MeOH is formed (note: for a comparison of this mechanism with Mo and Fe-systems see ESI†).

The reaction of **Mo-5** with MeOH yields hydrogen and is exergonic ($\Delta G = -9.7$ kcal mol⁻¹, Scheme 6). The methoxy intermediate **Mo-9a** is thus the resting state of the catalyst.

Formanilide, and other secondary amides, can also displace H_2 from the catalyst (**Mo-12** in Scheme 6). This reaction is even more exergonic ($\Delta G = -16.2$ kcal mol⁻¹) than with MeOH increasing the global energy barrier for the hydride transfer from 10.6 to 26.8 kcal mol⁻¹ with formanilide. This energy may increase to 31.4 kcal mol⁻¹ by reaction with BEt₃ (**Mo-4**). In

Fig. 4 TSs for the C–N bond cleavage step *via* the mechanism previously reported for **Fe-3**.[15]

Scheme 6 Calculated Gibbs energies (kcal mol⁻¹) for the substitution of H_2 in **Mo-5** by methanol, ethanol, formanilide and BEt₃ yielding **Mo-9a, b, Mo-10** and **Mo-4**, respectively.

157

contrast, with N-methylformanilide, the only penalty to pay is the addition of MeOH. Therefore, the energy barrier for the hydride transfer increases from 13.1 to 22.9 kcal mol^{-1}, which is lower than the barrier for formanilide, consistent with the larger conversion obtained with N-methylformanilide. In the case of N-methylacetanilide, the addition of ethanol instead of methanol is expected. The higher stability of the ethoxide complex **Mo-9b** compared to **Mo-9a** by $ca.$ 2 kcal mol^{-1} (Scheme 6), together with the higher energy barrier for the hydride transfer with this substrate ($\Delta G = 20.9$ kcal mol^{-1}, Fig. 3), is consistent with the low yields obtained experimentally with N-methylacetanilide.

The mechanism of catalyst recovery by addition of H$_2$ to the methoxide complex **Mo-9a** is shown in Fig. S3.† In this pathway, methanol assists the activation of the Mo–H$_2$ complex (**Mo-14**) by acting as a proton-shuttle with a global energy barrier of 23.0 kcal mol^{-1}. Similar mechanisms have been proposed with Ru–N and Fe–N complexes (see ESI†).[21b,23]

The results from the computational study can be summarized in the catalytic cycle represented in Fig. 6. In the absence of alcohol, the Mo-catalyst is involved in the hemiaminal C–N bond cleavage after the amide C=O reduction (blue cycle). This reaction yields amine and formaldehyde, which is reduced to alcohol by the catalyst **Mo-5** in a subsequent reaction (in red). In the presence of alcohol, a Mo-alkoxo intermediate is formed, **Mo-9a**. This species, which becomes the catalyst resting state, is involved in the hemiaminal C–N bond cleavage. Finally, the
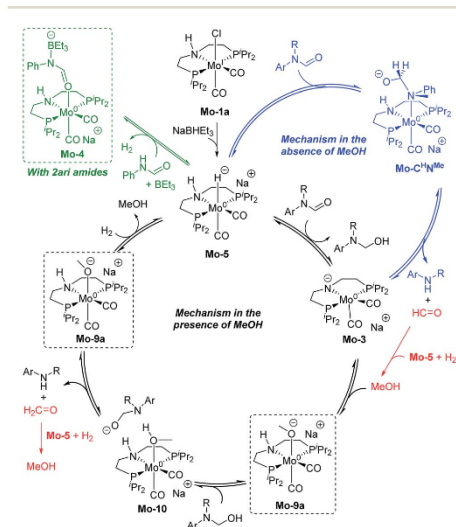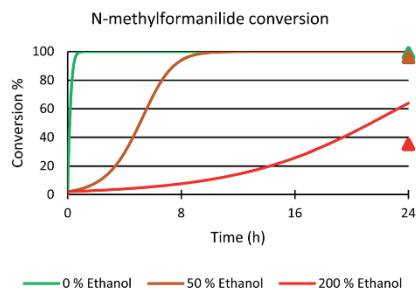

Fig. 7 Microkinetic simulation of N-methylformanilide **1a** conversion with 0% (green), 50% (brown) and 200% (red) ethanol in solution. The initial concentration of reactants were the same as those used in the experiments; $i.e.$ 0.25 M N-methylformanilide **1a**, 0.207 M of dihydrogen and 12.5 mM of **Mo-5**. Experimental values at 24 hours represented with triangles.

catalyst recovery takes place by the displacement of alcohol by H$_2$. The nature of the catalyst resting state may change with secondary amides, which reacts with the catalyst forming an adduct (**Mo-4**, in green) that hampers the reaction.

In order to validate this mechanism and the nature of Mo(0) active species, the role of the counter-cation in this reaction was explored computational and experimentally by using LiHBEt$_3$, NaHBEt$_3$, and KHBEt$_3$. Carrying out the benchmark reaction at 80 °C, 5 mol% of the alkali metal hydrides were added to activate **Mo-1a**. It could be shown, that for NaBHEt$_3$ and KBHEt$_3$ similar conversions of N-methylformanilide (**1a**) (76% and 77%, respectively) and yields of **2a** (75% and 73%, respectively) were obtained. However, when LiBHEt$_3$ was used, only 10% conversion of **1a** and 9% yield of N-methylaniline **2a** was obtained. These results were in agreement with the trends on the energy barriers obtained for the amide C=O reduction step, which are 22.9, 23.0 and 28.8 kcal mol^{-1} with Na$^+$, K$^+$ and Li$^+$, respectively, taking **Mo-9a** as energy reference. The stronger electrostatic interaction of Li$^+$ with the methoxide intermediate (**Mo-9a**^{Li}), accounts for the highest energy barrier predicted for this system (see ESI†).

Next, the role of the alcohol was explored by adding different amounts of ethanol to the benchmark system. In the presence of 50 mol% of EtOH, 96% conversion of N-methylformanilide (**1a**) and 93% product yield were obtained. However, the addition of 200 mol% resulted in a sharp decrease in conversion and yield (35% conversion, 32% yield). Thus, it was concluded that ethanol has a detrimental effect on the performance of the catalytic system. Notably, these trends were reproduced with a microkinetic model based on the general mechanism represented in Fig. 6 (in Fig. 7). This model predicted 100% conversion after 24 h of reaction for both 0% and 50% concentrations of ethanol. In contrast, and in line with the experiments, the same model predicted a significant decrease of conversion to 64% with an ethanol concentration of 200% (see ESI for further details†).

Fig. 6 General mechanism for the amide hydrogenation in the absence (in blue) and presence (in black) of methanol with the formaldehyde hydrogenation in red. Dashed squares indicate the catalyst resting state in the presence of MeOH and 2ari amides (in green).

Conclusions

Well-defined molybdenum–PNP pincer complexes have been used for the first time in the hydrogenation of a range of amides to the corresponding alcohols and amines. *N*-Alkylated and *N*-arylated formamides can be hydrogenated to the corresponding products in good to high yields. Applying complex **Mo-1a** high selectivity for the hydrogenation of formamides was observed in the presence of other reducible groups. These results pave the way for potential applications of this type of complexes in synthetic methodologies.

The DFT study shows that the active Mo(0) species (**Mo-5**) reduces the C=O group of the amide through low-energy barriers, compared to Fe-based systems. However, the alcohol product and secondary amides react with the catalyst forming stable adducts encumbering catalyst recovery and increasing the overall barrier for the reduction of the C=O group. These results suggest that further catalyst design should focus on preventing the formation of these adducts, while keeping the high hydricity of the complex.

Experimental details

General experimental information

All hydrogenation reactions were set up under Ar in a 300 mL autoclave (PARR Instrument Company). In order to avoid unspecific reductions, all catalytic experiments were carried out in 4 mL glass vials, which were set up in an alloy plate and placed inside the autoclave.

In a glove box, a 4 mL glass vial containing a stirring bar was charged with complex **Mo-1a** (12.5 mg; 5 mol%). Toluene (2 mL) was added and the corresponding brown suspension was treated with NaBHEt$_3$ (0.5 M in THF; 50 μL; 10 mol%). The reaction mixture was stirred for 10 minutes and the corresponding substrate was subsequently added. Afterwards, the vial was capped and transferred into an autoclave. Once sealed, the autoclave was purged three times with 10 bar of hydrogen, then pressurized to the desired hydrogen pressure (50 bar), and placed into an aluminum block that was preheated to the desired temperature (100 °C). After 24 h, the autoclave was cooled in an ice bath and the remaining gas was released carefully. The solution was subsequently diluted with ethyl acetate and filtered through a small pad of Celite (1 cm in a Pasteur pipette). The Celite was washed with methanol (2 mL) and the combined filtrates were subsequently evaporated to dryness. The remaining residue was purified by column chromatography (SiO$_2$, heptane/EtOAc, gradient 100 : 0 → 0 : 100). In the case of substrate **7**, the purified product was dissolved in 5 mL of Et$_2$O and subsequently treated with 1 mL of HCl (2 M in Et$_2$O). The reddish precipitate was filtered off, washed three times with 5 mL of Et$_2$O and finally dried *in vacuo*. For the characterization of the products of the catalysis, see ESI.†

Computational details

DFT calculations were carried out with Gaussian 09 [24] with the M06 [25] functional and the double-z LANL2DZ (on Mo, including relativistic effects) [26] and 6-31+G** (on all other elements) [27] basis sets. Calculations were done using the full system. The location of the Na$^+$ cation was evaluated in some of the intermediates, and the preferred position is represented in figures and schemes of the manuscript (see ESI†). The geometry optimization and energies of the possible spin states of **Mo-1a** and **Mo-4** were consistent with a doublet and singlet ground state, respectively (see ESI†). Vibrational frequencies were computed at the same level of theory to obtain the thermochemistry corrections (zero-point, thermal and entropy energies) at the experimental $p = 50$ atm and $T = 373.15$ K. The energy of the optimized geometries was refined by single point calculations with triple-z quality basis sets, including the LANL2TZ [26] on Mo and the 6-311+G** on all other elements. [28] The energies reported in the text were obtained by adding the thermochemistry corrections to the refined potential energies. The solvation effects of toluene were included in both the geometry optimizations and energy refinements using the continuum SMD model. [29] The ultrafine (99 590) grid was used in all calculations for higher numerical accuracy. A repository containing all input and output files is available on-line from ioChem BD at https://iochem-bd.bsc.es/browse/handle/100/193698. [30] Microkinetic models were simulated with the COPASI software [31] using the LSODA algorithm. See ESI for further details.†

Conflicts of interest

There are no conflicts to declare.

Acknowledgements

Notes and references

1 (*a*) P. Roose, K. Eller, E. Henkes, R. Rossbacher and H. Höhke, *Ullmann's Encyclopedia of Industrial Chemistry*, Germany, 2000; (*b*) P. G. Jessop, *The Handbook of Homogeneous Hydrogenation*, Germany, 2006.
2 For selected examples of carboxylic acid derivatives hydrogenation, see: (*a*) S. Werkmeister, K. Junge, B. Wendt, E. Alberico, H. J. Jiao, W. Baumann, H. Junge, F. Gallou and M. Beller, *Angew. Chem., Int. Ed.*, 2014, **53**, 8722–8726; (*b*) T. vom Stein, M. Meuresch, D. Limper, M. Schmitz, M. Holscher, J. Coetzee, D. J. Cole-Hamilton, J. Klankermayer and W. Leitner, *J. Am. Chem. Soc.*, 2014, **136**, 13217–13225; (*c*) D. Srimani, A. Mukherjee, A. F. G. Goldberg, G. Leitus, Y. Diskin-Posner, L. J. W. Shimon, Y. Ben David and D. Milstein, *Angew. Chem., Int. Ed.*, 2015, **54**, 12357–12360; (*d*) X. J. Cui,

Y. H. Li, C. Topf, K. Junge and M. Beller, *Angew. Chem., Int. Ed.*, 2015, **54**, 10596–10599; (*e*) T. J. Korstanje, J. I. van der Vlugt, C. J. Elsevier and B. de Bruin, *Science*, 2015, **350**, 298–301; (*f*) M. Naruto and S. Saito, *Nat. Commun.*, 2015, **6**, 8140; (*g*) J. R. Cabrero-Antonino, I. Sorribes, K. Junge and M. Beller, *Angew. Chem., Int. Ed.*, 2016, **55**, 387–391.

3 (*a*) B. Cornils and W. A. Herrmann, *Applied Homogenous Catalysis with Organometallic Compounds: A Comprehensive Handbook in Two Volumes*, Germany, 1996; (*b*) D. L. Dodds and D. L. Cole-Hamilton, *Sustainable Catalysis*, United States of America, 2013.

4 D. Wie, C. Netkaew and C. Darcel, *Eur. J. Inorg. Chem.*, 2019, 2471–2487.

5 M. Garbe, K. Junge and M. Beller, *Eur. J. Org. Chem.*, 2017, **30**, 4344–4362.

6 G. A. Filonenko, R. van Putten, E. J. M. Jensen and E. A. Pidko, *Chem. Soc. Rev.*, 2018, **47**, 1459–1483.

7 For selected examples see: (*a*) R. Langer, G. Leitus, Y. Ben-David and D. Milstein, *Angew. Chem., Int. Ed.*, 2011, **50**, 2120–2124; (*b*) N. Gorgas, B. Stöger, L. F. Veiros, E. Pittenauer, G. Allmaier and K. Kirchner, *Organometallics*, 2014, **33**, 6905–6914; (*c*) T. Zell, Y. Ben-David and D. Milstein, *Catal. Sci. Technol.*, 2015, **5**, 822–826; (*d*) N. Gorgas, B. Stöger, L. F. Veiros and K. Kirchner, *ACS Catal.*, 2016, **6**, 2664–2672; (*e*) S. Elangovan, B. Wendt, C. Topf, S. Bachmann, M. Scalone, A. Spannenberg, H. Jiao, W. Baumann, K. Junge and M. Beller, *Adv. Synth. Catal.*, 2016, **358**, 820–825; (*f*) S. Lange, S. Elangovan, C. Cordes, A. Spannenberg, H. Jioa, H. Junge, S. Bachmann, M. Scalone, C. Topf, K. Junge and M. Beller, *Catal. Sci. Technol.*, 2016, **6**, 4768–4772; (*g*) S. Elangovan, C. Topf, S. Fischer, H. Jiao, A. Spannenberg, W. Baumann, R. Ludwig, K. Junge and M. Beller, *J. Am. Chem. Soc.*, 2016, **138**, 8809–8814.

8 (*a*) P. M. Rylander, *Hydrogenation Methods*, Academic Press, London, 1985; (*b*) J. Hartwig, *Organotransition Metal Chemistry*, University Science Books, 2010.

9 (*a*) D. Cantillo, *Eur. J. Inorg. Chem.*, 2011, **19**, 3008–3013; (*b*) P. A. Dub and T. Ikariya, *ACS Catal.*, 2012, **2**, 1718–1741; (*c*) A. M. Smith and R. Whyman, *Chem. Rev.*, 2014, **114**, 5477–5510.

10 (*a*) A. A. Nunez Magro, G. R. Eastham and D. J. Cole-Hamilton, *Chem. Commun.*, 2007, **30**, 3154–3156; (*b*) E. Balaraman, B. Gnanaprakasam, L. J. W. Shimon and D. Milstein, *J. Am. Chem. Soc.*, 2010, **132**, 16756–16758; (*c*) J. M. John and S. H. Bergens, *Angew. Chem., Int. Ed.*, 2011, **50**, 10377–10380; (*d*) J. Coetzee, D. L. Dodds, J. Klankermayer, S. Brosinksi, W. Leitner, A. M. Z. Slawin and D. J. Cole-Hamilton, *Chem.–Eur. J.*, 2013, **19**, 11039–11050; (*e*) T. Miura, I. E. Held, S. Oishi, M. Naruto and S. Saito, *Tetrahedron Lett.*, 2013, **54**, 2674–2678; (*f*) T. vom Stein, M. Meureusch, D. Limper, M. Schmitz, M. Hölscher, J. Coetzee, D. J. Cole-Hamilton, J. Klankermayer and W. Leitner, *J. Am. Chem. Soc.*, 2014, **136**, 13217–13225; (*g*) J. R. Cabrero-Antonino, E. Alberico, H. J. Drexler, W. Baumann, K. Junge, H. Junge and M. Beller, *ACS Catal.*, 2016, **6**, 47–54; (*h*) L. Shi, X. Tan, J. Long, X. Xiong,

S. Yang, P. Xue, H. Lv and X. Zhang, *Chem.–Eur. J.*, 2017, **23**, 546–548.

11 J. A. Garg, S. Chakraborty, Y. Ben-David and D. Milstein, *Chem. Commun.*, 2016, **52**, 5285–5288.

12 N. M. Rezayee, D. C. Samblanet and M. S. Sanford, *ACS Catal.*, 2016, **6**, 6377–6383.

13 F. Schneck, M. Assmann, M. Balmer, K. Harms and R. Langer, *Organometallics*, 2016, **35**, 1931–1943.

14 U. Jayaranthe, Y. Zhang, N. Hazari and W. Bernskoetter, *Organometallics*, 2017, **36**, 409–416.

15 L. A. Suarez, Z. Culacova, D. Balcells, W. H. Bernskoetter, O. Eisenstein, K. I. Goldberg, N. Hazari, M. Tilset and A. Nova, *ACS Catal.*, 2018, **8**, 8751–8762.

16 V. Papa, J. R. Cabrero-Antonino, E. Alberico, A. Spannenberg, K. Junge, H. Junge and M. Beller, *Chem. Sci.*, 2017, **8**, 3576–3585.

17 S. Kar, A. Goeppert, J. Kothandaraman and J. K. S. Prakash, *ACS Catal.*, 2017, **7**, 6347–6351.

18 T. Leischner, A. Spannenberg, K. Junge and M. Beller, *Organometallics*, 2018, **37**, 4402–4408.

19 (*a*) S. Chakraborty, O. Blacque, T. Fox and H. Berke, *Chem.–Asian J.*, 2014, **9**, 328–337; (*b*) S. Chakraborty, O. Blacque and H. Berke, *Dalton Trans.*, 2015, **44**, 6560–6570; (*c*) S. Chakraborty and H. Berke, *ACS Catal.*, 2014, **4**, 2191–2194; (*d*) Y. Zhang, P. G. Williiard and W. H. Bernskoetter, *Organometallics*, 2016, **35**, 860–865.

20 (*a*) S. Chakraborty, P. Lagaditis, M. Förster, E. A. Bielinski, N. Hazari, M. C. Holthausen, W. D. Jones and S. Schneider, *ACS Catal.*, 2014, **4**, 3994–4003; (*b*) E. A. Bielinski, P. Lagaditis, Y. Zhang, B. Q. Mercado, C. Würtele, W. H. Bernskoetter, N. Hazari, S. Schneider and P. O. Lagaditis, *J. Am. Chem. Soc.*, 2014, **136**, 10234–10237; (*c*) D. Nguyen, X. Trivelli, F. Capet, J. F. Paul, F. Dumeignil and R. M. Gauvin, *ACS Catal.*, 2017, **7**, 2022–2032.

21 (*a*) Z. Shao, Y. Wang, Y. Liu, Q. Wang, X. Fu and Q. Liu, *Org. Chem. Front.*, 2018, **5**, 1248–1256; (*b*) X. Chen, Y. Jing and X. Yang, *Chem.–Eur. J.*, 2016, **22**, 1950–1957; (*c*) E. Bielinski, P. Föster, Y. Zhang, W. H. Bernskoetter, N. Hazari and M. Holthausen, *ACS Catal.*, 2015, **5**, 2404–2415.

22 D. Gusev, *ACS Catal.*, 2017, **7**, 6656–6662.

23 (*a*) G. Zhang and S. Hanson, *Chem. Commun.*, 2013, **49**, 10151–10153; (*b*) Z. Wie, A. De Aguirre, K. Junge, M. Beller and H. Jiao, *Catal. Sci. Technol.*, 2018, **8**, 3649–3665.

24 M. J. Frisch, G. W. Trucks, H. B. Schlegel, G. E. Scuseria, M. A. Robb, J. R. Cheeseman, G. Scalmani, V. Barone, B. Mennucci, G. A. Petersson, H. Nakatsuji, M. Caricato, X. Li, H. P. Hratchian, A. F. Izmaylov, J. Bloino, G. Zheng, J. L. Sonnenberg, M. Hada, M. Ehara, K. Toyota, R. Fukuda, J. Hasegawa, M. Ishida, T. Nakajima, Y. Honda, O. Kitao, H. Nakai, T. Vreve, J. A. Montgomery, J. E. Peralta, F. Ogliare, M. Bearpark, J. J. Heyd, E. Brothers, K. N. Kudin, V. N. Staroverov, T. Keith, R. Kobayashi, J. Normand, K. Raghvachari, A. Rendell, J. C. Burant, S. S. Iyengar, J. Tomasi, M. Cossi, N. Rega, J. M. Millam, M. Klene, J. E. Knox, J. B. Cross, V. Bakken,

160

C. Adamo, J. Jaramillo, R. Gomperts, R. E. Stratmann, O. Yazyev, A. J. Austin, R. Cammi, C. Pomelli, J. W. Ochterski, R. L. Martin, K. Morokuma, V. G. Zakrzewski, G. A. Voth, P. Salvador, J. J. Dannenberg, S. Dapprich, A. D. Daniels, O. Fakas, J. B. Foresman, J. V. Ortiz, J. Cioslowski and D. J. Fox, *Gaussian 09, Revision D.01*, Gaussian, Inc., Wallingford CT, 2013.

25 Y. Zhao and D. Truhlar, *Theor. Chem. Acc.*, 2008, **120**, 215–241.

26 (*a*) P. Hay and W. Wadt, *J. Chem. Phys.*, 1985, **82**, 270–283; (*b*) W. Wadt and P. Hay, *J. Chem. Phys.*, 1985, **82**, 284–298.

27 (*a*) W. J. Hehre, R. Ditchfield and J. A. Pople, *J. Chem. Phys.*, 1972, **56**, 2257–2261; (*b*) W. Kohn, A. D. Becke and R. G. Parr, *J. Phys. Chem.*, 1996, **1**, 12974–12980.

28 A. McLean and G. Chandler, *J. Chem. Phys.*, 1980, **72**, 5639–5648.

29 A. Marenich, C. Cramer and D. Truhlar, *J. Phys. Chem. B*, 2009, **113**, 6378–6396.

30 M. Álvarez-Moreno, C. De Graaf, N. López, F. Maseras, J. M. Poblet and C. Bo, *J. Chem. Inf. Model.*, 2015, **55**, 95–103.

31 S. Hoops, R. Gauges, C. Lee, J. Pahle, N. Simus, M. Singhal, L. Xu, P. Mendes and U. Kummez, *Bioinformatics*, 2006, **22**, 3067–3074.

Computational Details

General Computational Information.

DFT calculations were carried out with the Gaussian09 software package.[10] The hybrid meta-GGA M06[11] functional was selected on the basis of geometry (Figure S1 Table S1) benchmark, using X-Ray crystal structures as references. Structures were fully optimized without any geometry or symmetry constraints, combining the double-z LANL2DZ (on Mo, including relativistic effects)[12] and 6-31+G** (on all other elements)[13] basis sets. Vibrational frequencies were computed at the same level of theory to classify all stationary points as either saddle points (transition states, with a single imaginary frequency) or energy minima (reactants, intermediates and products, with only real frequencies). These calculations were also used to obtain the thermochemistry corrections (zero-point, thermal and entropy energies) at the experimental $p = 50$ atm and $T = 373$ K. The energy of the optimized geometries was refined by single point calculations with triple-z quality basis sets, including the LANL2TZ[12] on Mo and the 6-311+G** on all other elements.[14] The energies reported in the text were obtained by adding the thermochemistry corrections to the refined potential energies. The solvation effects of toluene were included in both the geometry optimizations and energy refinements using the continuum SMD model.[15] The ultrafine (99,590) grid was used in all calculations to increase numerical accuracy and to facilitate convergence. A data set collection of input files and computational results is available in the ioChem-BD repository and can be accessed online via https://iochem-bd.bsc.es/browse/handle/100/193698.[16] The complex reaction mechanisms inferred from the calculations were interpreted by means of quantitative microkinetic models (Figure S4, Figure S5 and Table S2), simulated with the COPASI software.[17] Time course simulation were carried with the LSODA algorithm.

DFT functional benchmark

In a previous work of the group, the hydrogenation of amides by an iron (II) Noyori-type bifunctional catalyst was studied by using the M06 functional.[6] This method was selected based on a method benchmark using X-ray geometries and CCSD(T) energies. In order to obtain comparable results, the same functional was initially chosen for this study. This functional was found to give geometries in good agreement with those experimentally obtained for complexes Mo-1a (RMSD = 0.037 Å), Mo-1c (RMSD = 0.031 Å), and Mo-4 (RMSD = 0.030 Å) and therefore was selected for this study. The geometry optimization and energies of the possible spin states for these species were consistent with a doublet for Mo-1a, and a singlet ground state for Mo-1c and Mo-4, respectively.
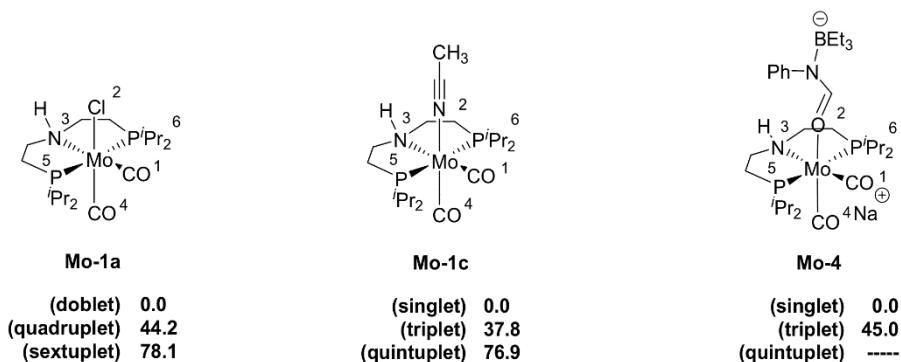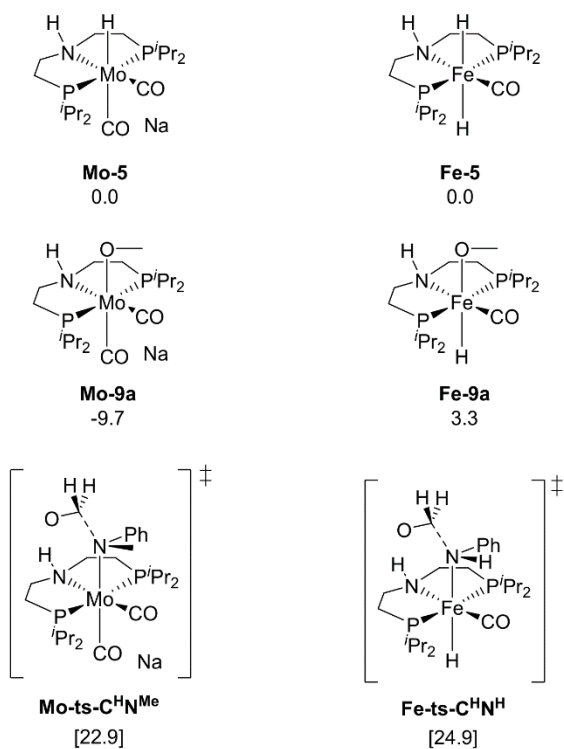
Figure S1. Mo-complexes used for the geometry benchmark using M06 with the labels used in Table S1, and the corresponding free energies for the first and second excited states. Mo-4 quintuplet did not converge.

Mo-1a

	Mo-CO[1]	Mo-Cl[2]	Mo-NH[3]	Mo-CO[4]	Mo-P[5]	Mo-P[6]	RMSD
Experimental	1.9536	2.5817	2.3029	1.9118	2.5002	2.4878	
M06							
(doublet)	1.9785	2.5814	2.3754	1.9549	2.5099	2.5099	0.0373
(quadruplet)	2.2574	2.6006	2.5649	1.9931	2.5313	2.5314	0.1687
(sextuplet)	2.2645	2.5904	2.5645	2.2881	2.6643	2.5793	0.2388

Mo-1c

	Mo-CO[1]	Mo-NCCH$_3$[2]	Mo-NH[3]	Mo-CO[4]	Mo-P[5]	Mo-P[6]	RMSD
Experimental	1.9203	2.2274	2.3227	1.9155	2.4389	2.4296	
M06							
(singlet)	1.9496	2.2247	2.3793	1.9490	2.4485	2.4485	0.0307
(triplet)	1.9775	2.2606	2.3677	1.9873	2.5054	2.5083	0.0608
(quintuplet)	2.3050	2.2898	3.2786	2.0528	2.6364	2.6682	0.4436

Mo-4

	Mo-CO[1]	Mo-OR[2]	Mo-NH[3]	Mo-CO[4]	Mo-P[5]	Mo-P[6]	RMSD
Experimental	1.8893	2.2391	2.3230	1.8893	2.4406	2.4421	
M06							
(singlet)	1.9116	2.2477	2.3694	1.8967	2.4777	2.4794	0.0304
(triplet)	2.0950	2.2919	2.4984	1.8675	2.5240	2.5271	0.1229

Table S1. Root mean square deviation of distances (in Å) of optimized geometries with respect experimental single crystal X-ray diffraction geometries, for Mo-1a, Mo-1c and Mo-4 molecules.

Comparison Iron system vs Molybdenum system.

In this work, a mechanism in which a methoxide intermediate is involved in the hemiaminal C-N bond cleavage (Mo-ts-12-13) has been proposed with Mo. This mechanism differs from the one previously proposed with Fe, in which the N of the hemiaminal is coordinated to Fe during the C-N bond cleavage (Fe-ts-$C^H N^H$). We have calculated ts-12-13 with Fe (see Figure S2) and has a higher energy than ts-$C^H N^H$, indicating that the methoxide mechanism is not preferred with Fe. The higher stability of the methoxide intermediate with Mo (Mo-9a) compared with (Fe-9a) may explain this difference in reactivity.
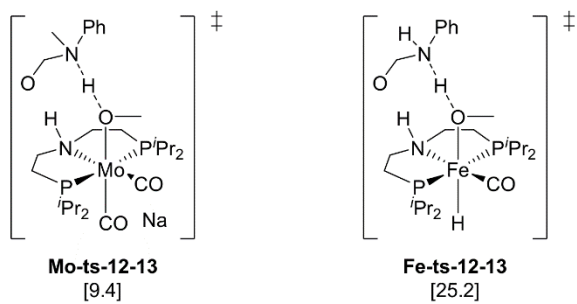

Mo-5
0.0

Fe-5
0.0

Mo-9a
-9.7

Fe-9a
3.3

Mo-ts-$C^H N^{Me}$
[22.9]

Fe-ts-$C^H N^H$
[24.9]

Mo-ts-12-13
[9.4]

Fe-ts-12-13
[25.2]

Figure S2. Computed free energies, in kcal mol^{-1}, for selected TSs and minima involved in the hemiaminal C-N bond cleavage step with Mo and Fe-systems.

Catalyst recovery mechanism.

The mechanism of catalyst recovery by addition of H_2 to the methoxide complex Mo-9a is shown in Fig. S3. In this pathway, methanol assists the activation of the Mo-H2 complex (Mo-14) by acting as a proton-shuttle. The global energy barrier for the catalyst recovery mechanism is 23.0 kcal mol^{-1}, which is similar to the global barrier for the hydride transfer with N-methylformanilide (5) (22.8 kcal mol^{-1}). This result suggests that both hydride transfer and catalyst recovery should be considered as rate limiting processes in the hydrogenation of amides catalyzed by Mo.
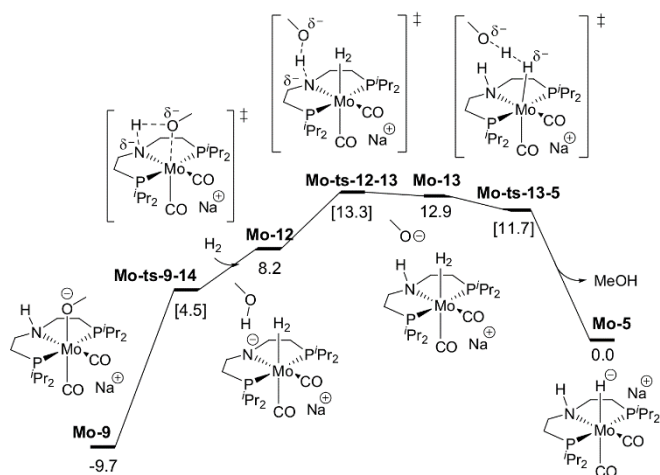

Figure. S3 Reaction pathway of the MeOH assisted hemiaminal proton transfer and posterior C-N bond cleavage. Gibbs energies in toluene (SMD) at 50 bar and 373 K are given in kcal mol^{-1}.

Hydrogenation of formaldehyde

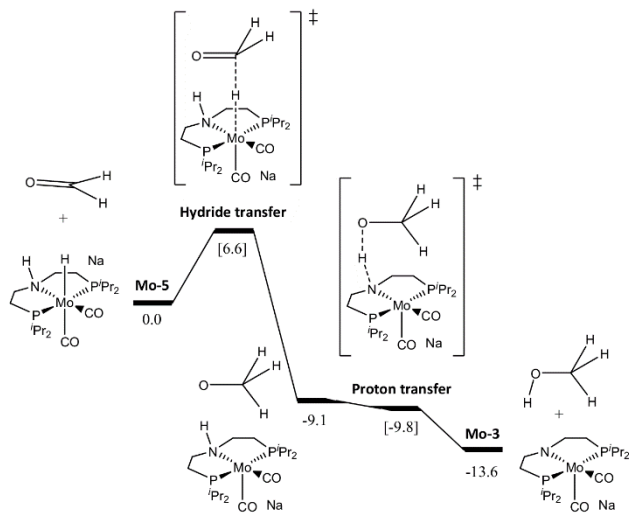The free energy profile for the formaldehyde reduction is represented in Figure S4.

Figure S4 Free energy profile in kcal mol^{-1} for the formaldehyde hydrogenation to methanol by Mo-5.

Mo-9a and Mo-ts-6-7 with Li$^+$, Na$^+$ and K$^+$

The energy barrier for the hydride transfer involves Mo-ts-6-7 and the methoxy intermediate Mo-9a, which is the ground state. The energy barriers computed for Na$^+$, K$^+$ and Li$^+$ is 22.9, 23.0, and 28.8 kcal/mol, respectively. Therefore, the difference in energy barrier for Li+ and K+ is 5.8 kcal/mol instead of 9 kcal/mol. In order to analyse these differences in energy barrier, the stability of Mo-9a and Mo-ts-6-7 with the different cations have been evaluated using isodesmic reactions (Figures S5). The energies of these reactions and the geometrical analysis of Mo-9a and Mo-ts-6-7 (Figures S6) suggest that the higher energy barrier for Li+ is due to a higher stabilization of the ground state (Mo-9a) with this cation, probably due to stronger electrostatic interaction of Li+ with the OMe group.
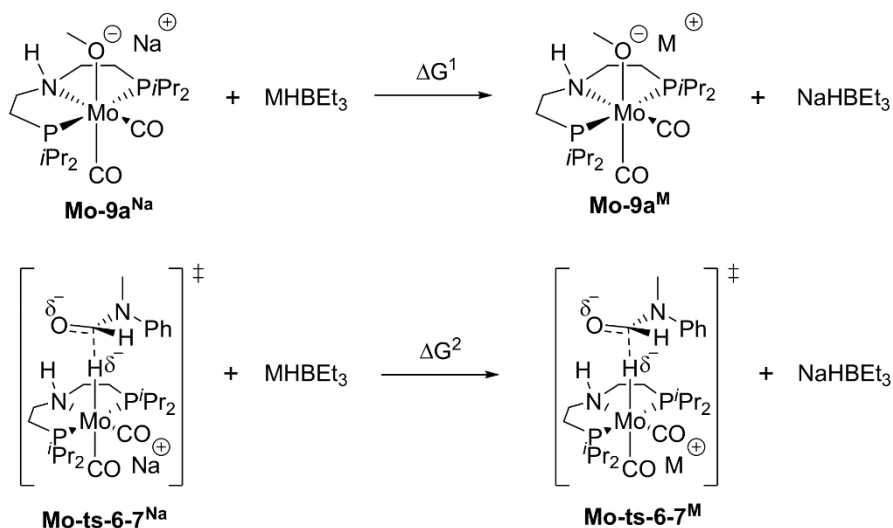
M	ΔG^1 (kcal mol^{-1})	ΔG^2 (kcal mol^{-1})
Li$^+$	- 4.6	1.4
K$^+$	- 0.9	-0.7

Figure S5. Free energies (kcal mol^{-1}) for the comparative isodesmic reaction between Li$^+$, Na$^+$ and K$^+$ in Mo-9a and Mo-ts-6-7

Mo-9a^{Li}   **Mo-9a^{Na}**   **Mo-9a^K**

Distances   O-Li 1.74 Å   O-Na 2.14 Å   O-K 2.48 Å
            O-Mo 2.36 Å   O-Mo 2.36 Å   O-Mo 2.35 Å

Mo-ts-6-7^{Li}   **Mo-ts-6-7^{Na}**   **Mo-ts-6-7^K**

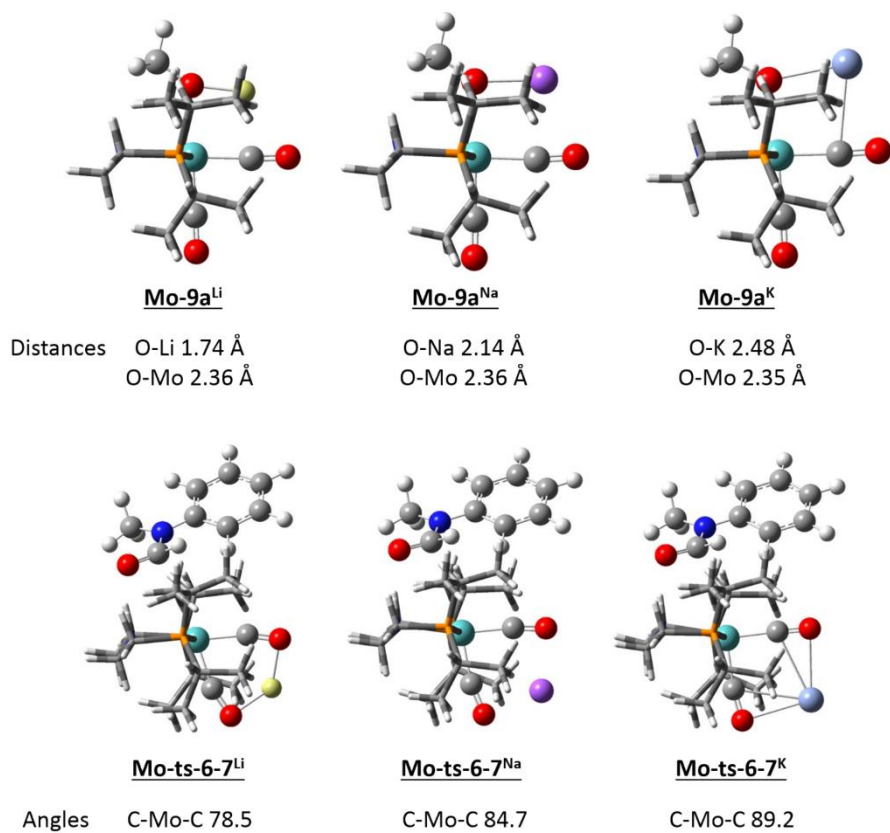Angles   C-Mo-C 78.5   C-Mo-C 84.7   C-Mo-C 89.2

Figure S6. Optimized geometries for Mo-9a and Mo-ts-6-7 with selected distances and angles in Å. PNP ligand depicted in tubes/wireframes for visual clarity. Mo (turquoise), C (grey), O (red), N (blue), H (white), P (orange), Li (Litium), Na (purple), K (lavender).

Microkinetic model

Microkinetic models were constructed with the COPASI software (version 4.22).[7] The initial concentrations used in the simulations were those reported in the experiments (0.25 M of N-methylformanilide, 0.207 M of hydrogen and 0, 0.125 and 0.5 M of ethanol). The concentration of hydrogen was kept constant, in line with the effectively constant pressure of hydrogen used in the reactor (50 atm). H_2 concentration was approximated using the molar fraction of H_2 in a saturated solution of H_2 in toluene at 50 atm and 100 ºC assuming incompresibility of THF and that $[H_2] \ll [toluene]$.[8] As in the experiments, simulations were carried out for a total time of 24 hours at T = 373 K. The models were based on deterministic time course simulations with the LSODA algorithm.[9]

Two microkinetic models were constructed: 1) assuming a barrierless catalyst activation; 2) including a catalyst activation process with an energy barrier estimated to fit the experimental conversions. We have not studied computationally the catalyst activation process due to the complexity and little experimental information obtained for this reaction.

1) *N-methylformanilide with EtOH poisoning assuming barrierless catalyst activation.*

The N-methylformanilide conversion *vs* time traces using Mo-5 as catalyst were obtained by running a microkinetic model described below. A concentration of 12.5 mM of Mo-5 was used. The elementary steps of the mechanism underlying the microkinetic model are given in Figure S7 and Figure S8, together with the $\Delta G^{\ddagger}$ values derived from the DFT calculations in Table S2.

2) *N-methylformanilide with EtOH poisoning assuming a catalyst activation.*

The N-methylformanilide conversion *vs* time traces using Mo-1a as catalyst were obtained by running a microkinetic model described below. A concentration of 12.5 mM of Mo-1a and 12.5 mM of NaHBEt$_3$ were used. The elementary steps of the mechanism underlying the microkinetic model are given in Figure S7 and Figure S8, together with the $\Delta G^{\ddagger}$ values

derived from the DFT calculations in Table S2. Mo-ts-6-7, was optimized to 25.1 kcal mol^{-1} to fit experimental conversions.
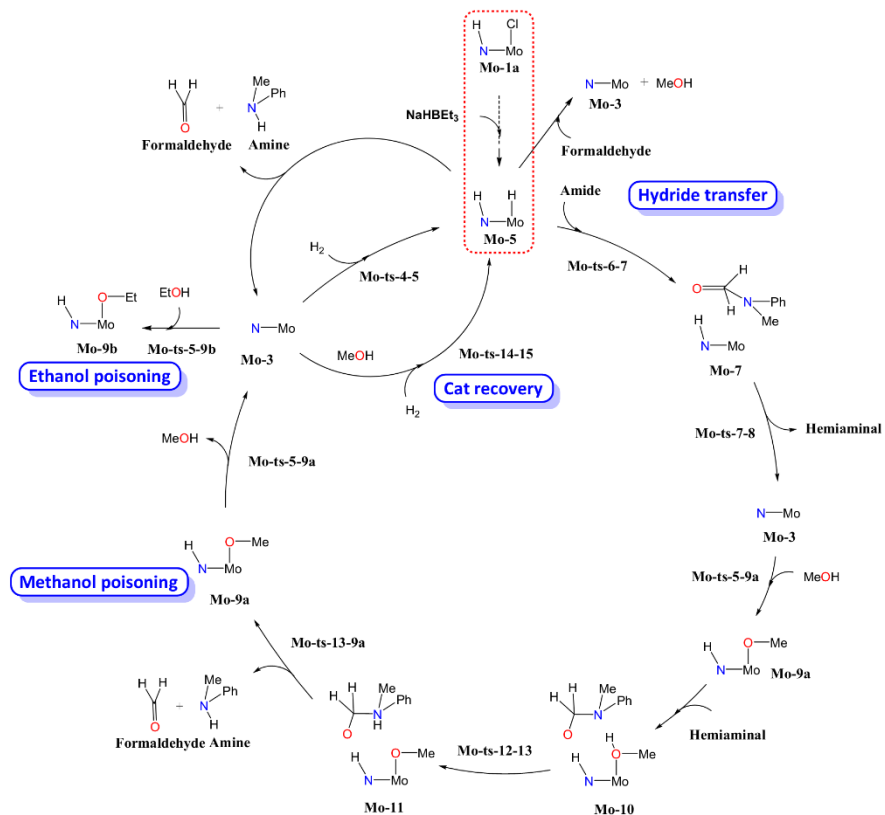

Figure S7. Reactions included in the microkinetic model of N-methylformanilide deaminative hydrogenation. In red dotted square, catalyst activation reaction.
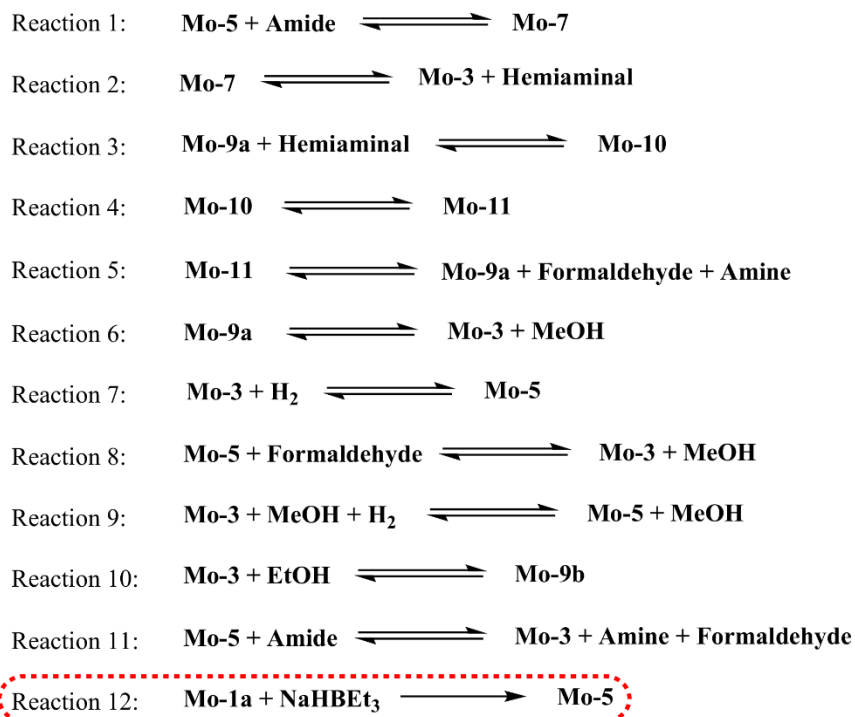
Reaction 1:	**Mo-5 + Amide**	⇌	**Mo-7**
Reaction 2:	**Mo-7**	⇌	**Mo-3 + Hemiaminal**
Reaction 3:	**Mo-9a + Hemiaminal**	⇌	**Mo-10**
Reaction 4:	**Mo-10**	⇌	**Mo-11**
Reaction 5:	**Mo-11**	⇌	**Mo-9a + Formaldehyde + Amine**
Reaction 6:	**Mo-9a**	⇌	**Mo-3 + MeOH**
Reaction 7:	**Mo-3 + H$_2$**	⇌	**Mo-5**
Reaction 8:	**Mo-5 + Formaldehyde**	⇌	**Mo-3 + MeOH**
Reaction 9:	**Mo-3 + MeOH + H$_2$**	⇌	**Mo-5 + MeOH**
Reaction 10:	**Mo-3 + EtOH**	⇌	**Mo-9b**
Reaction 11:	**Mo-5 + Amide**	⇌	**Mo-3 + Amine + Formaldehyde**
Reaction 12:	**Mo-1a + NaHBEt$_3$**	→	**Mo-5**

Figure S8 Reactions used in the microkinetic simulations. In red dotted square, reaction included in the model to estimate the catalyst activation.

	ΔG‡ Forward (kcal mol^{-1})	ΔG‡ Backwards (kcal mol^{-1})
Reaction 1	13.1	6.5
Reaction 2	3.1	0.4
Reaction 3	7.4	0.1[a]
Reaction 4	5.9	0.2[b]
Reaction 5	0.2[b]	13.9
Reaction 6	14.2[c]	2.8
Reaction 7	18.6	20.3
Reaction 8	6.6	20.2
Reaction 9	11.6	13.3
Reaction 10	5.0[c]	18.3
Reaction 11	22.9	14.4

Table S2. Reactions and corresponding Gibbs energies (kcal mol^{-1}) used in the microkinetic model of the deaminative hydrogenation of DMF. In red, reaction included to fit the experimental conversions. [a] TS raised to 5.2 to get positive energies. [b] TSs raised to 11 kcal mol^{-1} to get positive energies. [c] Estimated low energy barrier.

Evaluation of the position of the Na cation

The cation location was determined by computing the energy of selected species (Mo-3, Mo-4, Mo-5, and Mo-9a) with the cation in different positions (interacting with two CO ligands, P_{2CO}; or interacting with CO and a lone pair, $P_{CO/LP}$; see scheme S9). The location yielding the lowest energy was the one used in the energy profiles, and is the one represented in the Schemes of the manuscript. In most cases, small energy differences (<2 kcal/mol) are obtained when comparing P_{2CO} and $P_{CO/LP}$ structures.
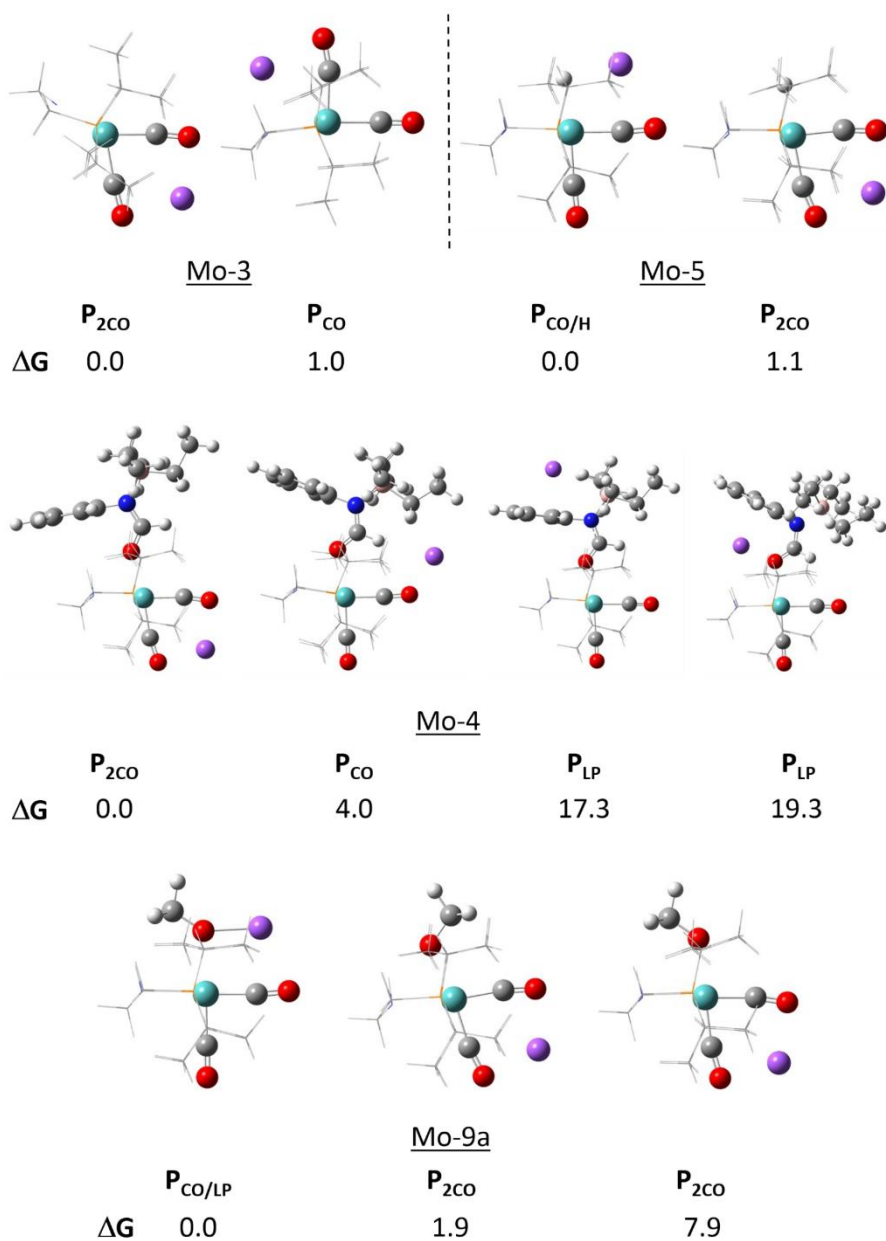
Figure S9. Evaluation of multiple Na⁺ positions and their relative free energies (kcal mol⁻¹). PNP ligand depicted in a wireframe representation for more clarity. Legend: Mo (turquoise), C (grey), O (red), N (blue), H (white), Na (purple), P (orange)

[1]T. Leischner, A. Spannenberg. K. Junge, M. Beller, *Organometallics*, 2018, 37, 4332-4335.

[2]J. Chen, W. Long, S. Fang, Y. Yang, X. Wan, *Chem. Commun.*, 2017, 53, 13256-13259.

[3]R. Bisht, M. E. Hoque, B. Chattopadhyay, *Angew. Chem. Int. Ed.*, 2018, 57, 15726-15766.

[4]P. V. Ilyin, A. S. Pankova, M. A. Kuznetzov, *Synthesis*, 2012, 44, 1353-1358.

[5]H. Taneda, K. Inamoto, Y. Kondo, *Chem. Commun.*, 2014, 50, 6523-6525.

[6]L. Artús Suàrez, Z. Culakova, D. Balcells, W. H. Bernskoetter, O. Eisenstein, K. I. Goldberg, N. Hazari, M. Tilset, A. Nova, *ACS Catal*, 2018, 8, 8751-8762.

[7]S. Hoops, S. Sahle, R. Gauges, C. Lee, J. Pahle, N. Simus, M. Singhal, L. Xu, M. Pedro, U. Kummer, *Bioinformatics,* 2006, 22, 3067-3074.

[8]E. Brunner, *J. Chem. Eng. Data.* 1985, 30, 269-273.

[9]L. Petzold, *SIAM. J. Sci. and Stat. Comput.* 1983, 4, 136-148.

[10]M. J. Frisch, G. W. Trucks, H. B. Schlegel, G. E. Scuseria, M. A. Robb, J. R. Cheeseman, G. Scalmani, V. Barone, B. Mennucci, G. A. Petersson, H. Nakatsuji, M. Caricato, X. Li, H. P. Hratchian, A. F. Izmavlov, J. Blonio, G. Zheng, J. L. Sonnenberg, M. Hada, M. Ehara, K. Toyota, R. Fukuda, J. Hasegawa, M. Ishida, T. Nakajima, Y. Honda, O. Kitao, H. Nakai, T. Verve, J. A. Montgomery, J. E. Peralta, F. Ogliare, M. Bearpark, J. J. Heyd, E. Brothers, K. N. Kudin, V. N. Staroverov, T. Keith, R. Kobayashi, J. Normand, K. Raghvachari, A. Rendell, J. C. Burant, S. S. Ivengar, J. Tomasi, M. Cossi, N. Rega, J. M. Millam, M. Klene, J. E. Knox, J. B. Cross, V. Bakken, C. Adamo, J. Jaramillo, R. Gomperts, R. E. Stratmann, O. Yazyev, A. J. Austin, R. Cammi, C. Pomelli, J. W. Ochterski, R. L. Martin, K. Morokuma, V. G. Zakrezweski, G. A. Voth, P. Salvador, J. J. Dannenberg, S. Dapprich, A. D. Daniels, O. Fakas, J. B. Foresman, J. V. Ortiz, J. Cioslowski, G. A. Voth, *Gaussian 09*, Revision D.01; Gaussian, Inc.: Wallingford CT, 2013.

[11]Y. Zhao, D. Truhlar, Theor. *Chem. Acc.*, 2008, 120, 215-241.

[12](a) P. Hay, W. Wadt, *J. Chem. Phys.,* 1985, 82, 270-283 (b) W. Wadt, P. Hay, *J. Chem. Phys.*, 1985, 82, 284-298.

[13](a) W. J. Hehre, R. Ditchfield, J. A. Pople, *J. Chem. Phys.*, 1972, 56, 2257-2261 (b) W. Kohn, A. D. Becke, R. G. Parr, *J. Phys. Chem.*, 1996, 1, 12974-12980.

[14]A. McLean, G. Chandler, *J. Chem. Phys.*, 1980, 72, 5639-5648.

[15]A. Marenich, C. Cramer, D. Truhlar, *J. Phys. Chem. B.*, 2009, 113, 6378-6396.

[16]M. Álvarez-Moreno, C. De Graaf, N. López, F. Maseras, J. M. Poblet, C. Bo, *J. Chem. Inf. Model.*, 2015, 55, 95-103.

[17]S. Hoops, R. Gauges, C. Lee, J. Pahle, N, Simus, M. Singhal, L. Xu, P. Mendes, U. Kummez, *Bioinformatics*, 2006, 22, 3067-3074.